Measurements of the Magnetic Form Factor of the Proton for Large Timelike Momentum Transfers

Doctoral Dissertation

Giulio Stancari

Advisor: Professor Roberto Calabrese

1998

Department of Physics

University of Ferrara

Italy

This doctoral dissertation was written in American English, according to the *Decreto del Presidente della Repubblica n. 387 del 3 ottobre 1997, Art. 3*, after obtaining the favorable opinion of the *Collegio dei Docenti* of the Department of Physics.

Author's address:
Dipartimento di Fisica dell'Università
Via Paradiso, 12
44100 Ferrara (FE) — Italy
Phone: +39-(0532)-781849
Fax: +39-(0532)-762057
E-mail: `stancari@fe.infn.it`

Typeset using TEX by Donald Knuth, the LATEX macros by Leslie Lamport and the `thesis` document class by Wenzel Matiaske.

to my parents,

Antonio and Isa

ACKNOWLEDGEMENTS[a]

I would like to thank my advisor, Prof. Roberto Calabrese, for his counsel and for giving me the opportunity to work on this interesting project. As an undergraduate student, I admired his talent as a teacher, especially his way of getting to the core of the problems being discussed. By working with him for a few years now, I have also been able to appreciate his experimental ability and his physical insight.

Prof. Diego Bettoni took an active interest in my analysis work. It has been a great pleasure to work with him and to share ideas and questions. I am among the many people who envy his culture, sagacity and sense of humor.

The results would not have been obtained without the hard work of the E-835 collaborators and of the Fermilab staff, whom I wish to thank also for their advice, teachings and encouragement in the persons of Prof. Rosanna Cester and Dr. Stephen Pordes. I would like to express my gratitude to the whole Fermilab community as well, for providing an excellent work environment, which I appreciated during my stays at the lab.

The following people have provided me with lots of useful information, especially data, papers, figures or, simply, good explanations: Stefano Bagnasco (forward calorimeter), Wander Baldini (charged trigger),

---

[a] This research was funded by the Istituto Nazionale di Fisica Nucleare, the U.S. Department of Energy and the U.S. National Science Foundation.

Prof. Giovanni Borreani (Čerenkov counter), Xiaoling Fan (nice picture of the E-835 detector), Gabriele Garzoglio (jet target, beam energy measurement), Dr. Keith Gollwitzer (central calorimeter, E-760 apparatus), Sheng Jin (neutral trigger), Jason Kasper (neutral trigger description and neutral data summary tapes), Prof. Mark Mandelkern (helicity formalism), Dr. Flavio Marchetto (Čerenkov counter), Jim Morgan (layout of the Antiproton Source), Dr. Roberto Mussa (scintillating fiber tracker), Dr. Nadia Pastrone (straw chambers), Dr. Claudia Patrignani (Electron-Weight algorithm and efficiencies), Todd Pedlar (luminosity monitor), Paolo Rumerio (straw chambers) and Michelle Stancari (central calorimeter readout, $\pi^0\pi^0$ event selection). In particular, I greatly benefited from discussions with Dr. Eleonora Luppi. Besides her experience of form factor physics, she is also an extraordinarily generous person. I apologize to all persons I have involuntarily left out of this list.

My Italian family, and my brother Giorgio in particular, deserve a warm "thank you" for being so supportive and for bearing with my frequent travels. Not to mention all my friends...

In these acknowledgements, I would like to reserve a special place for my wife Michelle, who shared with me hard times and laughs, frustrations and joys, country music and jazz, Pepto-Bismol[b] and ice-cream. If you think that this dissertation is lacking some information, or that some parts could be further refined, remember what she always says: "In each tube, there is an infinite amount of toothpaste; it just gets infinitely hard to squeeze it out!".

[b] Disgusting pink fluid, supposed to help you digest.

CONTENTS

INTRODUCTION

The understanding of the structure of the proton is an interesting and challenging research field in Particle Physics.

Within the framework of Quantum Electrodynamics, the proton's electromagnetic properties are characterized by two parameters, the electric and magnetic form factors $G_E(q^2)$ and $G_M(q^2)$, which are functions of the squared four-momentum q^2 transferred by the photon to the proton itself. In principle, Quantum Chromodynamics could describe the structure of the proton, including its electromagnetic form factors, but technical difficulties have made it impossible so far to deduce quantitative predictions, except for cases where approximations are valid or models are applicable.

In the spacelike region ($q^2 < 0$), the electric and magnetic form factors have been measured with high accuracy in elastic electron-proton scattering up to $\left|q^2\right|$ = 10 (GeV/c)^2 and $\left|q^2\right|$ = 31 (GeV/c)^2, respectively. Measurements for timelike momentum transfers ($q^2 = s > 0$) come from the reactions $e^+e^- \rightarrow p\bar{p}$ and $\bar{p}p \rightarrow e^+e^-$; these data have added precious information to the knowledge of form factors, but they are mainly concentrated in a small interval near threshold, at $4m_p^2 \leq s \leq 7$ GeV^2. The main reason is that G_E and G_M turn out to be rapidly decreasing functions of q^2, which makes cross sections quickly inaccessible.

The first attempts to make measurements at larger momentum transfers were made by the CERN experiment R-704; only upper limits were established, at $s = 8.9$ GeV^2 and $s = 12.5$ GeV^2. The first non-zero results came from Fermilab experiment E-760, which measured $|G_M|$ in $\bar{p}p$ annihilations at $s = 8.9$ GeV^2,$s = 12.4$ GeV^2 and $s = 13.0$ GeV^2. The breakthrough was brought about by the concurrence of the goals of form factor and charmonium physics. High-quality antiproton beams, a hydrogen gas jet target and a powerful electron/positron tagging system were the key elements which allowed to reach high luminosities; at the same time, the background arising from the large $\bar{p}p$ total cross section could be suppressed.

In this dissertation, I present new improved measurements of the magnetic form factor of the proton for timelike momentum transfers up to $s = 14.4$ GeV^2. They come from the analysis of the data taken by Fermilab experiment E-835, which is an upgrade of E-760. These results are the highest-energy, most-precise ones existing to date.

In Chapter 1, I discuss the physics of form factors, including the basic theoretical framework and the most relevant experimental facts observed for spacelike momentum transfers. The chapter also includes a complete review of the measurements performed so far in the timelike region. Chapter 2 is a description of the experimental technique employed by E-835, with emphasis on the physical motivations and on the aspects of the apparatus relevant to the form factors. In this chapter, I dedicated some extra space to the scintillating fiber tracker, since its assembly and performance analysis represented my primary occupation during the first two years of graduate school. The results I obtained are presented in detail in Chapter 3. Even though the detector characteristics makes the event selection relatively straightforward, the estimate of the efficiencies and of the background required careful studies. Some conclusions are drawn in Chapter 4.

Note on the conventions used. The real metric $g_{00} = -g_{kk} = 1$ ($k = 1, 2, 3$) is employed; ie the contraction $x^\mu x_\mu$ of a timelike four-vector x is positive. I tried to use natural units ($c = \hbar = 1$) consistently throughout the dissertation. The right-handed coordinate system usually referred to for the description of detectors and events (laboratory frame) has its origin at the interaction vertex; the z axis is in the direction of the particle beam, whereas the y axis is vertical and points upwards.

Giulio Stancari

Ferrara, Italy

December 1998

1. THE PHYSICS OF FORM FACTORS. THEORETICAL FRAMEWORK AND EXPERIMENTAL PROGRAMS IN A HISTORICAL PERSPECTIVE

Elastic electromagnetic processes represent an important source of information about the structure of hadrons. Their study began over forty years ago and led to a better understanding of the electrodynamics of composite particles. Deep inelastic scattering constitutes one of the experimental foundations of Quantum Chromodynamics, and, for some years, it has overshadowed the importance of form factors because of its slower decreasing cross sections. Quantum Chromodynamics is now universally believed to be the theory of strong interactions. Still, some of the most fundamental phenomena, like the binding of quarks and gluons inside hadrons or the electromagnetic properties of the proton, are not fully understood. Where the experimental feasibility has allowed to collect a large amount of data, the theory encounters technical difficulties that have been so far insurmountable. On the other hand, data is scarce (if not inexistent) where the theory is calculable. The experimental work presented in this dissertation adds a contribution to the understanding of the proton structure at the frontier of the region explored so far.

In this chapter, the physical meaning of form factors is discussed from several points of view. The peculiarities of some experimental techniques are also presented.

1.1 Introductory Remarks

Form factors are introduced to describe the structure of a composite system. They quantify the deviations from the behavior of a pointlike object, which is assumed to be known.

For example, in non-relativistic Quantum Mechanics one can study the scattering of a charged particle in the field of a static point charge. The first-order perturbative result is equal to the Rutherford cross section and depends on the kinetic energy E of the incident particle and on the scattering angle θ:

$$\left(\frac{d\sigma}{d\Omega}\right)_{\text{point}} = \frac{\alpha^2}{4E^2 \sin^4(\theta/2)}, \tag{1.1}$$

where α is the fine structure constant. If the pointlike charge is replaced by an extended charge distribution $\rho(\mathbf{r})$, the cross section acquires a dependence on the momentum transfer $\mathbf{q} \equiv \mathbf{k} - \mathbf{k}'$, where $\mathbf{k}$ and $\mathbf{k}'$ are the momenta of the particle before and after scattering, respectively:

$$\left(\frac{d\sigma}{d\Omega}\right)_{\text{extended}} = |F(\mathbf{q})|^2 \cdot \left(\frac{d\sigma}{d\Omega}\right)_{\text{point}}. \tag{1.2}$$

In this case, the form factor $F(\mathbf{q})$ is the Fourier transform of the charge distribution:

$$F(\mathbf{q}) = \int e^{i\mathbf{q}\cdot\mathbf{r}} \rho(\mathbf{r})\, d^3\mathbf{r}. \tag{1.3}$$

The form factor of the charge distribution being sampled can be measured by comparing the observed cross section with the calculated point cross section. In principle, one needs to measure the form factor for each value of

$\mathbf{q}$ in order to extract the charge distribution. Nevertheless, if ρ is spherically symmetric and the behavior of F is known for small $\mathbf{q}$, the mean square radius can be obtained from Equation 1.3:

$$\langle r^2 \rangle = -6 \left(\frac{dF}{d\,|\mathbf{q}|^2} \right)_{|\mathbf{q}|=0} . \tag{1.4}$$

In other words, a large wavelength probe cannot resolve the detailed structure of the charge cloud, but it is sensitive to its size.

In general, the form factors are quantities used to parameterize the structure of an extended object and to interpret the experimental results. A theory that aims at explaining the structure of a composite system should in principle be able to predict its form factors. The following discussions will be focused on the electromagnetic form factors of the proton, which are the object of this dissertation.

1.2 Parameterization of the Proton Structure. Form Factors in Quantum Electrodynamics

In 1950, Rosenbluth calculated the differential cross section of elastic electron-proton scattering in the framework of recently developed QED (Rosenbluth 1950). The corresponding Feynman diagram is shown in Figure 1.1.

The incoming electron has four-momentum $k \equiv (E, \mathbf{k})$, whereas k' is its four-momentum after interacting with the proton and being deflected by an angle θ. The momentum transferred by the electron to the proton is $q \equiv k - k'$ and it is spacelike: $q^2 = -2m_p T < 0$, where T is the kinetic energy of the recoiling proton in the frame where it is initially at rest. It is often convenient to define $Q^2 \equiv -q^2$, which is positive in the spacelike region.

From now on, we will assume that the electron rest energy m_e is negligible with respect to its total energy. The momentum transfer becomes:

$$
\begin{aligned}
Q^2 &= 2EE' \cdot \left[1 - \cos\theta - \frac{m_e^2}{EE'}\right] && (1.5)\\
&\simeq 4EE' \sin^2(\theta/2) && (1.6)\\
&= \frac{4E^2 \sin^2(\theta/2)}{1 + 2(E/m_p)\sin^2(\theta/2)} && (1.7)
\end{aligned}
$$

For a given energy of the impinging electron, the maximum momentum transfer is achieved when the electron is back-scattered, but it is the energy E that sets its order of magnitude.

One of the main points in Rosenbluth's paper was to quantify the deviations from the behavior of a pointlike Dirac particle. These were taken into account by allowing the proton's charge and anomalous magnetic moment to vary as a function of the invariant momentum transfer, which is chosen as the independent kinematic quantity of the process. This is done[a] by writ-

[a] A standardized notation is used in place of the parameterization found in the original papers.

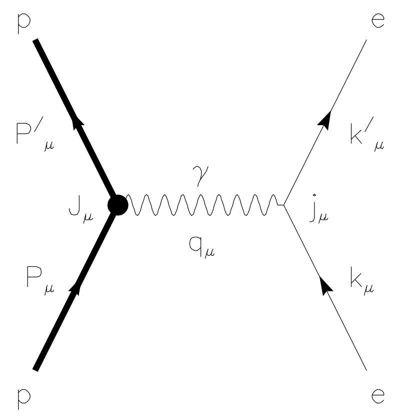

Fig. 1.1: Lowest-order Feynman diagram for elastic electron-proton scattering.

ing the current operator J_μ in terms of the static charge e and anomalous magnetic moment κ multiplied by two functions $F_1(q^2)$ and $F_2(q^2)$:

$$J_\mu = e\left[\gamma_\mu F_1 + \frac{\kappa}{2m_p}\sigma_{\mu\nu}q^\nu F_2\right]. \tag{1.8}$$

This form is to be compared with the pointlike lepton current $j_\mu = e\gamma_\mu$. If we use the abbreviation $\tau \equiv Q^2/4m_p^2$, the resulting first-order differential cross section in the laboratory frame is known as Rosenbluth's formula:

$$\left(\frac{d\sigma}{d\Omega}\right)_R = \left(\frac{d\sigma}{d\Omega}\right)_{NS} \cdot \left[\frac{G_E^2 + \tau G_M^2}{1+\tau} + 2\tau G_M^2 \tan^2(\theta/2)\right]. \tag{1.9}$$

The subscript NS indicates the scattering of the electron off a no-structure spinless object. The corresponding cross section is the Mott cross section multiplied by a factor that takes the recoil of the proton into account:

$$\left(\frac{d\sigma}{d\Omega}\right)_{NS} = \frac{E'}{E} \cdot \left(\frac{d\sigma}{d\Omega}\right)_{Mott} = \frac{E'}{E} \cdot \frac{\alpha^2 \cos^2(\theta/2)}{4E^2 \sin^4(\theta/2)}. \tag{1.10}$$

In the Mott cross section, the factor $\cos^2(\theta/2)$ comes from the spin of the electron, while the rest is the familiar Rutherford expression for the scattering of a spinless particle off an electrostatic potential.

The 'electric' and 'magnetic' form factors G_E and G_M, also known as Sachs form factors, are introduced as follows:

$$\begin{aligned} G_E &\equiv F_1 + \kappa\frac{q^2}{4m_p^2}F_2 \\ G_M &\equiv F_1 + \kappa F_2. \end{aligned} \tag{1.11}$$

The physical meaning of this parameterization, already hinted at by Yennie et al. (1957), was fully investigated by Ernst, Sachs, and Wali (1960). These form factors are used because they are strictly related to the charge and magnetic moment distributions inside the nucleon. In particular, their values at $q^2 = 0$ are the static electric charge and magnetic moment of the proton:

$$\begin{aligned} e &= eG_E(0) \\ \mu &= \frac{e}{2m_p} G_M(0)\boldsymbol{\sigma}; \end{aligned} \tag{1.12}$$

whereas their slope at the origin is proportional to the second moments of the charge and magnetic moment distributions:

$$\begin{aligned} \langle r^2_{ch} \rangle &= 6 \left. \frac{dG_E}{dq^2} \right|_{q^2=0} \\ \langle r^2_{mag} \rangle &= \frac{6}{\mu_p} \left. \frac{dG_M}{dq^2} \right|_{q^2=0} \end{aligned} \tag{1.13}$$

The expression of the current operator used by Rosenbluth (Equation 1.8) is the most general, as shown by Foldy (1952) and, under fewer restrictions, by Salzman (1955) and Yennie et al. (1957). In other words, two independent functions of q^2 are necessary and sufficient to characterize the electromagnetic properties of any spin 1/2 particle, under the assumptions of relativistic covariance and current conservation. With time-reversal arguments, one can show that these functions can be chosen to be real for every $q^2 \leq 0$.

1.3 First Experimental Information on the Proton Structure. The Spacelike Region

Rosenbluth's work was motivated by the fact that intense electron beams were becoming available at the new Stanford linac. A wide energy range, from 6 to 1000 MeV, was accessible. The scattering from a hydrogen target could represent a test for QED and, also, a way of studying the proton structure. A systematic experimental program followed, allowing to collect a large body of data in the spacelike region (Hofstadter 1963).

McAllister and Hofstadter (1956) were the first to measure the size of the proton. The electron beam accelerated by the Stanford linac was directed towards a high-pressure hydrogen chamber, which was placed inside an evacuated vessel. The scattered electrons, after being collimated by a set of slits, entered a magnetic spectrometer, which could be moved around the target. Interpreting the number of observed counts as a function of the scattering angle according to Rosenbluth's formalism, a value of $\sqrt{\langle r^2 \rangle} = 0.74 \pm 0.24$ fm was deduced. This result relies on the assumption that the charge and magnetic moment distributions are similar.

The form factors can be separated by measuring the reduced Rosenbluth cross section, which can be defined from Equation 1.9:

$$\sigma_{\mathrm{red}} \equiv \left[\left(\frac{d\sigma}{d\Omega} \right)_R \Big/ \left(\frac{d\sigma}{d\Omega} \right)_{NS} \right] \frac{(1+\tau)\epsilon}{\tau} = \frac{\epsilon}{\tau} G_E^2 + G_M^2 \tag{1.14}$$

The quantity ϵ is a function of Q^2 and of the scattering angle and is bounded:

$$\epsilon = \left[1 + 2(1+\tau) \tan^2 (\theta/2) \right]^{-1}; \quad 0 \le \epsilon \le 1. \tag{1.15}$$

For fixed Q^2, the reduced cross section is linear in ϵ. From a fit to the data one can extract the slope G_E^2/τ and the intercept G_M^2. This procedure is known as Rosenbluth separation, and allows to measure both form factors if the momentum transfer is not too large.

The behavior of G_E and G_M has been investigated over a wide range of Q^2. Walker et al. (1994) and Andivahis et al. (1994) report recent measurements of both the electric and magnetic form factor at $Q^2 < 10\ (\mathrm{GeV}/c)^2$ obtained at SLAC. Walker et al. (1994) have also performed a global fit to all existing data. As can be seen from Figure 1.2, the form factors can be well represented by the following empirical functional form, known as the

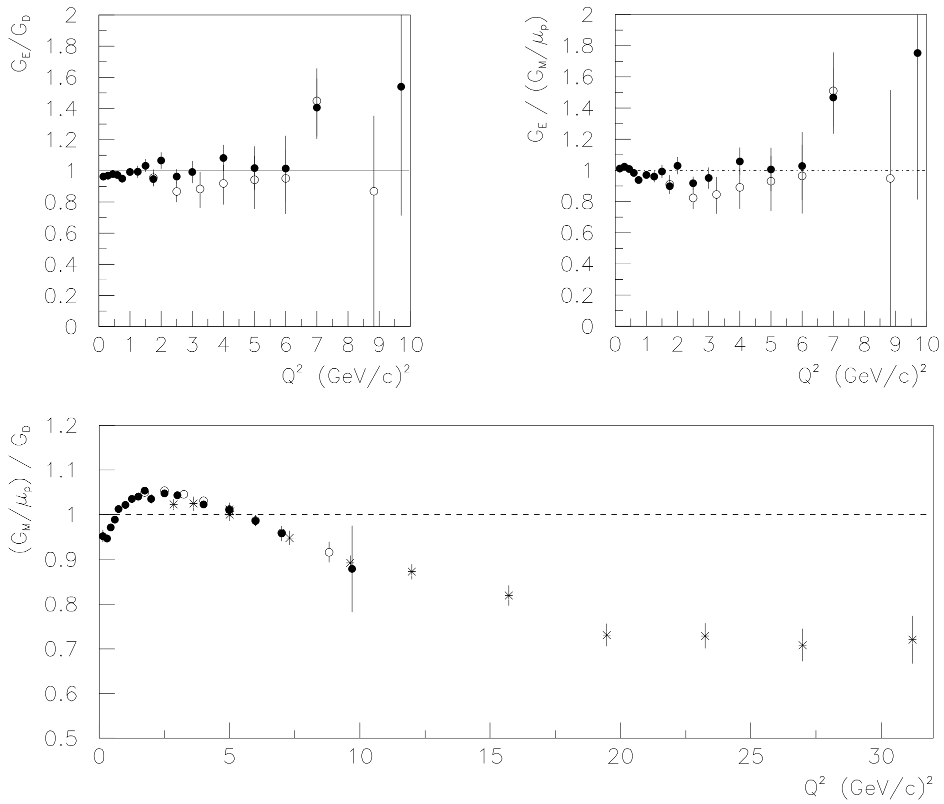

Fig. 1.2: Form factors obtained in electron-proton elastic scattering. The data at low Q^2 are from a fit to all existing measurements performed by Walker et al. (1994) (•). The mid- and high-Q^2 regions have been explored by Andivahis et al. (1994) (∘) and Sill et al. (1993) (∗), respectively.

dipole formula:

$$G_D = \left(1 + \frac{Q^2}{\Lambda}\right)^{-2} \quad \Lambda = 0.71\,\mathrm{GeV}^2. \tag{1.16}$$

The electric and magnetic form factors are also found to scale approximately in the same way: $G_E(q^2) = G_M(q^2)/\mu_p = G_D$. Deviations from the dipole behavior and from scaling are within approximately 10% for Q^2 smaller than 10 (GeV/c)^2.

These facts confirmed that the electric and magnetic moment distributions are very similar. The proton root-mean-square radius (from Equation 1.13) comes out to be $\sqrt{\langle r^2 \rangle} \simeq 0.8$ fm.

At low momentum transfer, i. e. when $Q^2 \ll m_p^2$, the recoil of the proton is negligible and $E'/E \simeq 1$. In this regime, $G_E(q^2)$ can be interpreted as the Fourier transform of a charge density $\rho(\mathbf{r})$. Transforming the dipole function G_D, one gets a charge density proportional to e^{-r}.

Because of the kinematic factors in Equations 1.9 and 1.14, at high momentum transfers Rosenbluth separation cannot be performed, and only the magnetic form factor can be precisely measured. Recent data (Sill et al. 1993) taken at SLAC in this regime up to $Q^2 = 31$ (GeV/c)^2 indicate significant deviations from the dipole behavior, as shown in Figure 1.2.

1.4 Form Factors in the Timelike Region

At the beginning of the 1960s, the feasibility of electron-positron colliders was proven at Stanford and Frascati, opening a wide spectrum of physical investigations. A discussion of the possible experiments and of some theoretical predictions from those years, including the form factors of barions, can be found in the paper by Cabibbo and Gatto (1961).

In the same years, soon after their discovery in 1955, antiprotons became available in relatively intense beams ($\approx 10^4$ particles per pulse). A proposal was made by Zichichi et al. (1962) to study lepton-antilepton final states in antiproton-proton annihilations at CERN.

In the process

$$\bar{p}p \to e^+e^-, \tag{1.17}$$

the momentum transfer $q \equiv -(k + k')$ is directly related to the center-of-momentum (CM) energy and it is timelike: $q^2 = s > 0$. Obviously, the reaction can only take place above a certain threshold, which corresponds to $s = 4m_p^2$. By definition (Equation 1.11), at threshold G_E equals G_M.

The angular distribution of process 1.17 can be predicted using helicity arguments, introduced in an elegant article by Jacob and Wick (1959). One of their main results is an expression for the scattering amplitude $f(\theta, \phi)$ for the process $a + b \to c + d$. In general, the angular dependence can be factorized in terms of exponentials and rotation matrices $d^j(\theta)$. Each term is weighed by amplitudes expressing the dynamics of the process, which, in general, depend upon the CM energy $\sqrt{s}$, the total angular momentum J and the spin of the particles (through their helicities λ_a, λ_b, λ_c and λ_d). In symbols:

$$\begin{aligned} d\sigma &= |f(\theta, \phi)|^2 \, d\Omega & (1.18) \\ f(\theta, \phi) &= \frac{1}{p} \sum_J (J + 1/2) \, \langle \lambda_c \lambda_d \left| T^J(s) \right| \lambda_a \lambda_b \rangle \, e^{i(\lambda-\mu)\phi} \, d^J_{\lambda\mu}(\theta) & (1.19) \\ & (\lambda = \lambda_a - \lambda_b; \;\; \mu = \lambda_c - \lambda_d), & (1.20) \end{aligned}$$

where p is the relative momentum of the two particles in the initial state and T is related to the S-matrix by $S - 1 = iT$. The sum over J reflects the fact that a two-particle state $|p;\, \theta\phi;\, \lambda_1\lambda_2\rangle$ emerging at a definite angle in the CM frame can be expressed as a superposition of states $|p;\, JM;\, \lambda_1\lambda_2\rangle$

with definite total angular momentum (and vice versa).

In the process 1.17, since the electron rest energy m_e is negligible, the final state total helicity $\mu \equiv \lambda_{e^+} - \lambda_{e^-}$ can only be $\mu = \pm 1$. This is equivalent to saying that, at high energy, helicity is conserved in a QED vertex. The helicity λ of the $\bar{p}p$ system can be ± 1 or 0, $\lambda = 0$ being suppressed as the CM energy becomes much larger than the proton rest energy. The dominant process is the exchange of one virtual photon, and therefore the total angular momentum J of the initial and final state is 1. It follows that there are six amplitudes describing the process, whose squared moduli have to be summed for unpolarized scattering:

$$\begin{array}{lll} A_{+1,+1}\, d^1_{+1,+1} & A_{0,+1}\, d^1_{0,+1} & A_{-1,+1}\, d^1_{-1,+1} \\ A_{+1,-1}\, d^1_{+1,-1} & A_{0,-1}\, d^1_{0,-1} & A_{-1,-1}\, d^1_{-1,-1}\,. \end{array} \tag{1.21}$$

Parity conservation and charge conjugation symmetry ensure that all $A_{\pm 1,\pm 1}$ are equal. Moreover, the d matrices satisfy the relations:

$$\begin{array}{lllll} d^1_{+1,+1} & = & d^1_{-1,-1} & = & \left(\frac{1+\cos\theta}{2}\right) \\ d^1_{+1,-1} & = & d^1_{-1,+1} & = & \left(\frac{1-\cos\theta}{2}\right) \\ d^1_{0,+1} & = & d^1_{0,-1} & = & \left(-\frac{\sin\theta}{\sqrt{2}}\right) \end{array} \tag{1.22}$$

Therefore, the unpolarized differential cross section contains two terms, the second of which is suppressed as the CM energy increases:

$$\frac{d\sigma}{d\Omega} \propto |A_1|^2 \left(1 + \cos^2\theta^*\right) + |A_0|^2 \sin^2\theta^*. \tag{1.23}$$

The detailed lowest-order QED calculation has been carried out referring to the analog of the diagram depicted in Figure 1.1 and using Equation 1.8 to parameterize the proton-antiproton current (Zichichi et al. 1962). If one indicates with β_p the speed of the (anti)proton in the CM frame,

$$\beta_p \equiv \sqrt{1 - \frac{4m_p^2}{s}}, \tag{1.24}$$

the differential cross section can be written as:

$$\left(\frac{d\sigma}{d\Omega}\right)_{\bar{p}p \to e^+e^-} = \frac{\alpha^2}{4\beta_p s} \cdot \left[|G_M|^2 (1 + \cos^2\theta^*) + \frac{4m_p^2}{s} |G_E|^2 \sin^2\theta^* \right] \quad (1.25)$$

where θ^* is the CM angle between the positron and the antiproton tracks. If the final state particles are detected in a manner that does not distinguish between electron and positron, there is no interference contribution from next-order processes.

At low q^2 in the spacelike region, the Sachs form factors are strictly related to the charge and magnetic moment distributions inside the proton (Section 1.2). Expression 1.25 for the cross section, together with Equation 1.23, emphasizes a relativistic interpretation of G_M and G_E — they are proportional to the helicity conserving and non-conserving amplitudes, respectively.

The cross section of the inverse process has the same angular dependence and differs only by a phase-space factor (principle of detailed balance). It is (Cabibbo and Gatto 1961):

$$\left(\frac{d\sigma}{d\Omega}\right)_{e^+e^- \to \bar{p}p} = \beta_p^2 \cdot \left(\frac{d\sigma}{d\Omega}\right)_{\bar{p}p \to e^+e^-} \quad (1.26)$$

Form factors in the timelike region are not guaranteed to be real. If the beam or the target are polarized, an azimuthal dependence of the cross section arises, allowing to separate the real from the imaginary part. Otherwise, only their moduli can be measured.

1.5 Review of the Timelike Measurements

All the measurements of the timelike magnetic form factor of the proton are briefly described to emphasize the experimental techniques employed and their evolution. The results are summarized in Table 1.1 and in Figure 3.22. From the following discussion, the context in which experiment E-835 operated and the relevance of its data will emerge.

The first timelike experiment was carried out at CERN in 1965, using a partially-separated antiproton beam from the Proton Synchrotron (Conversi et al. 1965). The beam momentum, corresponding to $s = 6.8$ GeV^2, was chosen in order to maximize the number of expected events, taking into account the energy dependence of the antiproton yield and of the cross section. The beam was identified by means of a gas Čerenkov counter, which allowed to reject the dominant pion component. The interactions took place inside a polyethylene target. The two-arm telescope made of plastic scintillators, spark chambers and lead absorbers, was used to select e^+e^- and $\mu^+\mu^-$ final states in the region around 90° in the CM reference frame. After producing about 10^{10} antiproton-proton interactions, no events were observed. Upper limits on the form factors and on the total cross section were published. Assuming $|G_E| = |G_M|$, as it is at threshold, they obtained $\sigma(\bar{p}p \to e^+e^-) < 1.44$ nb (90% CL).

Tab. 1.1: All existent measurements of the magnetic form factor of the proton.

s (GeV^2)	$\lvert G_M \rvert \times 10^2$	N	Lab	Machine	Experiment	Year
3.52	51±8	29	CERN	PS	ELPAR	1977
3.52	53^{+6}_{-8}	1830	CERN	LEAR	PS-170	1994
3.55	39±5	34	CERN	LEAR	PS-170	1994
3.57	34±4	40	CERN	LEAR	PS-170	1994
3.60	31±3	50	CERN	LEAR	PS-170	1994
3.61	46^{+15}_{-9}	5	CERN	PS	ELPAR	1977

continued on next page

continued from previous page

s (GeV^2)	$\|G_M\| \times 10^2$	N	Lab	Machine	Experiment	Year
3.69	36±5	16	Frascati	Adone	FENICE	1994
3.69	28.1±1.4	348	CERN	LEAR	PS-170	1994
3.76	25.5±1.3	375	CERN	LEAR	PS-170	1994
3.8	39±6	16	Orsay	DCI	DM-1	1979
3.83	24.9±1.0	284	CERN	LEAR	PS-170	1994
3.9	25±8	9	Orsay	DCI	DM-1	1979
3.94	24.6±1.1	210	CERN	LEAR	PS-170	1994
4.0	26±3	22	Orsay	DCI	DM-2	1983
4.00	24±3	18	Frascati	Adone	FENICE	1994
4.1	26±3	27	Orsay	DCI	DM-1	1979
4.18	23.7±0.9	496	CERN	LEAR	PS-170	1994
4.2	22±2	24	Orsay	DCI	DM-2	1983
4.4	27±4	25	Frascati	Adone	Castellano et al.	1973
4.4	19±2	20	Orsay	DCI	DM-2	1983
4.41	22±2	28	Frascati	Adone	FENICE	1994
4.6	21±4	11	Orsay	DCI	DM-1	1979
4.6	17±2	17	Orsay	DCI	DM-2	1983
4.8	19±2	19	Orsay	DCI	DM-2	1983
5.0	14±4	3	Orsay	DCI	DM-2	1983
5.1	<20	–	BNL	AGS	Hartill et al.	1969
5.69	$8.4^{+1.7}_{-1.3}$	7	Orsay	DCI	DM-2	1990
5.95	15±3	7	Frascati	Adone	FENICE	1994
6.6	<16	–	BNL	AGS	Hartill et al.	1969
6.8	<25	–	CERN	PS	Conversi et al.	1965
8.9	<5.2	–	CERN	ISR	R-704	1985
8.9	$3.3^{+0.6}_{-0.4}$	14	FNAL	AA	E-760	1993
9.6	21±3	14	DESY	DORIS	DASP	1975

continued on next page

continued from previous page

s (GeV^2)	$\|G_M\| \times 10^2$	N	Lab	Machine	Experiment	Year
12.4	$1.3^{+0.3}_{-0.2}$	11	FNAL	AA	E-760	1993
12.5	<4.2	–	CERN	ISR	R-704	1985
13.0	$1.3^{+0.5}_{-0.3}$	4	FNAL	AA	E-760	1993

In 1969, other upper limits were estabilished by an experiment at the Alternating Gradient Synchrotron operating at Brookhaven National Laboratory, for $s = 5.1$ GeV^2 and 6.6 GeV^2 (Hartill et al. 1969). The incident antiprotons were identified by measuring the time of flight of the beam particles. A long cylindrical flask contained the liquid hydrogen target. The tracking system was based upon hodoscopes and spark chambers. An effective suppression of the pion background was obtained by placing lead-lucite Čerenkov shower counters outside the tracking detectors. No events compatible with the electron-positron hypothesis were found.

The first positive result came in 1973, from head-on electron-positron annihilation at Adone, the storage ring in Frascati (Castellano et al. 1973). An integrated luminosity of about 0.2 pb^{-1} was collected at $s = 4.4$ GeV^2. Several criteria were used to identify the slow proton or antiproton tracks. Range and energy loss measurements were provided by a series of scintillation counters. Coplanarity and collinearity of the tracks were measured with a hodoscope and a spark chamber and contributed to suppress cosmic rays and beam-related background, like other two-body reactions or beam-gas scattering. Cosmic rays were also rejected by looking at the time of the event relative to a signal in phase with the accelerating RF cavity. From the twenty-five events observed, a cross section $\sigma(e^+e^- \to p\bar{p}) = (0.91 \pm 0.22)$ nb was deduced.

Soon after the discovery of the J/ψ, in 1975, a measurement was done at that energy (corresponding to $s = 9.6$ GeV^2) at the electron-positron storage ring DORIS (DESY) by the DASP collaboration (Braunschweig et al. 1975). The goal was to observe two-body hadronic decays of the then called '3.1 GeV resonance'. In particular, the $\pi^+\pi^-$, K^+K^- and $p\bar{p}$ final states were selected, using the magnetic Double Arm SPectrometer, based upon momentum, range, shower and time-of-flight information. Fourteen antiproton-proton events were observed. After normalizing to the $e^+e^- \to \mu^+\mu^-$ cross section, the ratios

$$\frac{\sigma(e^+e^- \to p\bar{p})}{\sigma(e^+e^- \to \mu^+\mu^-)} = \begin{cases} 0.036 \pm 0.010 & \text{(a)} \\ 0.030 \pm 0.009 & \text{(b)} \\ 0.022 \pm 0.006 & \text{(c)} \end{cases} \tag{1.27}$$

were obtained, corresponding to different assumptions on the angular distribution, namely: (a) negligible electric contribution, implying $(1+\cos^2\theta^*)$; (b) a flat distribution; or (c) $|G_M| = 0$, implying $(1 - \cos^2\theta^*)$. Rescaling the previous measurements and limits, a clear excess was found, indicating the relevant role of the resonance in the process; the corresponding value of $|G_M|$ can be compared with values at similar energies in Table 1.1.

The value of the form factor at threshold was measured indirectly in antiproton-proton annihilations at the CERN PS in 1977 (Bassompierre et al. 1976; Bassompierre et al. 1977). This measurement was of particular interest, because at $s = 3.52$ GeV^2 the electric and magnetic form factors are strictly equal; moreover, the measurement was not feasible at electron-positron colliders, because of the phase-space suppression of the cross section (Equation 1.26) and because of the impossibility to detect the proton and the antiproton at rest. The measurement proceeded in two steps. The first phase of the experiment succeeded in discriminating antiprotons annihilating at rest from annihilations in flight in the liquid hydrogen target, with a negligible background. The selection was based upon pulse height in the scintillators and tracking and shower characteristics in the spark chambers. By selecting e^+e^- (29 events), $\pi^+\pi^-$ and K^+K^- (240 events total) final states, the e^+e^- branching fraction at rest could be measured:

$$B_{e^+e^-} = \frac{\Gamma(\bar{p}p \to e^+e^-)}{\Gamma(\bar{p}p \to \text{total})} = (3.2 \pm 0.9) \times 10^{-7} \tag{1.28}$$

The second step consisted in evaluating the total cross section times the antiproton momentum at threshold. That was done by extrapolating existing data taken at low energy, obtaining $(\sigma_{tot} \times p_{lab})_{thr} = (56 \pm 2)$ mb × (GeV/c). From $B_{e^+e^-}$ and the product $(\sigma_{tot} \times p_{lab})_{thr}$, the magnetic form factor at threshold could be deduced. A measurement at $s = 3.61$ GeV^2 was also published by the same experiment, based upon five events. Both measurements rely on the $|G_E| = |G_M|$ hypothesis and on the assumption that e^+e^- and two-hadron events have the same angular distribution.

More data were collected in e^+e^- collisions at DCI (Orsay) starting from 1979 (Delcourt et al. 1979). The energy range scanned corresponds to s between 3.7 and 5.7 GeV^2. The DM1 detector consisted of four cylindrical multiwire proportional chambers inside a solenoid. Outside, a set of liquid scintillator counters was used to reject cosmic rays, which represented the main background. The head-on beam collisions took place in a 30 cm region and an integrated luminosity of 0.4 pb^{-1} was accumulated. A total of 63 $p\bar{p}$ events were observed, using the momentum information and the beam synchronization to identify them; also, the tracks were required to stop in the magnet yoke. The results were grouped in four points.

Three series of runs, corresponding to a total of about 0.7 pb^{-1}, were acquired with the DM2 detector in 1982 and 1984 (Bisello et al. 1983; Bisello et al. 1990). Inside a cylindrical solenoid two multiwire proportional chambers and several layers of drift chambers were placed. Still inside the magnet yoke were a segmented water Čerenkov counter and a series of scintillation counters, used for time-of-flight and energy deposit measurements. Collinear pairs were selected using momentum measurements. The shower detectors outside the solenoid, made of layers of lead, scintillator and streamer tubes, allowed to discriminate between e^+e^- and $\mu^+\mu^-$ pairs. These events served as a normalization for the 112 $p\bar{p}$ events, which were identified by range measurements and by detecting the antiproton annihilation products. Given the wide angular acceptance of the detector ($|\cos\theta^*| < 0.7$), it was possible to observe the angular distribution of the events. The best fit indicated a value of $|G_M|/|G_E| = 0.34$ for $s \leq 5$ GeV^2; but the low statistics still allowed the $|G_E| = |G_M|$ hypothesis to be highly compatible with the data.

The first high statistics data near threshold were collected at the CERN Low Energy Antiproton Ring by experiment PS-170 (Bardin et al. 1991a; Bardin et al. 1991b; Bardin et al. 1994). The number of events observed in that region was increased by more than an order of magnitude. For the first time, a relatively precise measurement of the angular distribution was also possible at different energies. The high-intensity ($\approx 2 \times 10^6$ particles/s) antiproton beam impinged on a liquid hydrogen target, placed in the gap of a C-shaped magnet. Momentum measurement was achieved using the tracking information provided by drift tubes. A ring of gas Čerenkov counters and shower detectors allowed to separate electron and positrons from pion and kaon pairs, which were used for cross-section normalization. Since the antiproton range in liquid hydrogen was well known, the reconstructed vertex position determined the momentum of the incoming antiproton, and annihilations were observed both at rest and in flight. The angular distribution of the events, measured up to $|\cos\theta^*| = 0.8$, was compatible with the $|G_E| = |G_M|$ hypothesis. This experiment revealed a much steeper slope of $|G_M|$ versus q^2 compared to what previous low-statistics experiments seemed to indicate.

Significant improvements in luminosity came from the exploitation of antiproton storage rings and hydrogen jet targets, used at CERN (Baglin et al. 1985) and later at Fermilab (Armstrong et al. 1993). The antiproton storage rings provide stochastically cooled ($\Delta p/p$ better than 10^{-3}) and intense ($\approx 10^{10}$ particles) antiproton beams. The hydrogen jet targets can reach high densities without compromising the beam stability[b]. Cross sections in the picobarn range became accessible, and detectors able to extract such small signals were devised. The high-q^2 region, where quantitative predictions are more easily calculable, began to be open to experimental investigation.

Experiment R-704 at the CERN Intersecting Storage Ring reached instantaneous luminosities of 3×10^{30} cm^{-2} s^{-1} (Baglin et al. 1985). The main goal of the experiment was to study the electromagnetic decays of the charmonium resonances, produced in $\bar{p}p$ annihilations. The detector was therefore apt to identify e^+e^- final states. Each of the two arms of the non-magnetic spectrometer consisted of a tracking system, a gas Čerenkov counter to tag electrons and an electromagnetic calorimeter. An attempt to sample the high-q^2 behavior of the form factors was made, by selecting $s = 8.9$ GeV^2 and $s = 12.5$ GeV^2. No events were observed and upper limits were set.

[b] Because of their relevance for the results presented in this dissertation, the Fermilab Antiproton Source and the E-835 hydrogen jet target are described in more detail in Chapter 2.

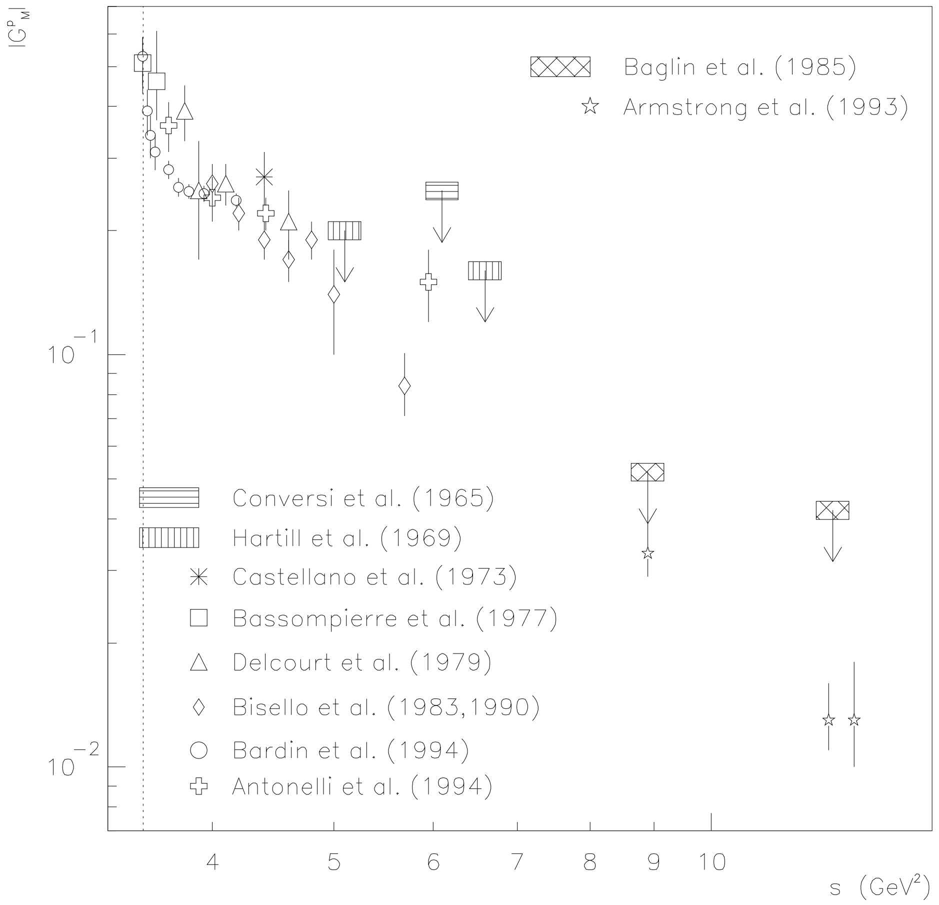

Fig. 1.3: Existing data on the magnetic form factor of the proton. Results corresponding to the $|G_E| = |G_M|$ hypothesis are reported. The cross-hatched rectangles represent upper limits at the 90% confidence level.

Fermilab experiment E-760 had similar goals and used a similar technique, but could exploit better performing beam, target and detectors during its data taking in 1990 and 1991 (Armstrong et al. 1993). The beam stored in the Antiproton Accumulator ($\approx 10^{11}$ particles/store) intersected the hydrogen gas jet target, achieving instantaneous luminosities up to 9×10^{30} cm^{-2} s^{-1}. The interaction region was confined in less than a cubic centimeter. Several charmonium resonances in the range 8.9 GeV$^2 < s <$ 13.0 GeV^2 were scanned with a non-magnetic spectrometer designed to detect electromagnetic final states, like e^+e^-X or $\gamma\gamma$. The cylindrical detector covered the full azimuthal region around the beam axis and the polar interval between approximately 15° and 65° in the laboratory frame. Its main parts were a tracking system (made of two hodoscopes, a straw chamber, a radial projection chamber, a multiwire chamber and two layers of streamer tubes), a threshold Čerenkov detector to identify electrons at the trigger level, and a lead-glass electromagnetic calorimeter. The electron (or positron) tagging was based upon pulse height in one of the hodoscopes, Čerenkov signal, energy deposition in the radial projection chamber and transverse shape of the shower in the calorimeter. A total of 29 background-free e^+e^- events were observed.

Experiment E-835 at Fermilab, whose data and results are the object of this dissertation, used the upgraded E-760 apparatus (Armstrong et al. 1992b). Some important modifications were made for the data-taking run, which lasted from October 1996 through September 1997 and allowed to collect a total of 143 pb^{-1}. The experiment is described in detail in Chapter 2.

Before its final shutdown in 1993, and about twenty years after allowing the first measurement of the timelike form factor to be made, the Adone ring was used by the FENICE experiment to measure the neutron form factor for the first time. The detector was also suitable for observing $p\bar{p}$ final states (Antonelli et al. 1994). It consisted of a central detector and of an antinucleon detector, arranged in an octagonal geometry around the beam pipe. In the central detector were a layer of scintillators for triggering and for time-of-flight measurements, and four planes of streamer tubes, used for tracking. The antinucleon detector was designed to recognize annihilation stars. It was made of iron plates, scintillator slabs and streamer tube planes. Four energy regions were explored, with a total luminosity of about $0.3\ \mathrm{pb}^{-1}$.

1.6 Form Factors in Quantum Chromodynamics. Attempts to Explain the Proton Structure

At present, Quantum Chromodynamics cannot predict the form factors of hadrons. Several approximations and models that are calculable have been devised, all with a limited range of applicability. The difficulties arise from the fact that in the understanding of elastic hadronic processes, both a small and a large distance picture contribute. In other words, asymptotic freedom and the perturbative approach play an important role at high momentum transfer; at the same time, the hadron conserves its identity, so the confinement of quarks and gluons must be taken into account as well. For these reasons, it is considered an interesting and challenging field of theoretical research.

Here, I briefly discuss the approach of valence perturbative QCD. Detailed information and references can be found in the review article by Sterman and Stoler (1997).

Valence perturbative QCD is applicable at high momentum transfer, even though there is no agreement upon how high q^2 has to be. In this regime, the quark masses can be neglected and a first-order perturbative approach in terms of $\alpha_s(q^2)$ is possible. Also, the dominant contributions come from hadronic states with the lowest number of partons (*valence* partons), i. e. $q\bar{q}$ for mesons and qqq for barions. In this framework, the pion form factor[c] can be calculated (Lepage and Brodsky 1980):

$$F_\pi(Q^2) = 16\pi f_\pi^2 \frac{\alpha_s(Q^2)}{Q^2}, \tag{1.29}$$

where $f_\pi \simeq 93$ MeV is a dimensional constant that can be experimentally extracted from the analysis of pion decays. Unfortunately, the existing data on the charged pion form factor is at relatively low Q^2 and it is affected by systematic uncertainties. On the other hand, π^0 data is in good agreement with Equation 1.29 already at $Q^2 \simeq 6$ (GeV/c)^2.

The asymptotic functional form of the proton magnetic form factor versus Q^2 is known up to an overall constant C (Lepage and Brodsky 1980):

$$G_M(Q^2) = \frac{32\pi^2}{9} C^2 \frac{\alpha_s^2(Q^2)}{Q^4} \left(\ln \frac{Q^2}{\Lambda^2}\right)^{-4/27}, \tag{1.30}$$

where Λ is the QCD scale parameter. The running coupling constant, to the leading logarithmic term, can be written as:

$$\alpha_s(Q^2) \simeq \frac{4\pi}{9} \left(\ln \frac{Q^2}{\Lambda^2}\right)^{-1}. \tag{1.31}$$

Asymptotically, the form factors in the timelike region are equal to those in the spacelike region (Gousset and Pire 1995). At lower energies, timelike form factors are approximately twice as large as the spacelike ones, as demonstrated by Gousset and Pire (1995) in the case of mesons; Kroll et al.

[c] Having the pion spin zero, only one form factor is necessary to characterize its electromagnetic properties.

(1993) showed that barion form factors behave similarly, but only within the additional approximations of the quark-diquark model.

As anticipated in Section 1.3, there is good agreement between these semi-quantitative predictions and the data. Obviously, more experimental information and theoretical speculations are necessary in order to fully understand the electromagnetic properties of the proton.

2. EXPERIMENT 835 AT FERMILAB. THE PHYSICS PROGRAM, THE EXPERIMENTAL APPARATUS AND THE DATA COLLECTION SYSTEM

Experiment E-835 is dedicated to the study of charmonium by resonant formation in $\bar{p}p$ annihilations. It has been carried out at the Antiproton Accumulator of Fermi National Accelerator Laboratory. The data-taking run lasted from October 1996 through September 1997, collecting an integrated luminosity of 143 pb^{-1}. In addition to the charmonium physics results, new high-precision measurements of the timelike form factor of the proton at large momentum transfer are extracted from the data.

The apparatus has been designed to detect electromagnetic final states, which are produced by the antiproton beam in the Accumulator intersecting an internal hydrogen gas jet target. It is a non-magnetic spectrometer, whose main components are a lead-glass electromagnetic calorimeter, a threshold Čerenkov counter, and a tracking system.

Several aspects of the experiment are described in detail in this chapter, emphasizing the information relevant to the form factor analysis.

2.1 Physics Program and Experimental Technique

Experiment E-835 is a collaboration of American and Italian institutions[a]; it studies the spectroscopy of charmonium ($\bar{c}c$), the bound state of a quark c and its antiquark (Figure 2.1).

A large amount of experimental data on charmonium spectroscopy has been obtained at electron-positron colliders. Through the annihilation into a virtual photon, only the states $\psi(nS)$ (like the J/ψ or the ψ'), which have the same quantum numbers of the photon ($J^{PC} = 1^{--}$), can be directly formed. The masses and width of these states have been measured with great precision ($\approx$ hundreds of keV for the masses, $\approx$ tens of keV for the widths), since the initial state was very well known. On the other hand, the other charmonium states are studied by observing the spectrum of the emitted photons in the radiative decays of the ψ', like $\psi' \to \chi_c + \gamma$. In these cases, the measurement of masses and widths is limited by the resolution of the photon detector (a few MeV), and is therefore less precise.

In contrast, the formation of all $\bar{c}c$ states is possible in $\bar{p}p$ collisions, through the coherent annihilation of the quarks in the proton with the antiquarks in the antiproton (Cester and Rapidis 1994). The advantage of this technique is that the precision on the measurement of masses and widths only depends on the knowledge of the beam energy and of its momentum spread. The main limitation is that charmonium signals (typically, 10^2 nb) are immersed in the comparatively huge $\bar{p}p$ total cross section ($\simeq$ 70 mb at the J/ψ energy). Therefore, to date, electromagnetic final states have been the only viable method for observing the charmonium resonances.

The resonances are scanned by varying the beam energy in small steps

[a] The complete list of collaborators and other information can be found at `http://www-e835.fnal.gov`.

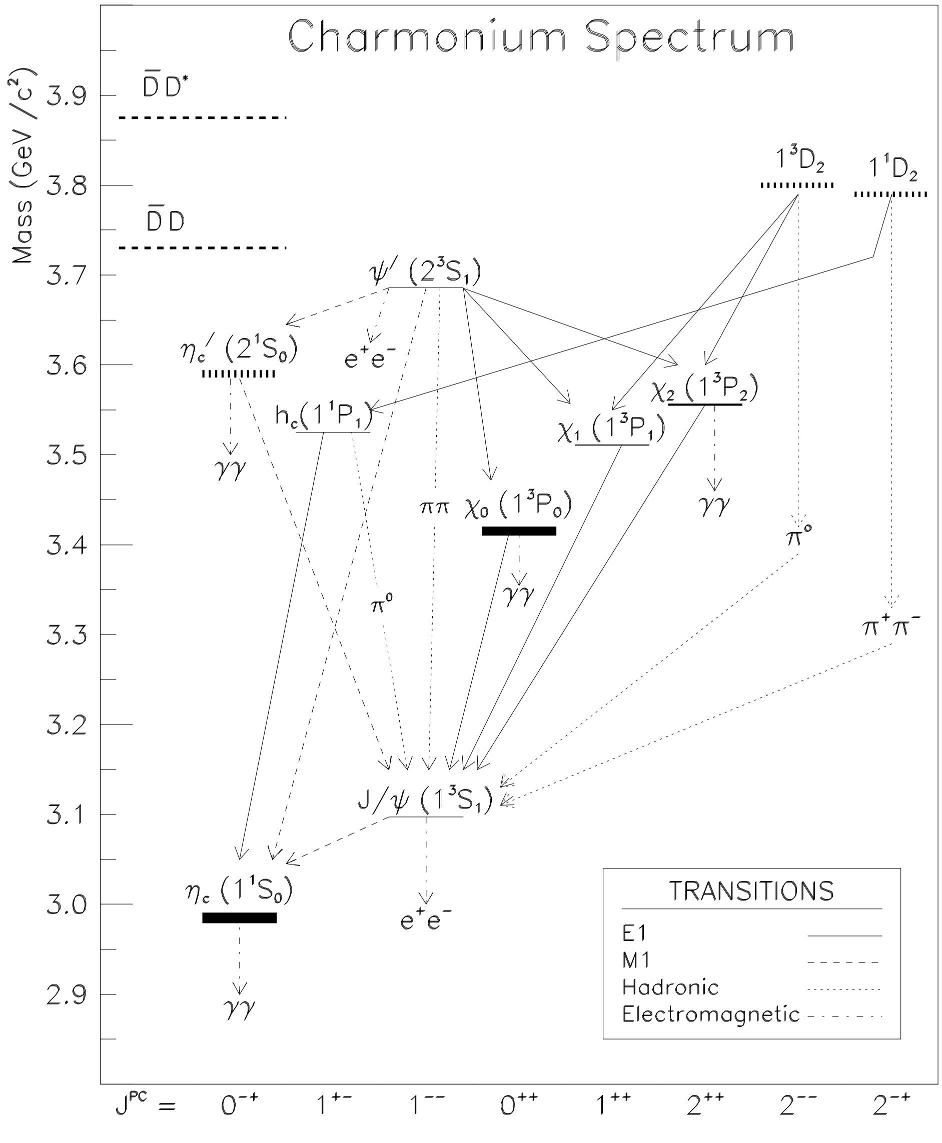

Fig. 2.1: The spectrum of the charmonium system.

and by counting, at each energy point, the number of selected events, typically J/ψ-inclusive (with the J/ψ decaying into e^+e^-) or $\gamma\gamma$.

This technique was proposed by Dalpiaz (1979) and used for the first time in 1984 at the CERN Intersecting Storage Ring by experiment R-704. The promising results prompted the design of experiment E-760 at the Fermilab Accumulator, which could exploit better performing beam, target and detector during its data-taking run in 1990–1991. The E-835 detector is an upgrade of the E-760 one. The new components were designed to cope with the increased instantaneous luminosity.

The success of this experimental technique relies on several factors: good knowledge of the beam energy and of its momentum spread, high luminosity, electron/positron identification and hadron rejection at the trigger level, efficient off-line electron reconstruction and precise calorimetry.

Some of these aspects are fundamental for the study of timelike form factors, especially the high luminosity and the low-background electron identification. This series of experiments, E-835 in particular, turned out to provide unique opportunities for studying the magnetic form factor of the proton in the charmonium region ($8 \lesssim s \lesssim 19$ GeV^2), which is the highest q^2 region explored to date, as shown in Section 1.5. Within that region, the choice of luminosity spent at each energy point has been determined by the charmonium physics goals. The results of R-704 and E-760 have been reported by Baglin et al. (1985) and Armstrong et al. (1993), respectively. In this dissertation, I present the results extracted from the E-835 data.

2.2 The Interaction Region: Beam, Target and Luminosity

(a) The Machine

The Fermilab Antiproton Accumulator is a unique machine. Besides its main role as storage ring for $\bar{p}$s to be employed in the Tevatron collider program, it can provide, at lower energies, a high-quality beam of antiprotons, which is desirable for both charmonium and form factor physics. After the shut-down of the CERN Antiproton Accumulator, the Fermilab machine is presently the only one in the world that can play this role[b].

(b) Antiproton Production

A single batch of protons with an intensity of about 3×10^{12} particles is accelerated to 120 GeV in the Main Ring. The eighty-two bunches contained within the batch are extracted from the Main Ring by means of a kicker and transported to the target vault through the AP-1 line (Figure 2.2).

The incident beam is focused to a small spot size using conventional quadrupole magnets and impinges upon the production target, which consists of a stack of nickel disks. The mechanical characteristics of the target (thickness, shape, material, capability of being displaced and rotated) are aimed at limiting the phase space spread of the secondary particles, without compromising the structural integrity of the target itself.

The resulting cone of secondaries is focused by means of a lithium lens, which is a cylinder through which an intense current is forced (Figure 2.3). Lithium is chosen to minimize the absorption of particles passing through

[b] The importance and the operation principles of both antiproton accumulators has been recently discussed by Church and Marriner (1993).

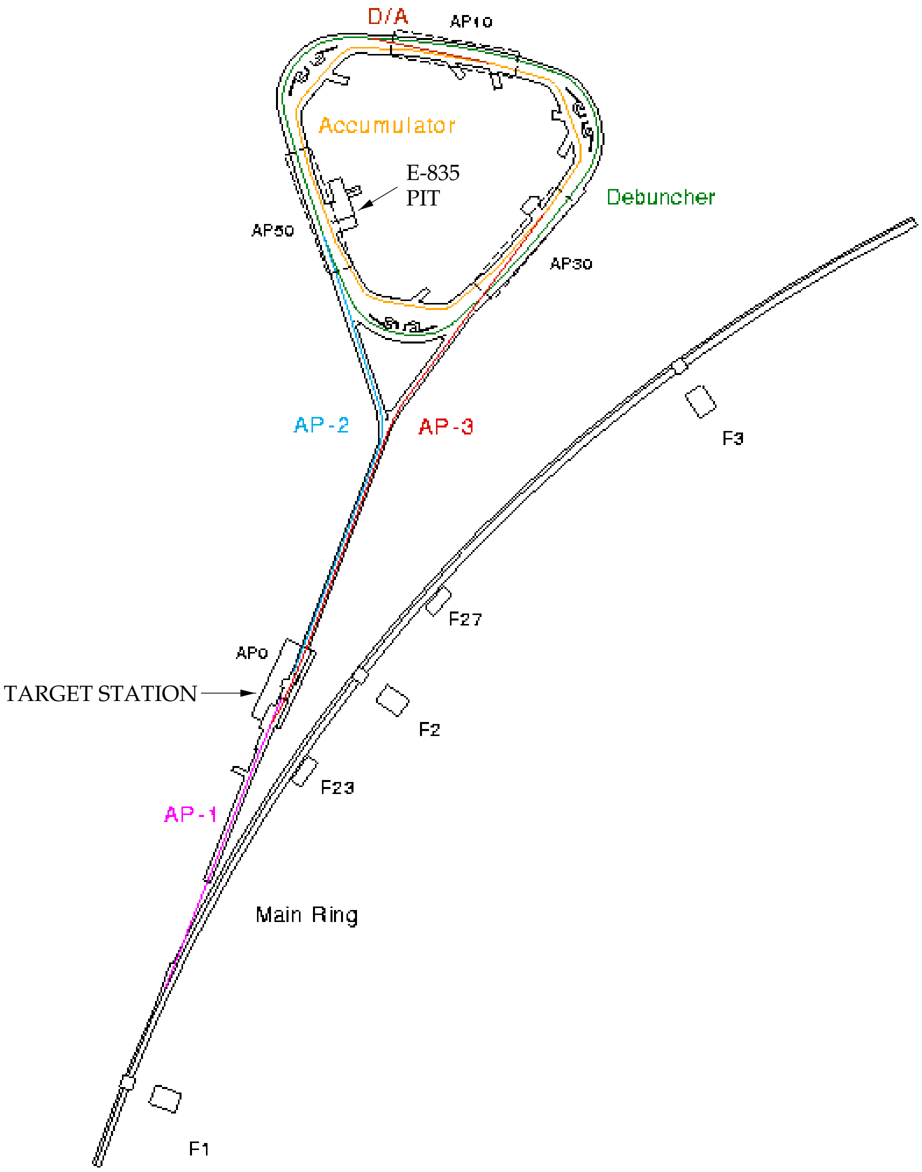

Fig. 2.2: Layout of the Antiproton Source.

the lens. The main advantage of using this kind of lens (compared to quadrupole magnets, for instance) is that one achieves focusing in both the horizontal and vertical planes in a very short distance. At this stage, the time structure of the beam coming off the lens is the same as that of the primary proton beam.

A pulsed dipole magnet bends all particles with the magnetic rigidity p/e of an 8.9 GeV/c antiproton into the AP-2 line, while all other particles are absorbed within a beam dump. The energies of the incident protons and of the collected secondaries are chosen in order to maximize the inclusive antiproton yield, compatibly with the machine constraints.

Particles that survive the trip down the AP-2 line are injected into the Debuncher where they coast for about two seconds. Most of the secondaries decay either in the AP-2 line or in the Debuncher, while electrons are lost due to bremsstrahlung; what is left is solely antiprotons.

On average, about 10^5 protons are needed to obtain a single antiproton. The main causes of inefficiency are the production cross section

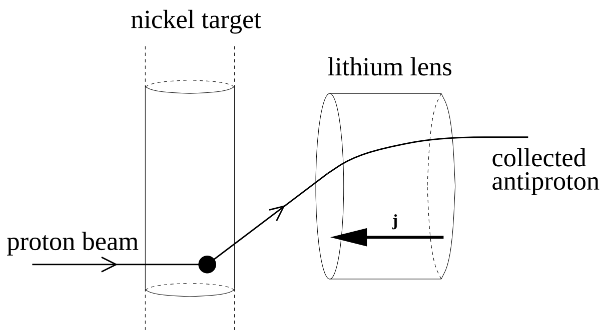

Fig. 2.3: Schematics of the target disks and of the collection lens used for antiproton production. The horizontal and vertical axes are not drawn to scale. The lens is 15 cm long and its diameter is 2 cm.

and the phase-space spread of the outcoming antiprotons. The angular spread depends intrinsically on the production mechanism, while the position spread can be controlled by focusing the impinging beam to the smallest possible spot. The momentum aperture of the collection system ($\Delta p/p = 4\%$) also constrains the production efficiency.

In the Debuncher, the momentum spread $\Delta p/p$ of the beam is reduced from 4% to 0.2% through bunch rotation and adiabatic debunching. Betatron (transverse) stochastic cooling is then applied so as to reduce the transverse size of the $\bar{p}$ beam. Momentum (longitudinal) cooling is also applied to further reduce the momentum spread to about 0.1%. Pre-cooling in the Debuncher is done for two reasons: to provide for more efficient momentum cooling in the Accumulator and because of the limited momentum aperture of the Accumulator at injection.

Just before the next pulse arrives from the target, the antiprotons are extracted from the Debuncher and injected into the Accumulator via the D-to-A line. Successive pulses of antiprotons are stacked into the Accumulator core by means of RF deceleration and momentum stochastic cooling. The RF moves (decelerates) the freshly injected pulses of antiprotons from the injection orbit inwards to the edge of the stack tail, the low density portion of the stacked beam. The stack-tail momentum cooling system sweeps the beam deposited by the RF away from the edge of the tail and moves it toward the dense portion of the stack, known as the core, which is close to the inside edge of the Accumulator. Antiprotons are confined in the core by additional longitudinal and transverse cooling.

Antiprotons are stacked for several hours at an average stacking rate of about 3×10^{10} $\bar{p}$/hour, until the desired number, typically 5×10^{11} $\bar{p}$, is achieved.

Over a stacking cycle, this procedure allows to increase the phase-space density of the antiproton beam by a factor of 10^5, somehow compensating for the poor production rate of antiprotons. Instantaneous luminosities comparable with those achievable with proton beams are accessible, both in collider and in fixed-target experiments.

(c) Beam Energy

For the E-835 data taking, the Accumulator operates in an unconventional manner. After stacking at 8.9 GeV, the beam needs to be decelerated so that collisions with the protons in the target take place at the desired CM energy, corresponding to the particular charmonium resonance under study (Table 2.1). Often, for instance in the case of the η_c and of the J/ψ, the transition energy of the machine ($\gamma_t = 5.430$, corresponding to $\sqrt{s} = 3.365$ GeV) has to be crossed.

The deceleration is carried out at a rate of about 20 MeV/s and con-

Charmonium Resonance	Formation Energy (GeV)	Beam Momentum (GeV/c)
$\eta_c(1^1S_0)$	2.980	3.676
$J/\psi(1^3S_1)$	3.097	4.066
$\chi_{c0}(1^3P_0)$	3.417	5.201
$\chi_{c1}(1^3P_1)$	3.511	5.550
$\chi_{c2}(1^3P_2)$	3.556	5.725
$\psi'(2^3S_1)$	3.686	6.232

Tab. 2.1: Antiproton beam momentum corresponding to the formation energy of some charmonium resonances. Their masses are taken from Caso et al. 1998.

sists of several steps or ramp points. The deceleration ramp is an empirical table of magnet currents for each beam energy. After each step, the accelerator parameters, such as the orbit, the tunes, the dispersion and the chromaticity, are measured and possibly corrected. Once the desired energy is reached, the jet target is turned on and the data taking begins.

The CM energy $\sqrt{s}$ is calculated from the beam energy[c] E_{beam}, which in its turn is obtained by measuring the revolution frequency f and the orbit length L of the beam; the product $f \cdot L$ is the speed β of the antiprotons:

$$\begin{aligned} \sqrt{s} &= \sqrt{2} m_p \, (1+\gamma)^{1/2} \\ \gamma &= E_{beam}/m_p = \left(1-\beta^2\right)^{-1/2} \\ \beta &= fL. \end{aligned} \tag{2.1}$$

The relative error on the CM energy is the sum in quadrature of the relative errors on the revolution frequency and on the orbit length, multiplied by an energy-dependent factor:

$$\frac{\delta\sqrt{s}}{\sqrt{s}} = \left[\frac{\beta^2\gamma^3}{2\,(1+\gamma)}\right] \cdot \sqrt{\left(\frac{\delta f}{f}\right)^2 + \left(\frac{\delta L}{L}\right)^2}. \tag{2.2}$$

In the charmonium region, this factor varies between 5 and 45, as shown in Figure 2.4. The length of the Accumulator is 474 m, making the revolution frequency approximately 0.6 MHz. This means that, in order to get a CM energy error of $\approx 10^2$ keV one has to know f to about one Hertz and L to about one millimeter[d].

The Schottky noise of the beam is suitable for such high-precision measurements of the revolution frequency. It is also used to monitor the mo-

[c] The speed of the molecules of the jet target (~ 800 m/s) can be neglected.

[d] Such small uncertainty is required for some of the charmonium resonances, but it is not necessary for the form factors, for which different energy regions can be combined together.

mentum spread of the beam, through the relation

$$\frac{\Delta p}{p} = \frac{1}{\eta}\frac{\Delta f}{f}, \tag{2.3}$$

where η is the slip factor of the machine. The beam energy spread, as measured from the Schottky spectrum, is shown in Figure 2.5 for each data-taking run[e].

The orbit length is calibrated by scanning the ψ' resonance, whose mass is known with an uncertainty of 90 keV and where the factor defined in Equation 2.2 is relatively large. A reference orbit with length $L_0 = 474.050 \pm 0.001$ m is defined, and the values read out by the Beam Position Monitors (BPMs) are recorded. For all other energies, the orbit length $L = L_0 + \Delta L$ is computed by comparing the readings of the BPMs with the reference ones, in order to measure ΔL. This is possible because

[e] The first bin (null energy spread) contains the seventy-one runs for which the link between the accelerator network and the data-acquisition system failed. The data was not recorded, but the frequency spectrum had been checked on-line.

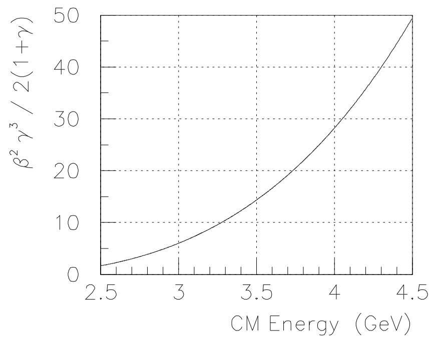

Fig. 2.4: The energy dependence of the error amplification factor defined in Equation 2.2

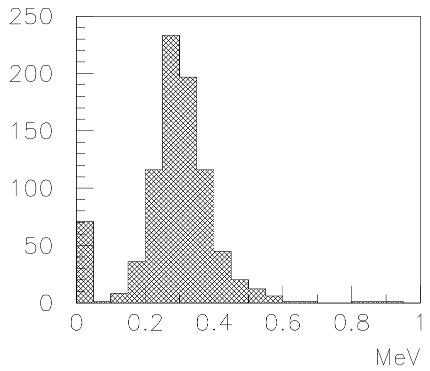

Fig. 2.5: The CM energy spread of the beam for each of the 866 data-taking runs.

ΔL is related to the orbit displacements inside the 38 dipole magnets, which in their turn can be computed by knowing the lattice functions and the displacements at the 48 horizontal BPMs, measured with an uncertainty of half a millimeter (Garzoglio 1998).

With this procedure, the CM energy can be determined to less than a hundred keV. Due to a malfunction of some of the BPM systems for part of the run, a significant systematic error must be taken into account. For the present analysis, one can rely on the fact that the total error $\delta\sqrt{s}$ never exceeds 2 MeV; its systematic impact on the form factor (measured by the slope $d|G_M|/d\sqrt{s}$) is still negligible compared to the total measurement error $\delta|G_M|$ on the form factor itself:

$$\delta|G_M| \gg \left|\frac{d|G_M|}{d\sqrt{s}}\right| \cdot \delta\sqrt{s}, \qquad (2.4)$$

as can be deduced, for instance, from Figure 3.22.

(d) The Jet Target

Since antiproton beams are a precious resource, it is particularly important to use them efficiently, especially when the process under study has a low cross section and the total integrated luminosity is a relevant factor. An internal hydrogen gas jet target is suitable for this task.

The E-835 target (Allspach et al. 1998) intersects the circulating antiproton beam, as shown in Figure 2.6. The helium refrigerated expansion stage causes the formation, inside the nozzle, of H_2 cluster streams with densities up to $\rho = 3.2 \times 10^{14}$ atoms/cm^3. The core of the cluster stream is selected by aligning the movable nozzle with two skimmers. A series of pumps (not shown in the figure), in conjunction with the alignment system of the jet, maintains a low level of background gas inside the beam pipe.

Consequently, the antiproton stochastic cooling is sufficient to contain the beam emittance growth due to the presence of the target itself.

The total transverse width of the jet at the interaction point is less than 7 mm, as inferred from measurements of the density profile (Figure 2.7a).

In Figure 2.7b, the set of operating conditions is shown. For each value P of the pressure[f], the corresponding temperature T (open circles, right vertical axis) and density ρ (full circles, left axis) are plotted. The closer the P-T points (open circles) are to the saturation curve, the higher the achieved density is. A trade-off is found between high density and the possible formation of liquid, which could freeze and obstruct the nozzle.

During a data-taking run, as the beam current decreases, the target density is varied so as to keep the instantaneous luminosity constant, around 2×10^{31} cm^{-2} s^{-1}. This value is close to the maximum rate that the data-acquisition system can keep up with; therefore the integrated luminosity

[f] 1 psi = 6.9×10^3 Pa; 14.7 psi = 1 atm

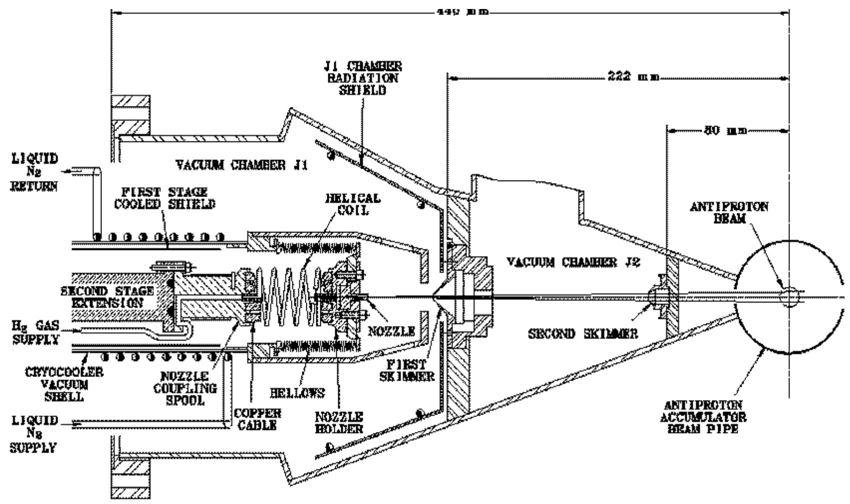

Fig. 2.6: Schematics of the internal hydrogen gas jet target.

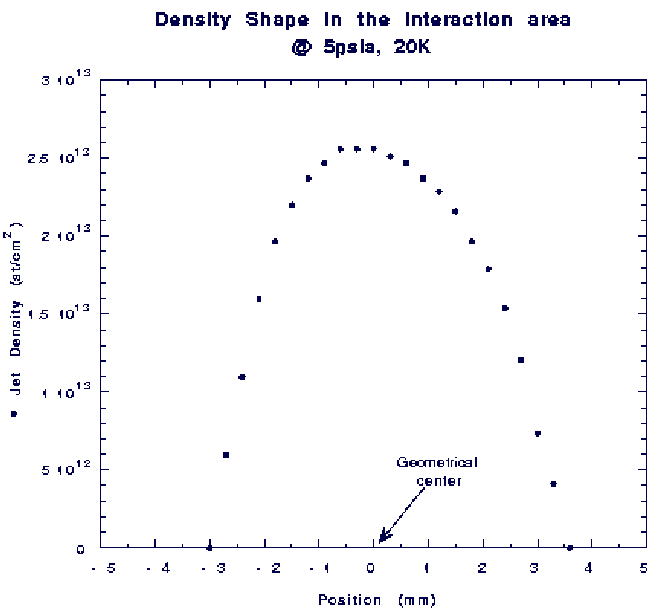

(a)

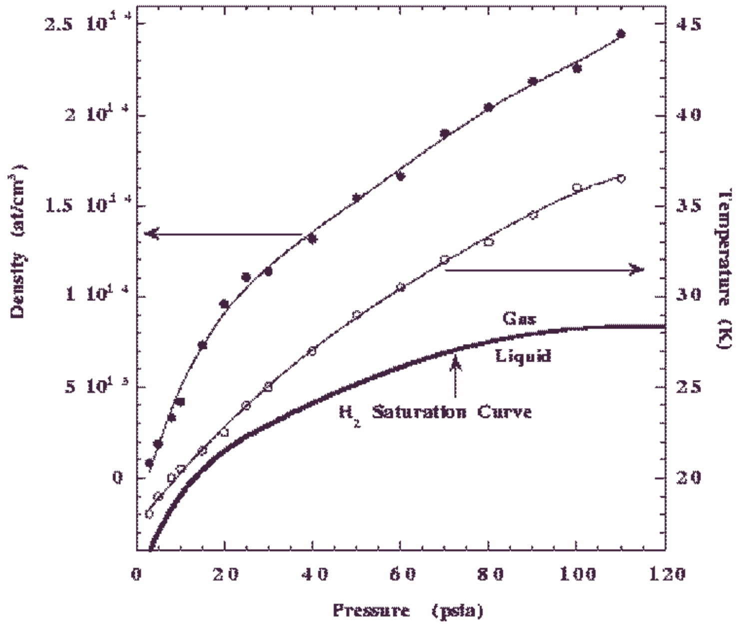

(b)

Fig. 2.7: Jet target performance: (a) Density profile of the cluster stream. (b) Target density as a function of pressure and temperature.

collected by the experiment is maximized.

(e) Accumulated Luminosity

Luminosity measurement. The luminosity is measured by observing the recoil protons corresponding to forward angle elastic scattering of antiprotons.

The number N of protons scattered within the solid angle Ω in a given time interval is proportional to the integrated luminosity L:

$$N = L \int_{\Omega} \left(\frac{d\sigma}{d\Omega} \right) d\Omega, \tag{2.5}$$

where $d\sigma/d\Omega$ is the $\bar{p}p$ elastic differential cross section, which has been measured with good accuracy in the energy range of interest for E-835 (Armstrong et al. 1996).

The luminosity monitor (Trokenheim et al. 1994; Pedlar 1998) is located about 150 cm below the interaction point, at a polar angle of 86.4° (Figure 2.8 and Figure 2.11). It consists of three solid state detectors, enclosed

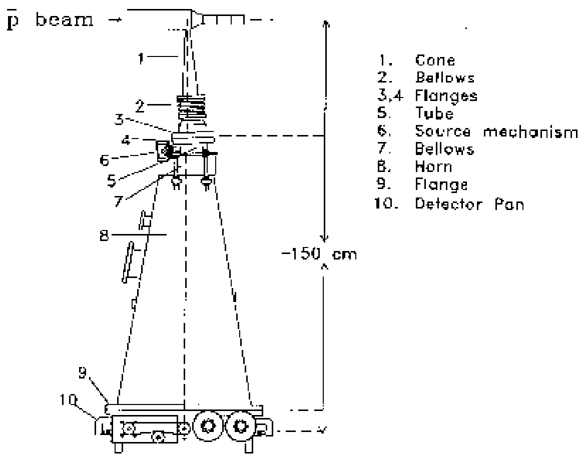

Fig. 2.8: Layout of the luminosity monitor.

in a vacuum vessel directly coupled to the beam pipe. The presence of three devices allows to detect possible horizontal displacements of the beam; it also provides redundancy in case of failure of one of them. One of the detectors sits on a movable tray and is situated directly beneath the beam axis. The other two are fixed and lie on either side. The active surface of the three detectors is 1×5 cm^2; their thickness is 0.5 mm.

In the angular region covered by the detectors, the scattered protons possess a kinetic energy that varies between 3 MeV and 7 MeV (depending strongly upon the beam momentum and upon the scattering angle), which correspond to a penetration range smaller than 0.4 mm.

The analog signal from each detector is sent to an ADC and then to a histogramming memory, which acts as a multichannel spectrum analyzer. Each of its four channels has 8192 24-bit bins. Every two minutes, and at the start and finish of each data-taking run, the contents of the histogramming memory are recorded and then reset to zero.

About 10^5 events are present in the elastic recoil peak for 10^2 nb^{-1} of integrated luminosity. Figure 2.9 shows a typical energy spectrum. Each

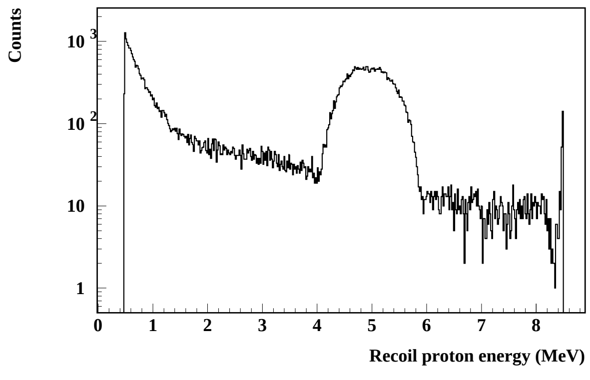

Fig. 2.9: Energy spectrum of recoil protons detected by the luminosity monitor (description in the text).

bin is 17.4 keV wide. Data were taken at the energy of the χ_{c2} resonance (run number 695, $\sqrt{s} = 3556.56$ MeV, instantaneous luminosity $\mathcal{L} = 1.7 \times 10^{31}$ cm^{-2} s^{-1}), corresponding to a total of 36.8 nb^{-1}.

The uncertainty on each luminosity measurement is less that 3%; the main source of error (2%) is the value of the differential cross section.

Running conditions. Typically, data are taken at an instantaneous luminosity $\mathcal{L}$ of 1.9×10^{31} cm^{-2} s^{-1} (above the transition energy of the machine, $\sqrt{s} = 3.365$ GeV) or 0.9×10^{31} cm^{-2} s^{-1} (below transition). The difference is mostly due to the fact that transition crossing is more efficient with smaller-sized beams; therefore, it was chosen to use antiproton stacks of modest intensity (~ 20 mA, corresponding to 2×10^{11} particles) for low-energy data-taking. Figure 2.10a shows the instantaneous luminosity versus the CM energy for all runs; the areas of the boxes are proportional to the amount of data (ie total luminosity) collected at each value of $\sqrt{s}$ and $\mathcal{L}$.

During the whole E-835 run, which lasted for about one year, the experiment has accumulated 143 pb^{-1}. In Figure 2.10b, the integrated luminosity as a function of time is reported.

2.3 The Detector

The E-835 apparatus has been designed to detect electromagnetic final states. It makes use of some of the components employed in experiment E-760 (Armstrong et al. 1993) as well as several upgrades. The layout of the detector is shown in Figure 2.11. It is a non-magnetic spectrometer with full azimuthal (ϕ) coverage and polar angle (θ) acceptance ranging from 2° to 70°. The central detector ($15° < \theta < 65°$) has cylindrical symmetry around

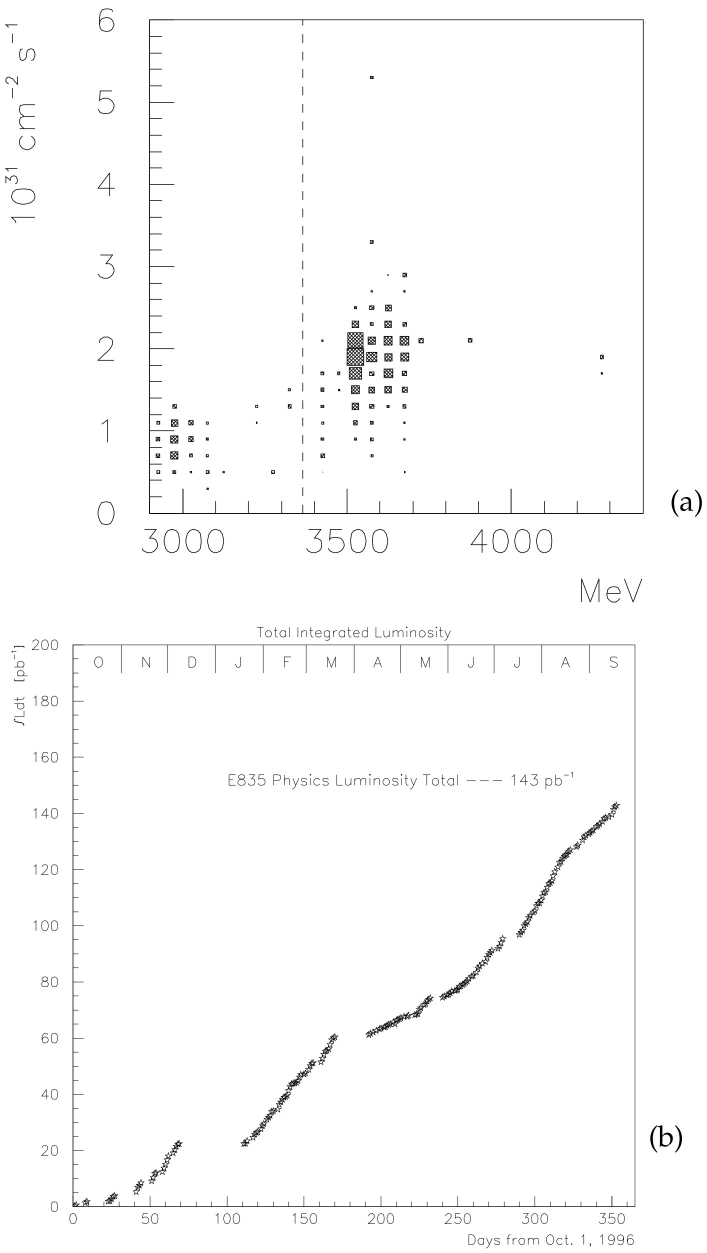

Fig. 2.10: E-835 luminosity. (a) The instantaneous luminosity versus the CM energy. The vertical dashed line represents the transition energy of the antiproton accumulator. (b) The integrated luminosity accumulated throughout the data-taking run.

the beam axis; its main components are the lead-glass electromagnetic calorimeter (CCAL), the threshold gas Čerenkov counter and the inner tracking system.

Upstream ($\theta = 65°$), the polar coverage is limited by constraints of space (jet target and luminosity monitor equipment). Given these constraints, the choice of the downstream edge of the detector ($\theta = 15°$) represents a compromise between several factors: the geometrical acceptance for the reactions of interest, mostly $\bar{p}p \to \gamma\gamma$, $\bar{p}p \to e^+e^-$ and $\bar{p}p \to J/\psi + X \to e^+e^- + X$; the interaction and trigger rates; the radiation damage, especially in the lead glass; the speed of the hadrons in the final state, which affects the rejection power of the Čerenkov counter.

(a) Electromagnetic Calorimeter

The central calorimeter (CCAL) (Bartoszek et al. 1991) measures the energy and direction of photons, electrons and positrons.

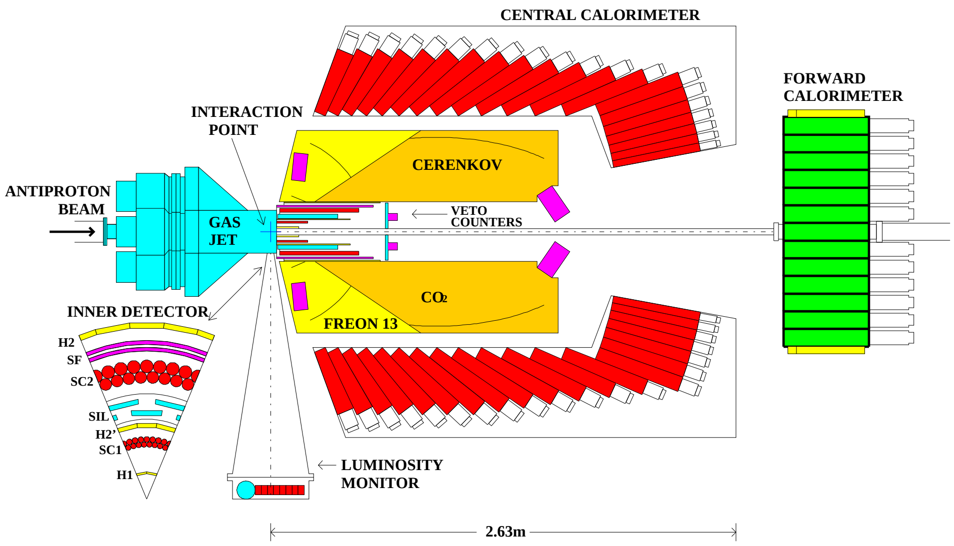

Fig. 2.11: The E-835 Detector.

Block Number	Block Length (cm)	Central θ (deg)	Block Width (deg)	Distance from Target (cm)	PMT Diameter (inches)	Fractional PMT Coverage
01	37.80	67.387	5.226	72.44	3.0	0.473
02	38.65	62.259	5.031	75.87	3.0	0.475
03	39.88	57.342	4.803	80.07	3.0	0.476
04	41.50	52.664	4.552	85.08	3.0	0.478
05	43.54	48.246	4.284	90.96	3.0	0.479
06	46.03	44.101	4.007	97.79	3.0	0.481
07	48.98	40.234	3.728	105.62	3.0	0.482
08	50.00	36.644	3.451	114.54	3.0	0.497
09	50.00	33.327	3.183	124.66	3.0	0.520
10	50.00	30.273	2.925	136.07	3.0	0.544
11	50.00	27.472	2.679	148.89	3.0	0.568
12	50.00	24.908	2.449	163.26	3.0	0.593
13	50.00	22.567	2.233	179.34	3.0	0.617
14	50.00	20.434	2.033	197.28	3.0	0.641
15	50.00	18.493	1.848	197.29	2.5	0.546
16	50.00	16.730	1.678	197.29	2.5	0.664
17	50.00	15.130	1.522	197.30	2.0	0.527
18	50.00	13.679	1.380	197.30	2.0	0.644
19	50.00	12.364	1.250	197.30	1.5	0.443
20	50.00	11.174	1.131	197.30	1.5	0.543

Tab. 2.2: Dimensions, positions and photomultiplier characteristics of the 20 lead-glass blocks within each of the 64 CCAL wedges.

One of the most important CCAL design goals is an effective background rejection. The neutral electromagnetic final states of charmonium formed in $\bar{p}p$ annihilations are immersed in a hadronic background, which consists mostly of neutral pions decaying into two photons. Identifying and rejecting these events requires: (a) good position resolution, which implies fine segmentation; (b) sensitivity to low-energy showers, which limits the thickness of the detector. In fact, high position resolution is necessary for symmetric pion decays, ie when the two emerging photons have approximately the same energy; on the other hand, a low energy threshold is important when the decay is asymmetric.

The calorimeter is a matrix of 1280 lead glass Čerenkov counters (64 *wedges* in ϕ by 20 *rings* in θ, shown in Figure 2.12), read out with photomultiplier tubes (PMTs). Each block is pointing towards the interaction region. The thickness of the blocks, expressed in radiation lengths ($X_0 = 3.141$ cm), varies between $12X_0$ and $16X_0$. In Table 2.2 some of the mechanical characteristics of the CCAL are reported.

The angular resolution is 11 mrad in ϕ and 6 mrad in θ; it includes the uncertainty on the location of the interaction vertex. The average energy resolution is $\sigma_E/E = 1.4\% + 6\%/\sqrt{E(\mathrm{GeV})}$.

The signal from each block is sent to a shaper board and then to an ADC. Each CCAL channel is also equipped with a time-to-digital converter (TDCs), which provides the timing information needed to reject pile-up clusters. For showers with energy above 80 MeV, the time is always recorded; they are classified as 'in time' or 'out of time'. Clusters with smaller energies are identified as 'undetermined' if such information is missing.

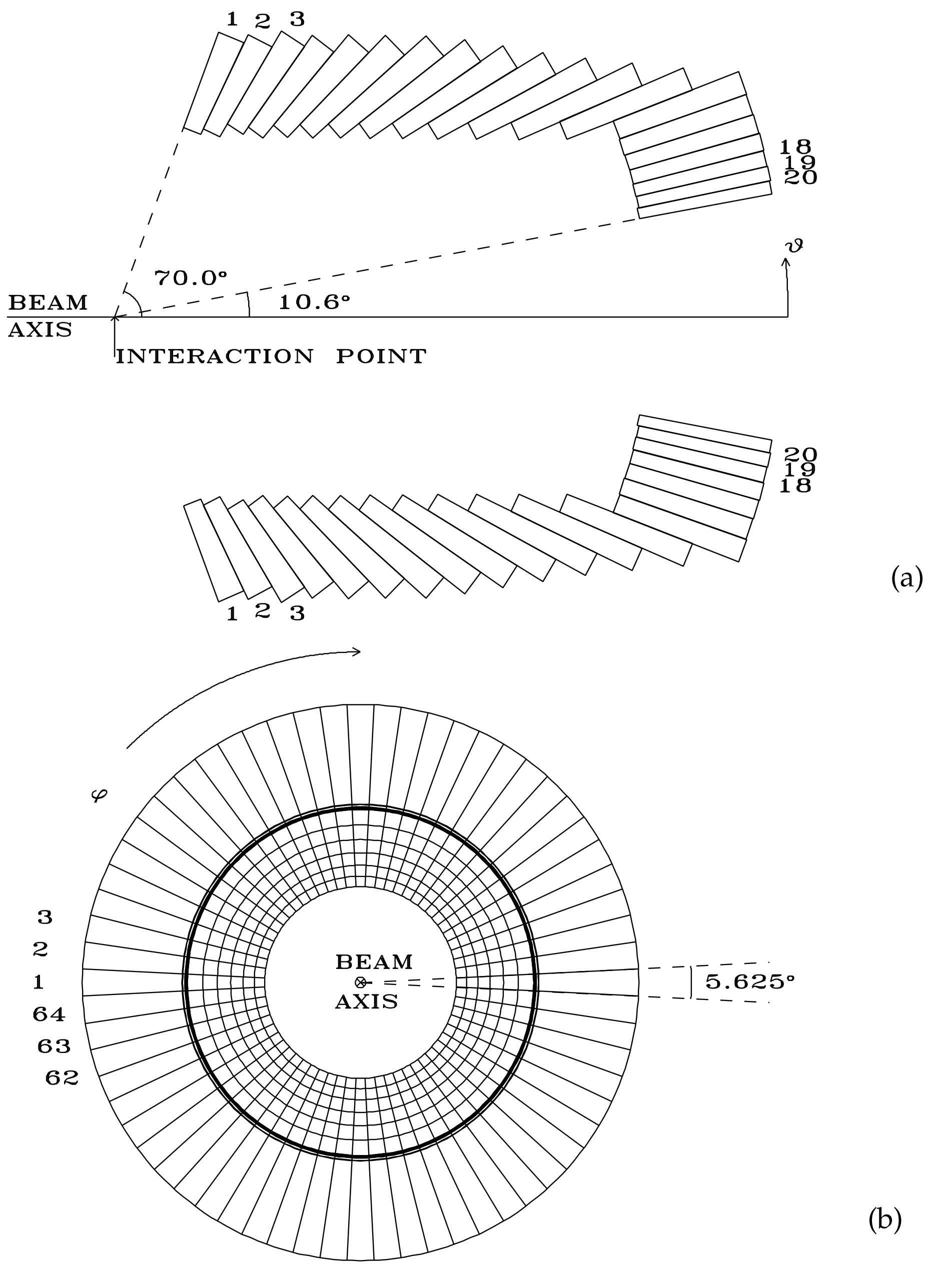

Fig. 2.12: Central calorimeter layout. (a) The side view shows the 20 rings. (b) Cross section showing the 64 wedges.

(b) Čerenkov Counter

The threshold gas Čerenkov counter (Biino et al. 1992; Bagnasco et al. 1998b) is used for identifying electrons and positrons. It has been designed to reject pions and heavier particles both at the trigger level and off-line.

The counter occupies a cylindrical sector around the beam pipe (inner radius = 17 cm, outer radius = 59 cm). It consists of 16 gas tight cells (two in θ by eight in ϕ), covering the whole azimuth and the polar region between 15° and 65°. Each cell is equipped with a photomultiplier tube and is read out by an ADC and a TDC. Figure 2.13 shows a schematic diagram of a sector the counter. Some of its characteristics are summarized in Table 2.3.

The faster particles that must be rejected are the pions from $\bar{p}p \to \pi^+\pi^-$. The relativistic factor $\gamma_\pi = (1 - \beta_\pi)^{-1/2}$ of these pions as a function of the laboratory angle θ is plotted in Figure 2.14. The curves correspond

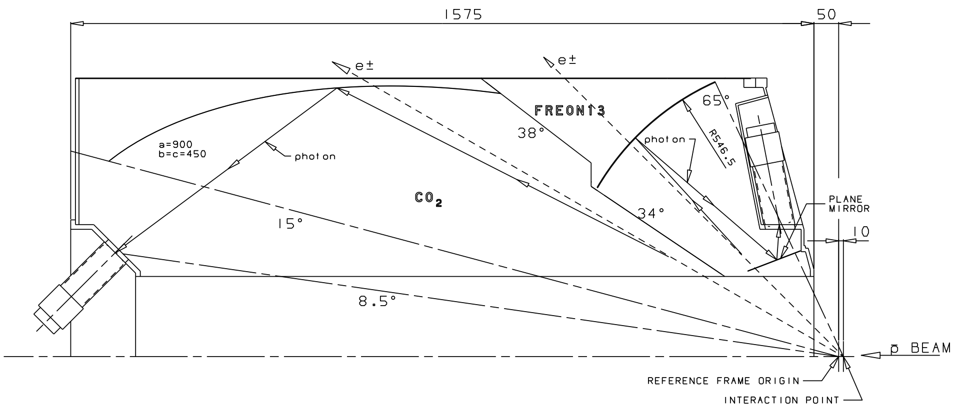

Fig. 2.13: Schematic side view of the Čerenkov counter. One of the downstream cells (CO_2 gas, elliptical mirror) and one of the upstream cells (Freon-13 gas, spherical mirror) are visible. Dimensions are in mm.

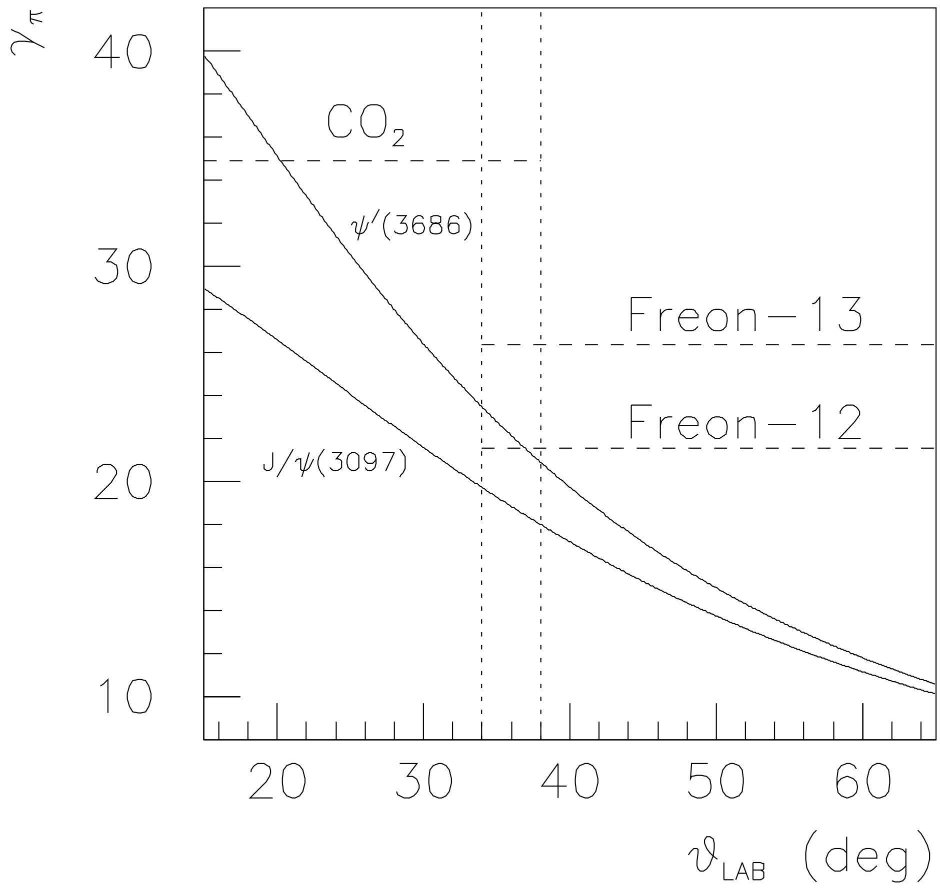

Fig. 2.14: The relativistic factor γ_π as a function of the polar angle θ for pions from $\bar{p}p \to \pi^+\pi^-$ at two different CM energies. The vertical dotted lines represent the edges of the cells. The three horizontal dashed segments indicate the pion thresholds for each gas.

to the formation energies of the J/ψ ($\sqrt{s} = 3.097$ GeV) and of the ψ' ($\sqrt{s} = 3.686$ GeV). Two different gases at room temperature and atmospheric pressure are used in the cells: (a) CO_2 downstream ($15° < \theta < 38°$), where particles are faster and where the thickness of the radiator is longer; (b) Freon-13 (CF_3Cl) upstream ($34° < \theta < 65°$), so that the shorter radiator length is compensated by a higher index of refraction[g].

The limited size of the interaction region and the small value of the Čerenkov angle θ_c, make it possible to use a relatively straightforward light collection system. In the upstream cells, a spherical and a plane mirror direct the light towards the photomultiplier tube, located in a recess on the wall of the cell. In each of the downstream cells is an ellipsoidal mirror; one of its foci lies in the interaction region, while the other one coincides with the face of the PMT. The light collection efficiency reported in Table 2.3 includes the geometrical acceptance (calculated), the transmittance of the radiator (calculated) and the reflectance of the mirrors (measured).

[g] During the last month of data taking, Freon-12 (CF_2Cl_2) was used instead of Freon-13. The performance of the detector did not change significantly.

Characteristics	Downstream Cells	Upstream Cells	
Polar Coverage	15°–38°	34°–65°	
Azimuthal Segmentation	$45° \times 8$	$45° \times 8$	
Radiator Length	93–72 cm	34–39 cm	
Gas at STP	CO_2	Freon-13	Freon-12
Index of Refraction $(n-1)$	4.1×10^{-4}	7.2×10^{-4}	10.8×10^{-4}
θ_c from $\cos\theta_c = 1/n$	1.64°	2.17°	2.66°
Pion Threshold (GeV/c)	4.873	3.677	3.003
Light Collection Efficiency	0.84–0.90	0.84–0.98	0.75–0.88

Tab. 2.3: Characteristics of the Čerenkov counter.

Characteristics	Scintillating Fibers	Clear Fibers
Type	Kuraray	Kuraray
	SCSF-3HF-1500 Multiclad	Multiclad
Diameter (μm)	835	835
Core Diameter (μm)	740	740
Length (m)	$\simeq 0.95$	$\simeq 2.2$
Attenuation Length (m)	5.5±0.3	10.4±0.5

Tab. 2.4: Fiber characteristics.

The detection efficiency of the counter has been measured with a sample of clean events $\bar{p}p \to e^+e^-$ and $\bar{p}p \to \chi_{c2} \to J/\psi + \gamma \to e^+e^- + \gamma$, selected with no requirements on the Čerenkov counter itself. It comes out to be $(98.1 \pm 0.5)\%$.

Besides the overall light collection efficiency, the average number of photoelectrons $\langle n_{phe} \rangle$ collected per electron or positron depends upon the thickness of the radiator, the speed of the particle and the quantum efficiency of the PMTs. The one-photoelectron equivalent in ADC counts has been measured periodically by recording the thermal noise spectrum of the PMTs. The average number of photoelectrons is $\langle n_{phe} \rangle = 14$–$16$ for the downstream cells and $\langle n_{phe} \rangle = 8$–$9$ for the upstream cells.

(c) Scintillating Fiber Tracker

The main purpose of this 860-channel cylindrical tracker (Ambrogiani et al. 1997; Ambrogiani et al. 1998) is to measure the polar angle θ of charged tracks with high precision, in the region $15° < \theta < 65°$. Its prompt signal is also used in the first level trigger, to select hadronic channels (like $\bar{p}p$ elastic or $\bar{p}p \to \phi\phi \to K^+K^-K^+K^-$) based upon their kinematic characteristics. In

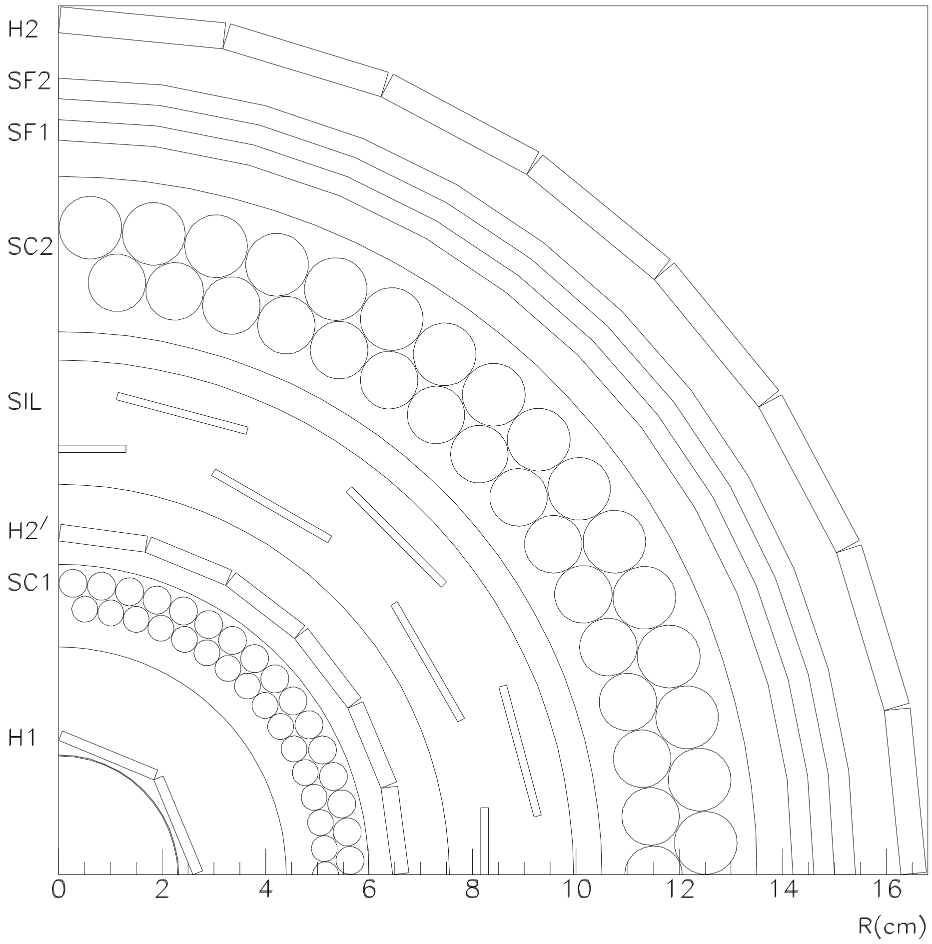

Fig. 2.15: Schematic cross section of the inner detectors: (a) the three hodoscopes (H1, H2′ and H2); (b) the two straw chambers (SC1 and SC2); (c) the two layers of scintillating fibers (SF1 and SF2); (d) the silicon detector (SIL).

Characteristics	Inner Layer	Outer Layer
Average Radius (mm)	144.0	150.6
Pitch (mm)	1.10	1.15
Number of Fibers	430	430

Tab. 2.5: Mechanical characteristics of the scintillating fiber tracker.

addition, the good overall light yield makes it possible to combine the pulse height information and the fine granularity to discriminate between single minimum-ionizing particles and e^+e^- coalescent pairs, which constitute one of the main sources of background (Section 3.4). This last feature has not been implemented, since we already have an efficient and powerful off-line tool to tag single electrons or positrons, ie the Electron-Weight index, described in Section 3.1.(c).

Each scintillating fiber is wound around one of the two support cylinders, on the surface of which a set of U-shaped grooves has been machined. The depth of the grooves varies linearly with the azimuthal coordinate ϕ, so that the fiber overlaps itself after one turn (Figure 2.16). Some of the characteristics of the fibers and of the cylinders are summarized in Table 2.4 and in Table 2.5. On one end, the fibers are aluminized, to increase the light yield and to improve its homogeneity; on the other end, they are thermally spliced to clear fibers, which, after a four-meter path, bring the light to the surface of the Visible Light Photon Counters (VLPC HISTE-V, EOC-low). The complete light path is shown in Figure 2.17.

The VLPCs (Petroff and Atac 1989; Atac 1998) are solid state photodetectors[h] with high quantum efficiency (70% at 550 nm), gain of about 2×10^4,

[h] In the review article by Ruchti (1996), a discussion of the paradigm for scintillating fiber trackers read out with visible-light photon counters can be found.

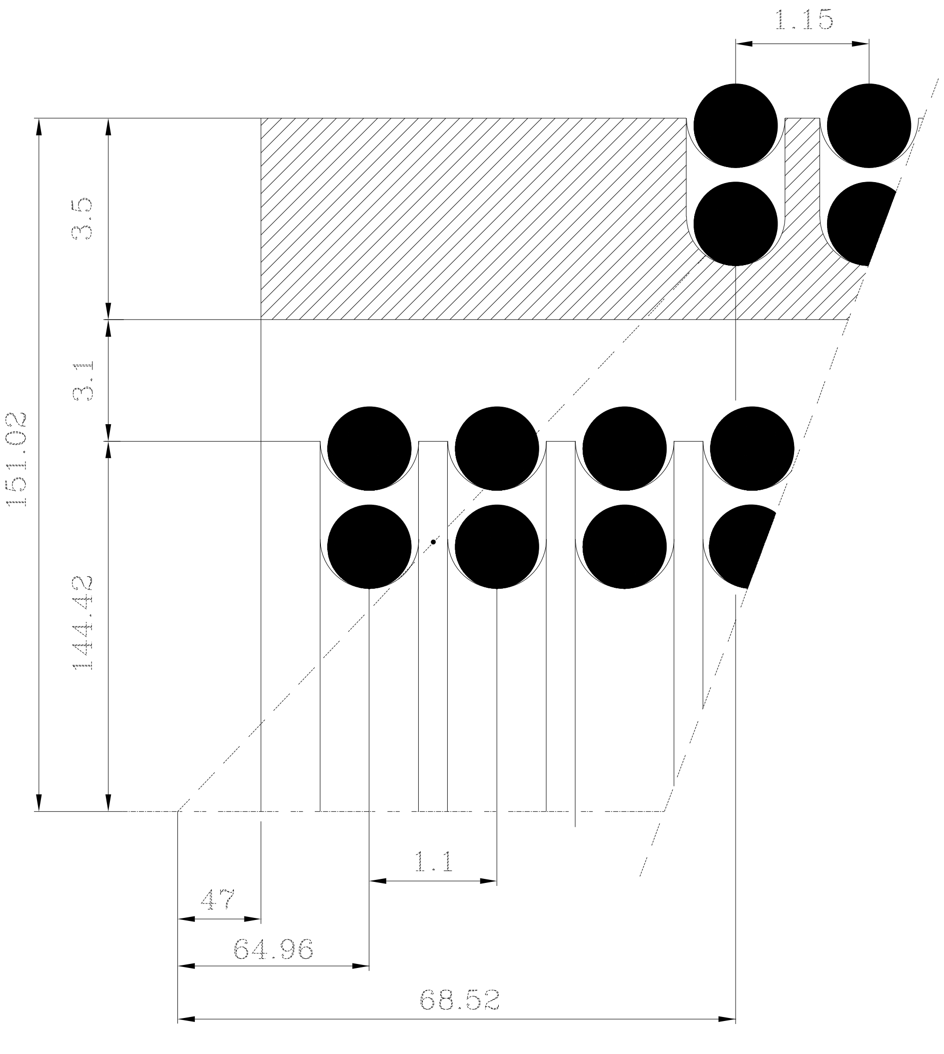

Fig. 2.16: Side view of the two support cylinders of the fiber tracker (dimensions in millimeters, not drawn to scale). Both ends of each scintillating fiber are shown (black circles).

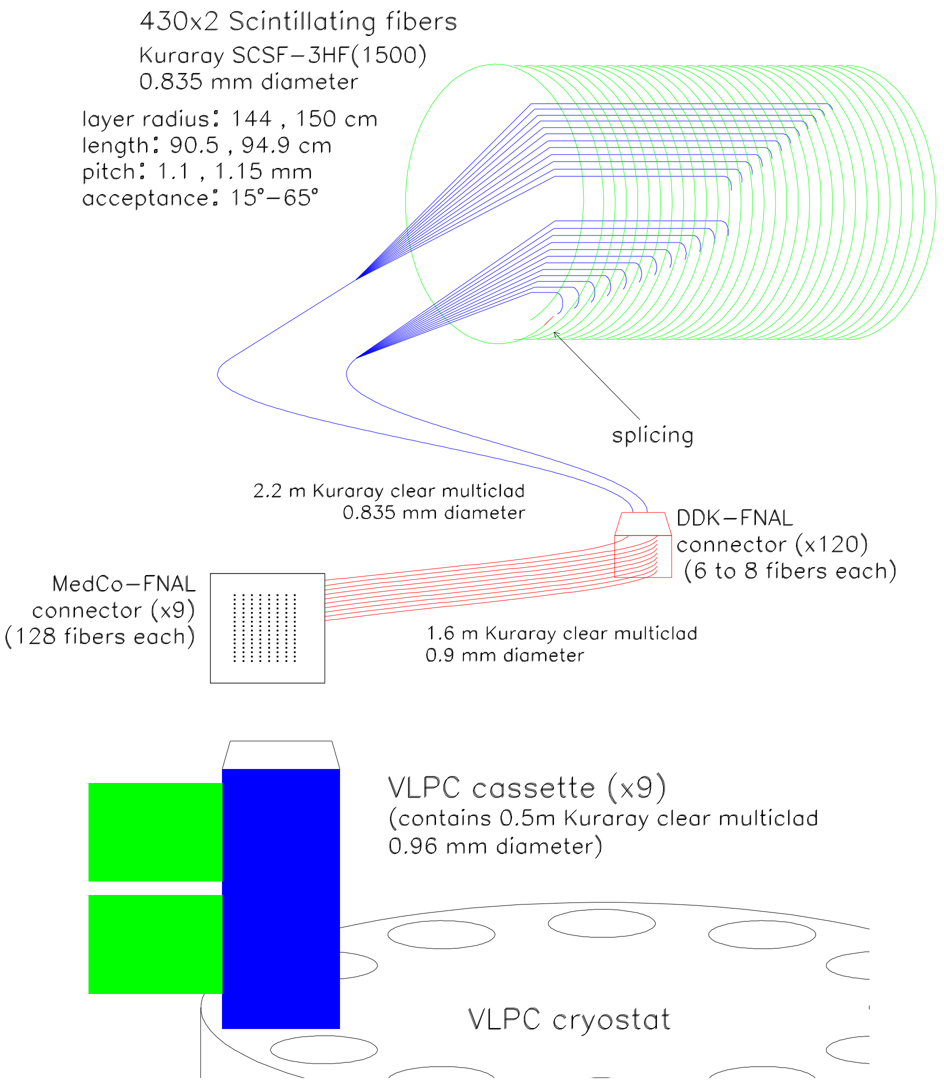

Fig. 2.17: Diagram of the light path from the scintillating fibers to the VLPC cryostat.

single-photon counting capability and resistance to rates up to 10^8 photons/pixel/s. They are housed in a cryostat and operated at a temperature of 6.5 K.

The electronic signal generated by the VLPCs is amplified and sent to discriminator-OR-splitter modules. These modules provide an analog and a digital output for each input channel, together with the digital OR of all inputs. The analog signal is recorded by ADCs, while the digital output is read out by latches. The digital OR of a set ('bundle') of adjacent channels is sent to TDCs and to the first-level trigger logic.

For each channel, we measured the one photoelectron equivalent in ADC counts by illuminating the VLPC pixels with an attenuated LED source. From a high statistics sample ($\approx 10^3$ hits/fiber) of hadronic punch-through tracks in the central calorimeter, we obtained the charge generated by a minimum-ionizing particle. The resulting average number of photoelectrons per mip is about 14 — the high quantum efficiency of the VLPCs compensates for the thinness of the active material.

The detection efficiency and the tracking resolution have been measured with a clean sample of J/ψ-inclusive and ψ' events, where the J/ψ or the ψ' decays into e^+e^-.

In Figure 2.18a, I report the fraction of tracks detected by the tracker, as a function of the polar angle θ for different data samples. The variations over time are due to different running conditions (VLPC bias voltage, ADC gate width, dead channels). The decrease in the upstream region ($\theta > 40°$) is consistent with the diminished geometrical acceptance (due to the constant fiber spacing), evaluated with a Monte Carlo calculation; the average detection efficiency is 99.5%.

The fiber tracker is by far the device with the best θ resolution in the E-

835 apparatus. For this reason, I measured its ‘intrinsic’ resolution, defined as the standard deviation (divided by $\sqrt{2}$) of the distribution of the residuals $\theta_{\mathrm{INN}} - \theta_{\mathrm{OUT}}$, where, for a given track, θ_{INN} (θ_{OUT}) is the polar angle measured with the inner (outer) layer (Figure 2.18b). The intrinsic resolution, averaged over all polar angles, is 0.7 ± 0.1 mrad.

(d) Straw Chambers

Two cylindrical straw chambers (Bagnasco et al. 1998a) provide a measurement of the azimuthal coordinate ϕ for charged tracks.

Each chamber consists of two staggered layers of 64 drift tubes, with their axes parallel to the beam pipe (Figures 2.15 and 2.19). This geometry allows to achieve a relatively low occupancy in each element and to solve the left-right ambiguities on the position of the track with respect to the anode wire. The main characteristics of the two chambers are reported in

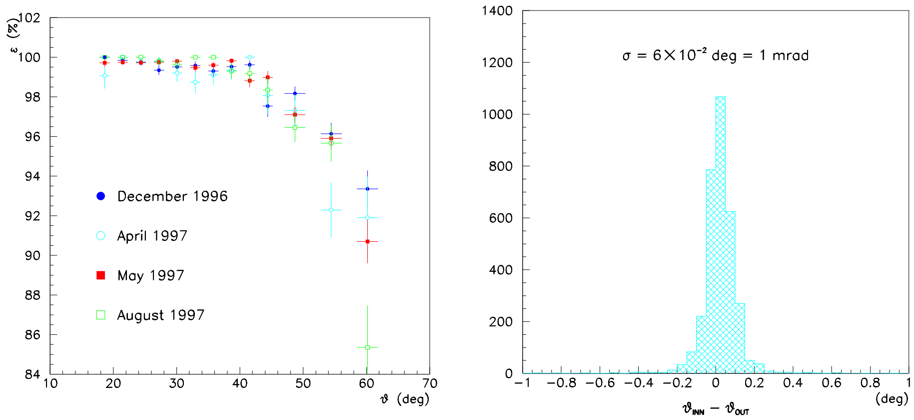

(a) (b)

Fig. 2.18: Detector performance of the scintillating fiber tracker: (a) detection efficiency × geometrical acceptance; (b) distribution of residuals.

Characteristics	Inner Chamber	Outer Chamber
Average Radius (mm)	54	120
Polar Coverage	15°–58°	15°–65°
Diameter of Tubes (mm)	5.0, 5.4	11.1, 12.1
Length of Tubes (mm)	182	414
Operating Voltage (V)	1320	1530
Anode diameter (μm)	20	20

Tab. 2.6: Main characteristics of the straw chambers.

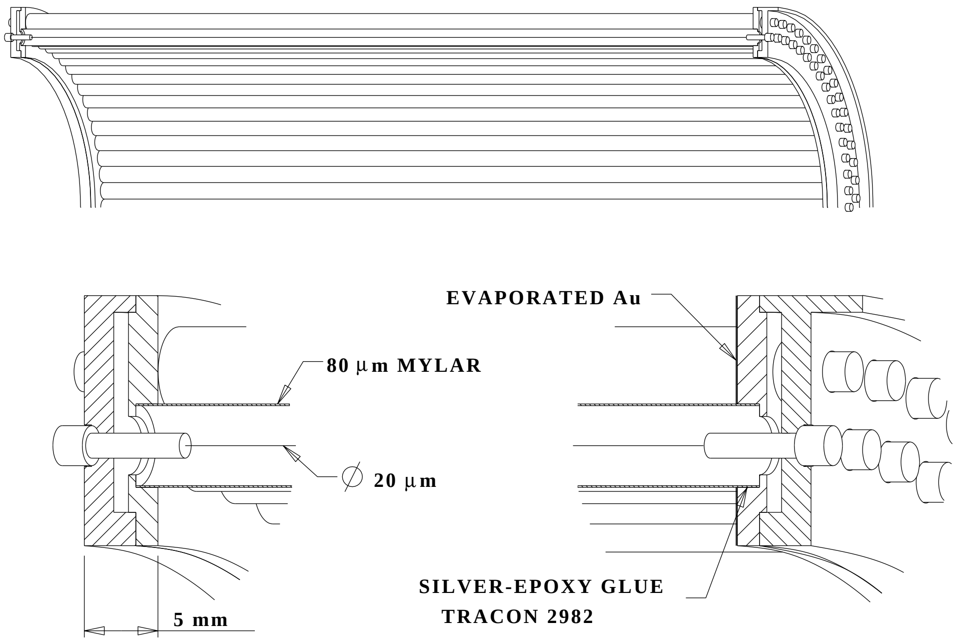

Fig. 2.19: Schematic diagram of the inner straw chamber and a detail of the anode wire holders.

Table 2.6.

The tubes contain a mixture of Ar, C_4H_{10} and $(OCH_3)_2CH_2$, in the proportion 82:15:3 (drift velocity of about 40 μm/ns). This gas is chosen because it shows good detection efficiency at relatively low voltage and because it can cope with the high event rates ($\sim 10^2$ kHz/tube). Each of the 128 channels is read out by an amplifier-shaper-discriminator directly mounted on the downstream end of the detector. The output signals are then sent to a TDC.

The detection efficiency per layer varies between 0.8 (near the walls of the tubes) and 1 (in proximity of the anode wire), as shown in Figure 2.20a. The angular resolution per track is measured with a clean sample of events $\bar{p}p \to J/\psi \to e^+e^-$. It is 9 mrad per track, corresponding to about 250 μm per layer (Figure 2.20b).

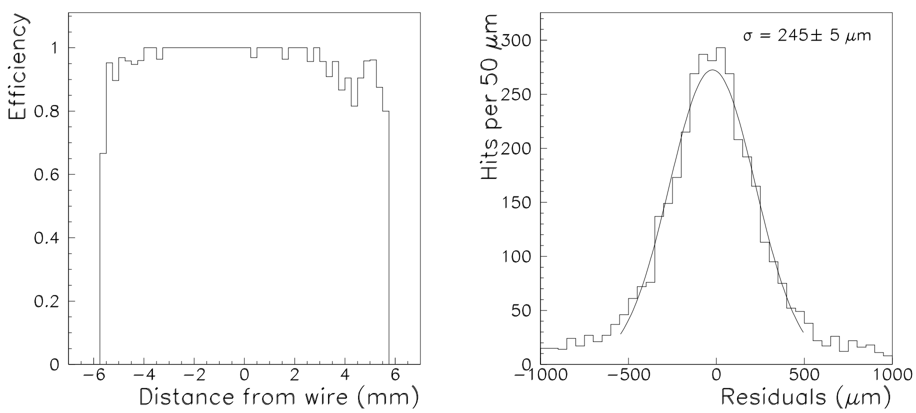

(a) (b)

Fig. 2.20: Performance of the straw chambers: (a) detection efficiency; (b) position resolution.

(e) Silicon Pads

A silicon pad detector (Buzzo et al. 1997) to be used for tracking was built and installed, but never exploited because of the excessive electronic noise. The malfunction occurred right after the beginning of the data taking. The temperature at which the built-in electronics were operated was too high, even though it was within the manufacturer specifications.

(f) Hodoscopes

Three cylindrical plastic scintillator hodoscopes (H1, H2$'$ and H2) are located at increasing distances from the beam axis (Figure 2.15). They are employed in the trigger to select charged tracks. Their pulse heights, together with those in the Čerenkov counter, are used off-line to distinguish single charged particles from electron-positron pairs due to photon conversions or to Dalitz decays of neutral pions.

Hodoscope H1 is positioned right outside the beam pipe. It consists of 8 elements covering the polar angle between 9° and 65°. Each element is 2 mm thick. The 24 elements of hodoscope H2$'$ (scintillator thickness $=$ 3 mm) are located at a radial distance of 6.5 cm. Hodoscope H2 is mounted on the frame of the Čerenkov counter and contains all the other inner detectors. The thickness of its 32 elements is 4 mm.

A fourth hodoscope, the forward veto counter FCH (Figure 2.11), is used in the trigger to reject events with charged tracks in the region not covered by the central detector. It comprises 8 trapezoidal plastic scintillators, which are perpendicular to the beam axis. They cover the full azimuth and the polar region 2°–9°.

All the hodoscope signals are sent to the trigger logic, to an ADC and to a TDC.

(g) Forward Calorimeter

The polar angle region from 2° to 12° is covered by a planar end-cap calorimeter (Hasan et al. 1990), shown in Figure 2.11 and in Figure 2.21. Its purpose is twofold: (a) to increase the acceptance for reactions like $\chi_0 \to J/\psi + \gamma \to (e^+e^-) + \gamma$ or $J/\psi + \pi^0 \to (e^+e^-) + (\gamma\gamma)$; (b) used as a veto, it can reduce the background to events completely contained in the central detector. It is not used in the form factor analysis presented here.

Its 144 modules are arranged according to a 13×13 array (10 cm spacing). There are no modules at the center of the grid (to accomodate the beam pipe) and at the corners, where angular coverage is already ensured by the central calorimeter. Each module consists of 148 alternate layers of lead plates and scintillator tiles, for a total of 14.7 radiation lengths of absorber.

During the shutdown of March 1997, the modules were replaced with

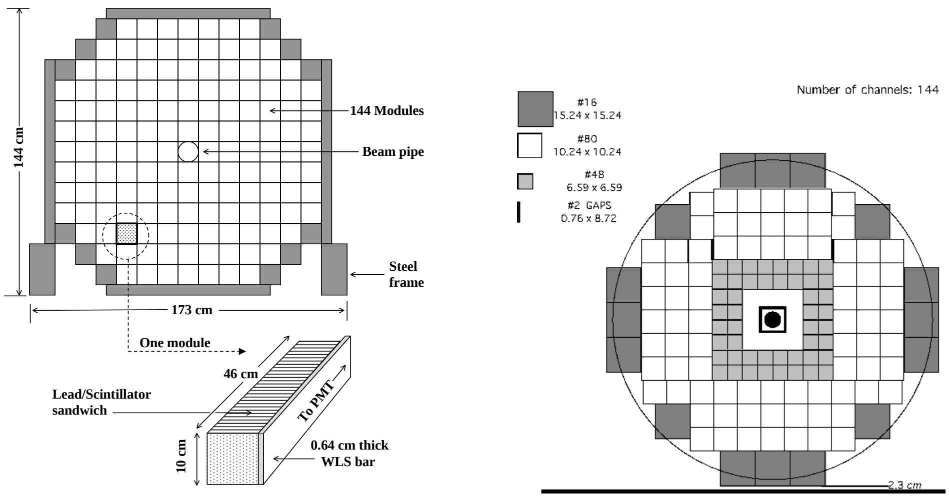

Fig. 2.21: The two end-cap calorimeters used in E-835: on the left, the layout of the scintillator/lead modules; on the right, the lead-glass calorimeter.

lead-glass blocks, in order to obtain a better energy resolution. Since the blocks have different sizes, the layout of the detector was modified (Bagnasco et al. 1997) (Figure 2.21).

The signal from each block is processed by a shaper board and then read out by an ADC and a TDC.

2.4 Data Acquisition

Including all the detector and trigger information (ADCs, TDCs, latches), each event occupies approximately 1 Kbyte, depending upon the data stream (charged or neutral events) and the CM energy. The total trigger rate is typically 1.4 KHz, yielding a rate to tape of the order of Mbytes/s.

E-835 employs the DART data acquisition system[i], which, in this regime, guarantees dead times smaller than 10%. The system performs several operations: event building, on-line filtering, data logging, run control and monitoring. The hardware is based upon the CAMAC/FASTBUS standards, while the software has been developed for SGI Challenge multiprocessor machines.

The data regarding the accelerator, the jet target and the luminosity monitor have their own individual collection streams, separated from the detector/trigger data.

[i] DART (`http://www-dart.fnal.gov`) is a collaboration between the Fermilab Computing Division and some fixed-target experiments.

3. THE DATA ANALYSIS

In this chapter, the complete data analysis is presented, from the raw data to the measurement of the form factor. Given the small cross section of the process under study, one of the main goals is an efficient selection of the events. Especially important is also an evaluation of the background sources; here the main discussion is given, while the details on how some quantities have been measured are given in the appendices.

3.1 Selection of $\bar{p}p \to e^+e^-$ Events

(a) Data Sample

The data taken during E-835 are distributed in the energy region 2.9 GeV $< \sqrt{s} <$ 4.3 GeV. To reduce background contamination, I exclude the data taken in proximity of some resonances, because they are known to yield a comparatively strong e^+e^- or J/ψ-inclusive signal (with the J/ψ decaying into e^+e^-); namely[a] the J/ψ (rest energy m = 3096.88 MeV, full width Γ = 87 keV), the χ_0 (m = 3417 MeV, Γ = 14 MeV), the χ_1 (m = 3510.5 MeV, Γ = 0.9 MeV), the χ_2 (m = 3556.2 MeV, Γ = 2.0 MeV) and the ψ' (m = 3686.00 MeV, Γ = 0.28 MeV). These data are useful for tuning the selection, and for efficiency and background studies. The remaining data ($\approx 10^2$ pb^{-1}) have been grouped in the way indicated in Table 3.1. For each

[a] Masses and widths are taken from the Review of Particle Physics (Caso et al. 1998).

data point, the weighed mean $\sqrt{s}$ and rms, the total integrated luminosity L and the number N of events (selected according to the criteria described in Section 3.1.(c)) are reported. Figure 3.1 shows the distribution of the accumulated luminosity versus the CM energy, emphasizing the samples that I use in the analysis with a horizontal shaded bar.

(b) First-level Trigger and On-line Filter

The trigger logic that selects events for this analysis requires two back-to-back electron tracks and, independently, two calorimeter showers with high invariant mass.

A charged track (h) is defined as a coincidence between an element of hodoscope H1 and one of the four corresponding elements of hodoscope H2 (Figure 3.2), plus two overlap H2 elements. So, for instance, element H1-2 is in coincidence with the logical OR of elements H2-4 to H2-9. If a hit is also recorded in the appropriate cells of the Čerenkov counter, an electron track (e) is defined.

Sample	$\sqrt{s}$ Interval (GeV)	Mean ± Rms (GeV)	L (pb^{-1})	N
1	2.900–3.050	2.9737 ± 0.0269	17.69	93
2	3.200–3.340	3.2840 ± 0.0427	1.78	3
3	3.520–3.540	3.5261 ± 0.0035	47.84	33
4	3.570–3.670	3.6208 ± 0.0241	33.99	14
5	3.710–3.880	3.7889 ± 0.0664	1.86	1
6	4.270–4.310	4.2890 ± 0.0003	0.76	0

Tab. 3.1: Summary of data used for the form factor analysis.

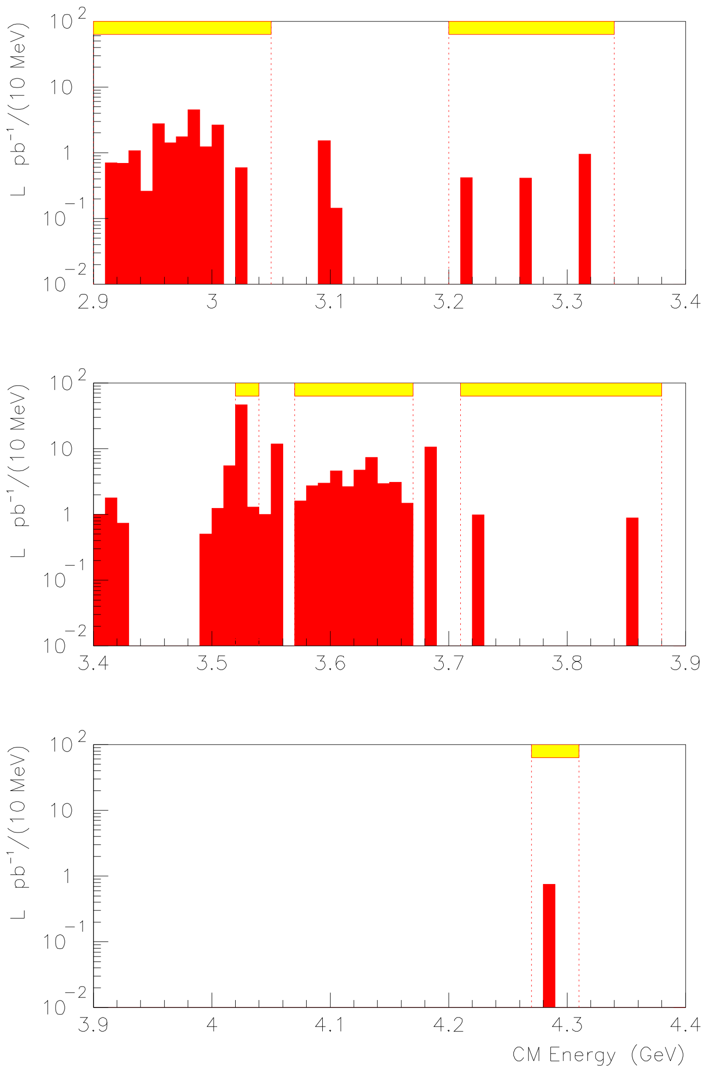

Fig. 3.1: Distribution of the luminosity accumulated during E-835 as a function of CM energy.

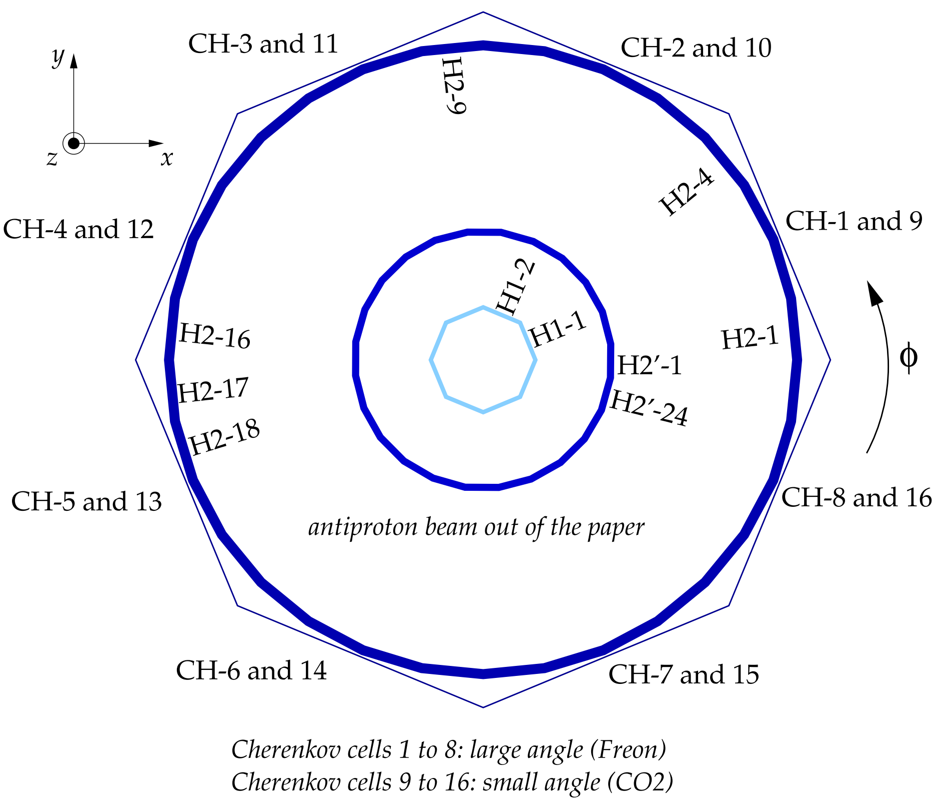

Fig. 3.2: Schematic diagram of the counters employed in the trigger.

The charged coplanarity logic (COPL) is formed by the elements of hodoscope H2 and selects tracks that are back-to-back in ϕ. It is the coincidence between an H2 element and at least one of the three opposite in azimuth. For example, elements H2-1 with the logical OR of elements H2-16, H2-17 and H2-18.

The central calorimeter is used to tag events with two back-to-back large energy deposits, separated by at least 90° in azimuth (PBG3 logic). The signals from the 1280 lead glass blocks first go through the Level I Summers, where, for each ring[b], the signals of nine consecutive blocks are summed (Figure 3.3). The first and last block in the sum are overlap blocks, ie they are counted in two adjacent sets of nine blocks. For instance, in ring 1, the signals from blocks 1 to 9 are summed, as are 9 to 17, etc.; finally, blocks 57 to 64 back to (and including) block 1. Thus, 160 signals leave the Level I Summers, eight from each ring. These signals are then split; one set forms the strobe for the logic units (Memory Look-up Units, or MLUs), and the other set enters the Level II Summers.

At the Level II Summers, the signal from each octant of blocks is summed with the same octant in five (or four) other adjacent rings. For example, octant 1 (ie wedges 1 to 9) from rings 1 to 4 are summed, as are the ones from rings 4 to 8, etc.; finally, from rings 16 to 20. It should be noticed that the first sum is made from only four rings, and that there is again an overlap (of rings this time). The 40 signals that leave the Level II Summers are the signals of the 40 so-called "super-blocks" of the central calorimeter.

After Level II, the 40 signals are split. One set goes to ADCs and the other set goes to an integrator. After the integrator, the signals enter a

[b] The definitions and pictures of the 20 rings and of the 64 wedges are in Section 2.3.(a).

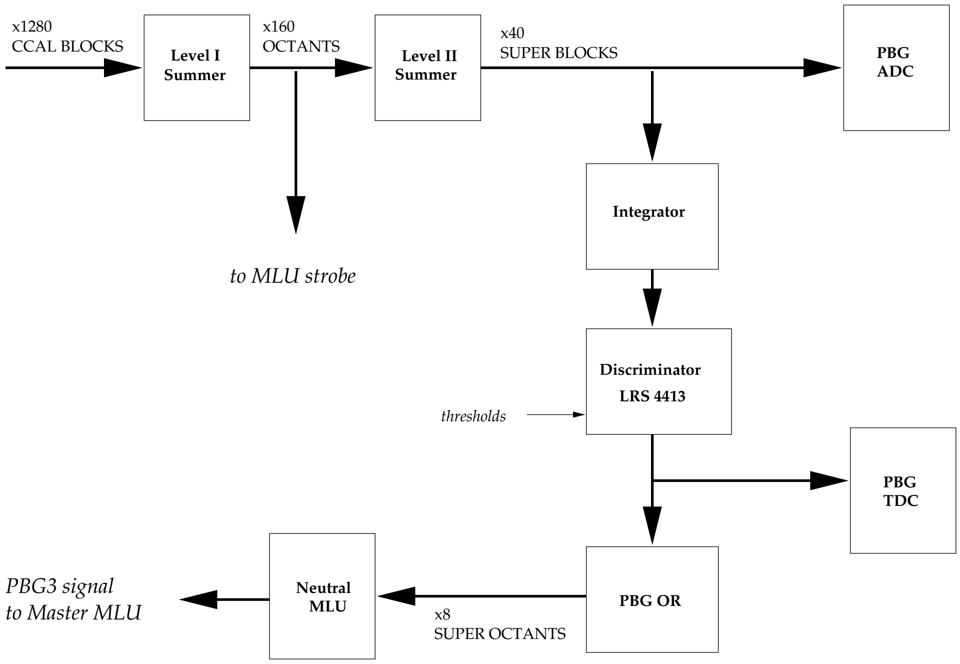

Fig. 3.3: The two-body branch of the CCAL trigger logic, from the individual blocks to the final PBG3 signal.

discriminator, whose thresholds are set according to two-body reactions ($\bar{p}p \to \gamma\gamma$ below the J/ψ formation energy, $\bar{p}p \to J/\psi(\to e^+e^-) + X$ above); therefore, they depend on the CM energy at which the data is taken.

The 40 super-block signals are split again after the discriminator; one set going to TDCs and the other set going to the PBG OR module. This module performs the logical OR of the five super-blocks in the same octant. Its 8 outputs are fed into the Neutral MLU, which looks for coincidences between one of the eight octants and the three opposite to it in azimuth (for instance octant 1 and at least one among octants 4, 5 and 6). The resulting logic signal is called PBG3, which stands for "lead glass, one versus three".

The final e^+e^- trigger is formed by three branches. The first one is the main logic; the other two are used to check the efficiency of the Čerenkov counter and of PBG3 logic. In symbols:

$$\begin{aligned}(e^+e^-) \quad = \quad & (2e)\cdot(\mathrm{H2} \leq 4)\cdot(\mathrm{PBG3}) & + \\ & (1e)\cdot(2h)\cdot(\mathrm{H2} = 2)\cdot(\mathrm{COPL})\cdot(\mathrm{PBG3}) & + \\ & (2e)\cdot(\mathrm{H2} = 2)\cdot(\mathrm{COPL})\cdot(\overline{\mathrm{FCH}}). &\end{aligned} \tag{3.1}$$

The symbols $(\mathrm{H2} = 2)$ and $(\mathrm{H2} \leq 4)$ refer to the multiplicity (ie number of hits) in hodoscope H2, while $\overline{\mathrm{FCH}}$ represents the veto on the forward hodoscope.

Events which satisfy the hardware trigger are processed by the on-line filter[c], which requires the event to contain at least one pair of CCAL clusters forming an invariant mass greater than 2.2 GeV (2.0 GeV when taking data below the transition energy of the accumulator).

[c] The filter is called PRUDE, which stands for Program Rejecting Unwanted Data Events.

(c) Data Reduction and Off-line Selection

Electron tracks are reconstructed off-line by associating the hits in the counters (hodoscopes and Čerenkov detector) with the calorimeter showers. Track information from the inner detectors is added to improve the angular resolution. The two electron candidates are identified as the tracks with the highest invariant mass.

The off-line selection of $\overline{p}p \to e^+e^-$ events is based upon two straightforward criteria: identification of the electron and of the positron and kinematic characteristics of the event. In the following paragraphs, I describe in detail the cuts that I impose on electron identification, on CCAL cluster multiplicity, on kinematic fit probability and on fiducial volume.

Fiducial volume. The cut in fiducial volume is necessary in order to remove inhomogeneities in the response of the detector at its edges. For this reason I accept only events in which both electron candidates have polar angles in the interval $15° < \theta < 60°$, well within the angular coverage of the central detector.

Electron identification. What characterizes electrons and positrons in the E-835 detector is pulse height in the Čerenkov counter, energy loss in the hodoscopes and profile of the electromagnetic shower. For each candidate electron track, an electron weight index (EW) is constructed using the pulse heights in the counters and the shape of the electromagnetic shower (Patrignani 1997). The particles that we wish to reject are mostly coalescing e^+e^- pairs (from photon conversions or Dalitz decays of neutral pions), coalescing photons from π^0 decays and hadrons. Following is the complete list of the variables used. The pulse heights in the counters

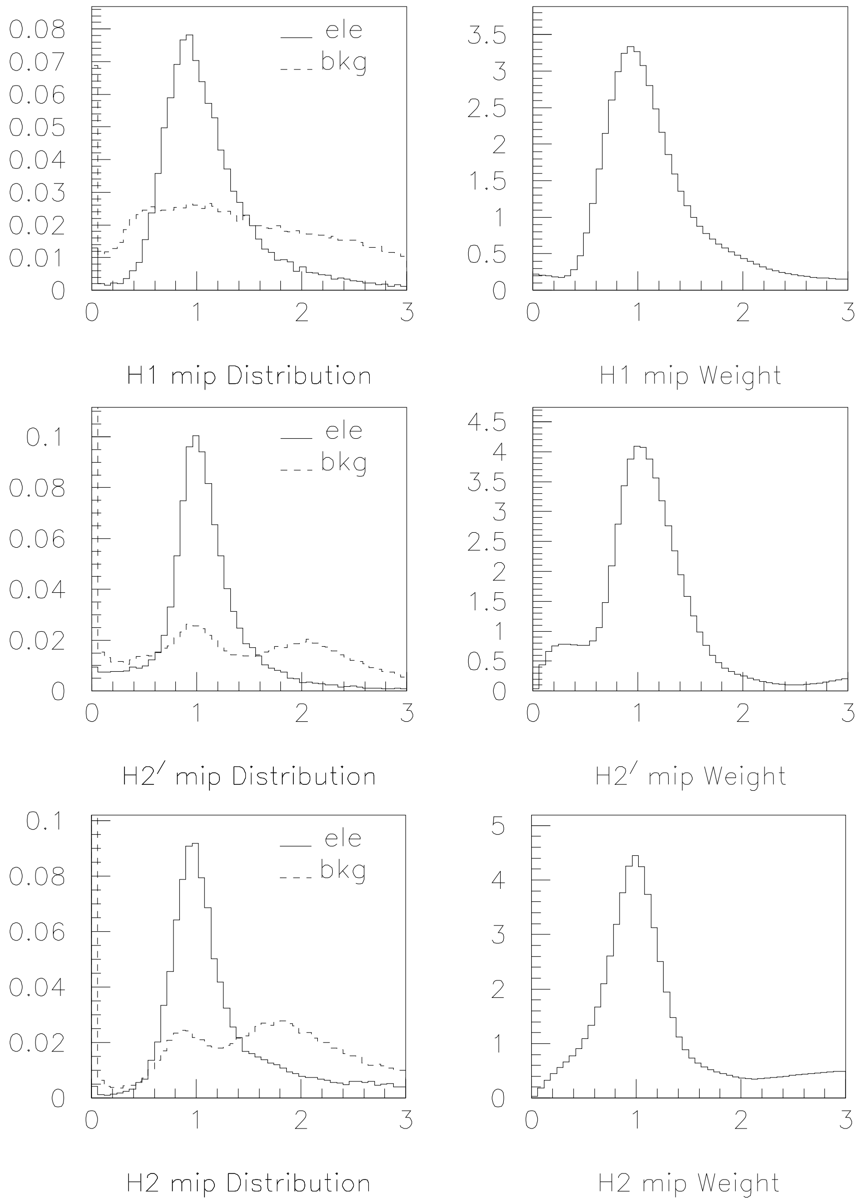

Fig. 3.4: Electron-Weight distributions for the three hodoscopes.

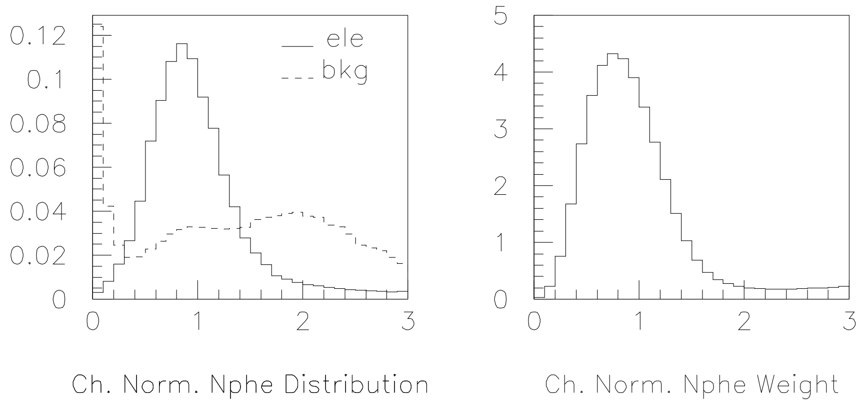

Fig. 3.5: Electron-Weight distributions for the Čerenkov counter.

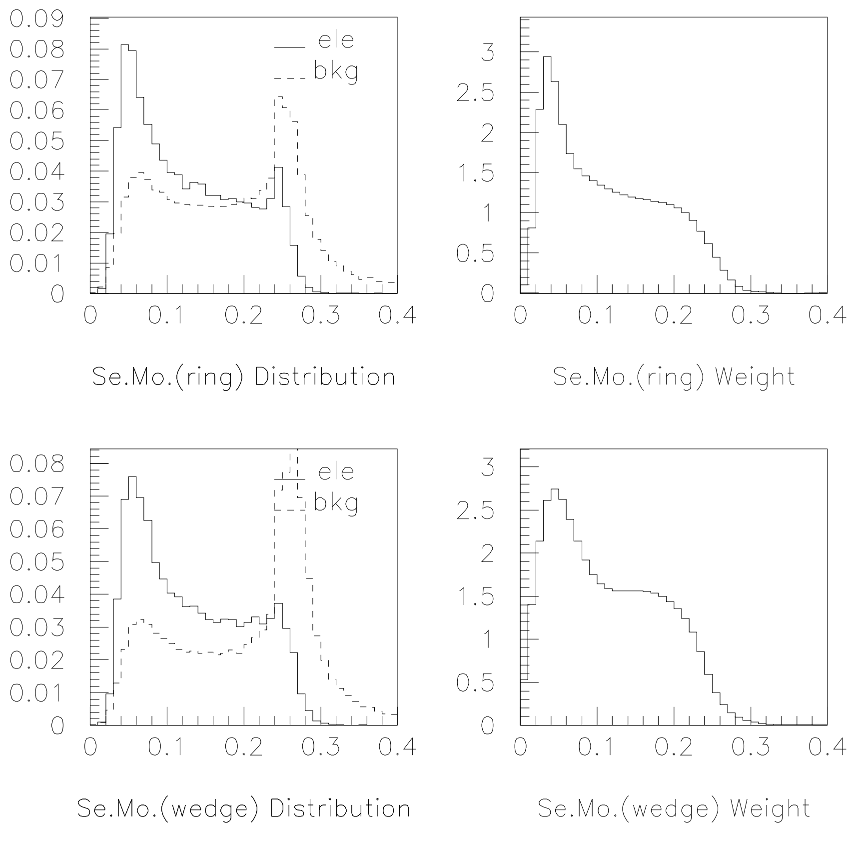

Fig. 3.6: Electron-Weight distributions of CCAL second moments.

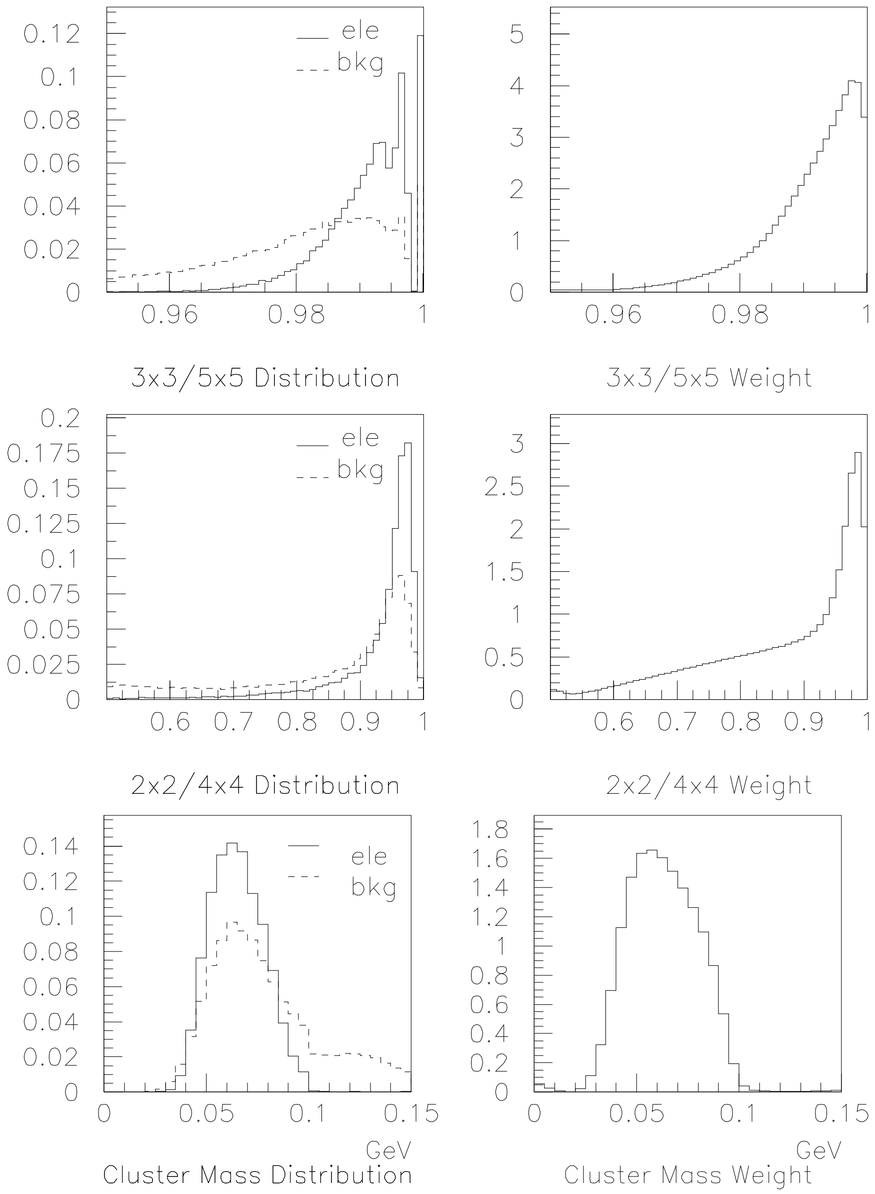

Fig. 3.7: Electron-Weight distributions of CCAL fractional shower energy and cluster mass.

are aimed at discriminating between singly charged tracks and coalescing e^+e^- pairs:

- pulse height p_1 in hodoscope H1 (in mips, ie normalized to the signal generated by a minimum-ionizing particle);
- pulse height p_2 in hodoscope H2 (in mips);
- pulse height p_p in hodoscope H2′ (in mips);
- pulse height p_C in the Čerenkov counter (normalized number of photoelectrons);

coalescing e^+e^- or $\gamma\gamma$ pairs generate in the CCAL a wider electromagnetic shower, compared to single electrons, positrons or photons. Moreover, the distribution of the energy deposits in the blocks can have two local maxima. Most of the times, hadrons release a small amount of energy (≈ 450 MeV) in only one block (punch-through tracks); if a nuclear interaction takes place which generates neutral pions in the final state, an electromagnetic shower is inititated, but it is usually asymmetric. The following parameters are used to characterize the energy deposits in the calorimeter:

- second moments of the energy distribution $E(r, w)$ in the CCAL cluster, within a 3×3 grid around the highest-energy block (r_0, w_0), expressed in ring (r) and wedge (w) units:

$$
\begin{aligned}
s_r &\equiv \sum_{(r,w)\in 3\times 3} E(r,w)\cdot(r-r_0)^2 \Bigg/ \sum_{(r,w)\in 3\times 3} E(r,w) \\
s_w &\equiv \sum_{(r,w)\in 3\times 3} E(r,w)\cdot(w-w_0)^2 \Bigg/ \sum_{(r,w)\in 3\times 3} E(r,w);
\end{aligned}
$$

- fractional shower energy in a 3×3 block region surrounding the highest energy block, with respect to a 5×5 grid; same thing for a

2×2 grid (defined by the highest energy block and by the largest deposit among the eight adjacent to it) with respect to the 4×4 region enclosing it:

$$R_{3/5} \equiv \sum_{(r,w)\in 3\times 3} E(r,w) \Big/ \sum_{(r,w)\in 5\times 5} E(r,w)$$
$$R_{2/4} \equiv \sum_{(r,w)\in 2\times 2} E(r,w) \Big/ \sum_{(r,w)\in 4\times 4} E(r,w)$$

- cluster mass, constructed from the energy deposits in the blocks within a 5×5 grid centered around the highest energy hit; it is defined as follows:

$$M_c \equiv \left[\left(\sum_{(r,w)\in 5\times 5} E(r,w) \right)^2 - \left(\sum_{(r,w)\in 5\times 5} E(r,w) \cdot \hat{x}(r,w) \right)^2 \right]^{1/2}, \tag{3.2}$$

where $\hat{x}(r,w)$ is the unit vector from the interaction point to the center of the counter (r,w).

The distribution $f_i(x_i)$ $(x_i = p_1, p_2, \ldots, M_c)$ of each of the nine variables listed above is observed in a clean sample of electron and positron tracks ($J/\psi \to e^+e^-$, $\chi_{c1,2} \to J/\psi(\to e^+e^-) + \gamma$ and $\psi' \to J/\psi(\to e^+e^-) + X$, selected with a kinematic fit) and in a background sample (data taken off-resonance at various energies). The corresponding normalized distributions are called $f_i^{ele}(x_i)$ and $f_i^{bkg}(x_i)$, respectively; they are shown on the left side of Figures 3.4–3.7. On the right side of the same figures, the ratio ('weight'):

$$W_i = \frac{f_i^{ele}(x_i)}{f_i^{bkg}(x_i)} \tag{3.3}$$

is plotted for each of the nine chosen quantities.

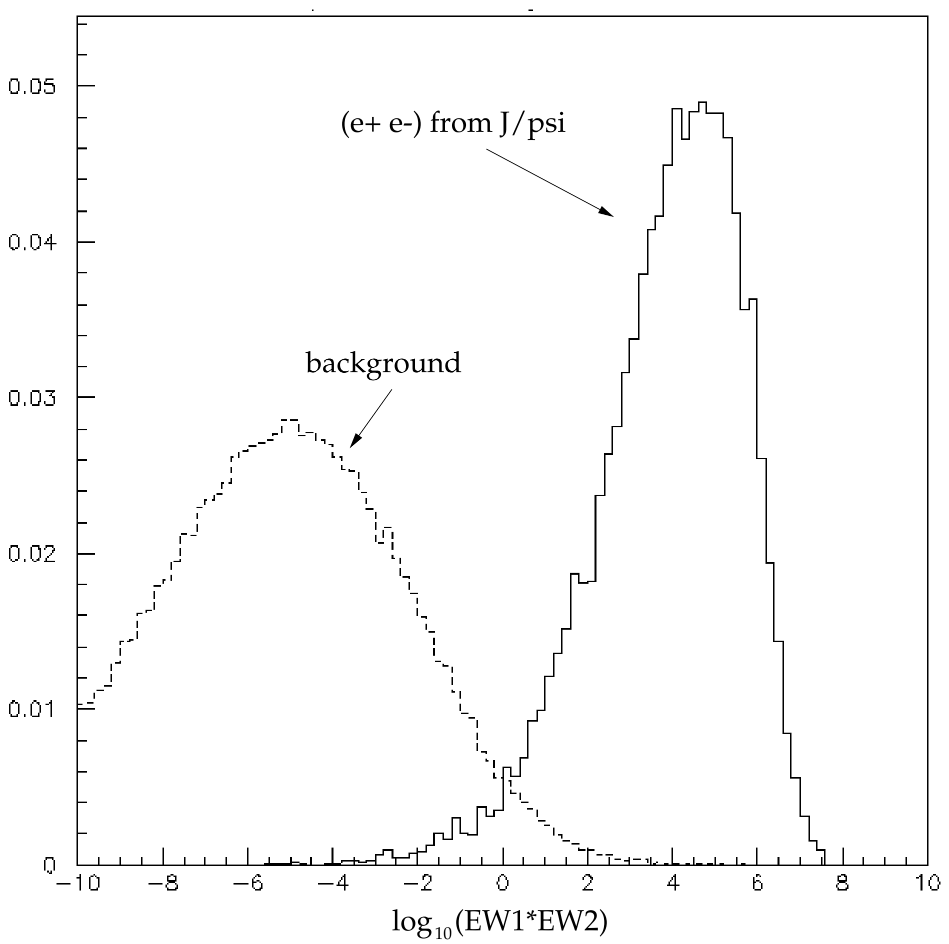

Fig. 3.8: Distribution of EW indices' product for electrons and background.

For a track with a particular set of values $x_1, \ldots, x_9$ of the above mentioned variables, the EW index is defined as:

$$\mathrm{EW} \equiv \prod_i W_i \tag{3.4}$$

Since in a good event both candidates have to be good electron tracks, a sensible variable to use is the product of the EW indices of the two candidate electrons. The distribution of $\log_{10}(\mathrm{EW1} \cdot \mathrm{EW2})$ in the electron and in the background samples is shown in Figure 3.8.

In order to reduce the size of the data sample, a preliminary selection is applied to the raw data by imposing a loose cut on the product of the EW indices for the two electron candidates: $\log_{10}(\mathrm{EW1} \cdot \mathrm{EW2}) > -1$. Only events which pass this preliminary selection undergo the subsequent analysis. In the final selection, I cut at $\log_{10}(\mathrm{EW1} \cdot \mathrm{EW2}) > 0$.

CCAL multiplicity. The simplest requirement on the number of clusters in the calorimeter would be exactly two on-time clusters. The definition of 'on-time' is tuned on a clean $J/\psi \to e^+e^-$ sample. Figure 3.9a shows the time distribution of the clusters associated with clean electrons and positrons. The horizontal scale has an arbitrary software offset. The time of a cluster is defined as the TDC reading of the highest energy block. In Figure 3.9b, I plot the fraction of electron or positron tracks with cluster times within a window of half-width Δt centered around the mean value $\langle t \rangle$, as a function of Δt. In this analysis, extra clusters whose times differ from the average electron or positron time by less than 7 ns are classified as 'on-time'.

An electron or positron, by interacting with the detector material, can radiate a Bremsstrahlung photon, which might form a distinct satellite cluster in the CCAL. The thicker devices on the particles' path are the beam pipe and the silicon pads; the effect is of the order of a few percent.

To avoid rejecting these events, I do not impose a strict cut demanding exactly two on-time clusters. Events with more on-time clusters are kept, provided that the extra clusters, when paired with either electron candidate, give an invariant mass below 100 MeV. This value has been tuned on a J/ψ sample selected with a tight Electron-Weight cut (Figure 3.10a). In Figure 3.10b, the electron/extra-cluster invariant mass distribution is shown for background events; the π^0 peak is prominent.

Any number of out-of-time or undetermined clusters is allowed. The invariant mass formed by the candidate electron and by the possible out-of-time or undetermined clusters is checked (to make sure that there is no π^0 contamination), but not cuts are necessary.

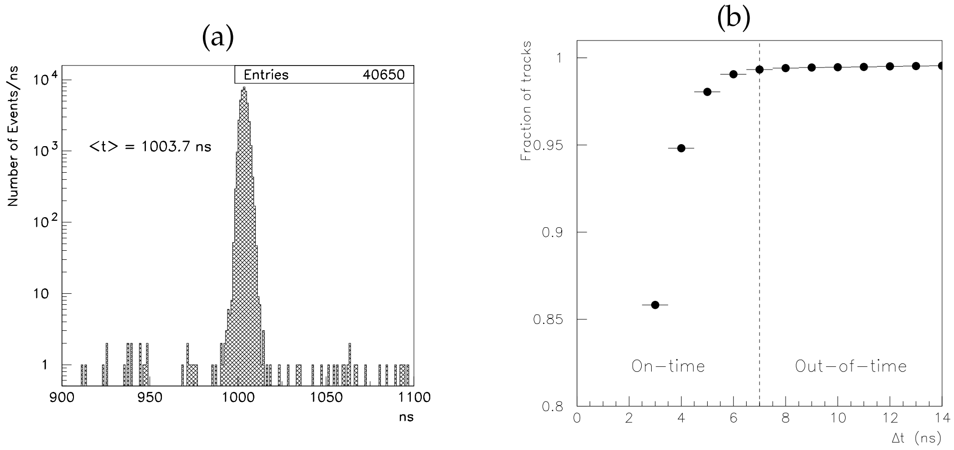

Fig. 3.9: (a) Time distribution of clean electron and positron tracks from $J/\psi \rightarrow e^+e^-$. The horizontal scale has an arbitrary software offset. (b) Fraction of tracks from Figure (a) within a window centered around the mean, as a function of the window's half-width. The vertical dashed line marks the chosen definition of 'on-time' for extra clusters.

Kinematic fit. The goodness of the two-body hypothesis is tested by means of a four-constraint kinematic fit. All candidate events are tested with this hypothesis and are accepted if the fit probability is above 1%. In Figure 3.11 is the fit probability distribution for e^+e^- decays of the J/ψ selected by means of the Electron-Weight ($\log_{10}(EW1 \cdot EW2) > 1$), the CCAL multiplicity (allowing low invariant mass satellite clusters) and the fiducial volume cuts.

The number N of events that satisfy all the criteria described so far is reported in Table 3.1 for each energy region.

3.2 Estimate of Selection Efficiencies

The overall efficiency ε is the product of the trigger efficiency ε_{tri}, the efficiency of the preliminary selection ε_{pre} and that of the off-line analysis

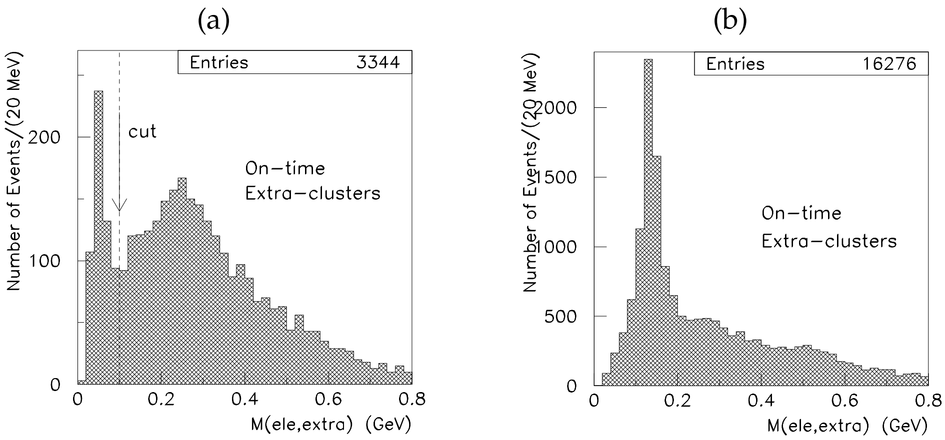

Fig. 3.10: Distribution of the invariant mass formed by all on-time extra clusters when paired with the closest candidate electron: (a) at the J/ψ energy (after imposing a tight cut on the EW index) and (b) at $\sqrt{s}$ = 3.0 GeV (no cuts besides the preliminary selection).

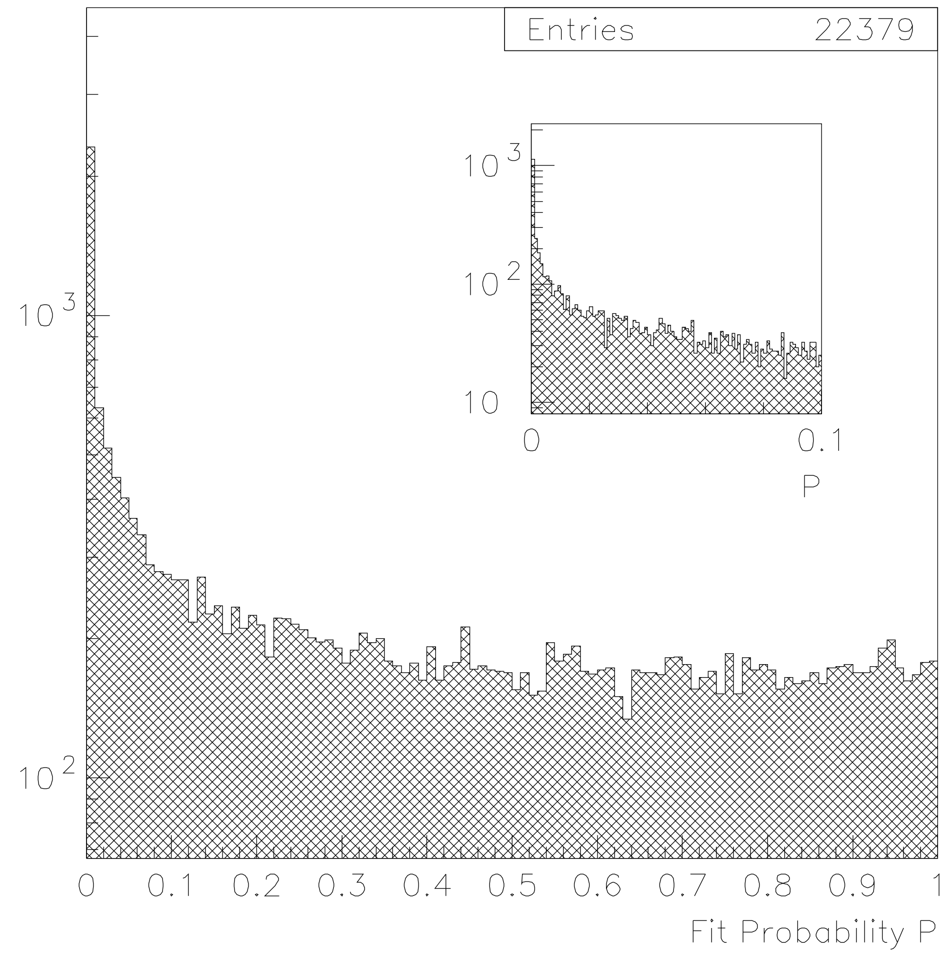

Fig. 3.11: Probability distribution of the kinematic fit for clean $J/\psi \to e^+e^-$. In the inset is a blow-up of a portion of the horizontal scale (the binning is ten times finer).

ε_{ana}:

$$\varepsilon = \varepsilon_{tri} \cdot \varepsilon_{pre} \cdot \varepsilon_{ana}.$$

The inefficiency of the on-line filter is negligible.

The trigger efficiency ε_{tri} takes into account the detection efficiency of the detectors involved in the formation of the logic signals and the efficiency of the logic itself. It has been measured at the J/ψ energy with a special trigger run, since all three branches of the normal trigger require two tracks (Equation 3.1). The special trigger required only one electron track in the H1, H2 and Čerenkov counters (1e), in addition to PBG3, the two-cluster requirement in the central calorimeter. The result is ε_{tri} = 0.898±0.005(stat) (Baldini and Marchetto 1997).. The efficiency of the PBG3 logic can be checked on every run, because the third branch of the e^+e^- trigger does not require it (Equation 3.1). Its inefficiency turns out to be negligible.

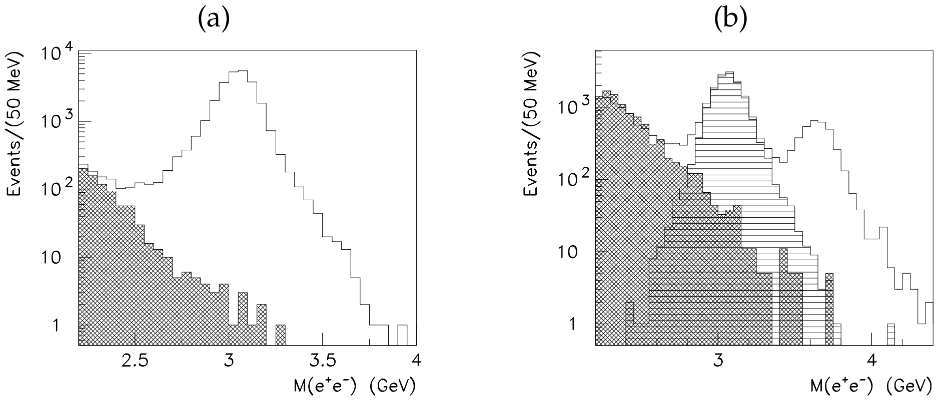

Fig. 3.12: Invariant mass distribution for candidate electrons after preliminary cuts only: (a) at the J/ψ formation energy (white) and at $\sqrt{s}$ = 3.3 GeV (cross-hatched); (b) at the ψ' formation energy (white, all events; horizontal lines, J/ψ-inclusive subsample) and at $\sqrt{s}$ = 3.8 GeV (cross-hatched).

The efficiency of the preliminary off-line cut $\log_{10}(\mathrm{EW1} \cdot \mathrm{EW2}) > -1$ has been measured using clean samples of $J/\psi \to e^+e^-$, $\chi_{c1,2} \to e^+e^-\gamma$ and $\psi' \to e^+e^-$ events (Patrignani 1998). It has been found to be ε_{pre} = $0.985 \pm 0.001(\mathrm{stat})\,^{+0.007}_{-0.020}(\mathrm{syst})$. The systematic error arises from the different processes and CM energies, and represents the maximum deviations observed from the average value.

I evaluated the efficiency of the second set of off-line cuts (the final selection) on both $J/\psi \to e^+e^-$ and $\psi' \to e^+e^-$ events, so as to be sensitive to possible energy-dependent systematic uncertainties. Also, the J/ψ and ψ' data samples have been broken down into four subsamples (runs 533–909, 1006–1432, 2003–2460 and 3005–3346), in order to check the stability of the efficiency over time and for different running conditions. The four subsamples correspond to data taken in Oct–Dec 1996, Jan–Mar 1997, Apr–Jul 1997 and Jul–Sep 1997, respectively.

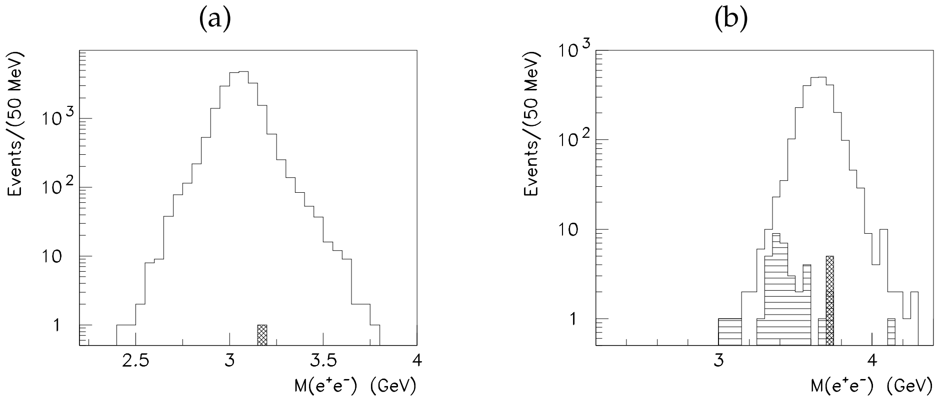

Fig. 3.13: Invariant mass distribution for candidate electrons after the complete selection: (a) at the J/ψ formation energy (white) and at $\sqrt{s}$ = 3.3 GeV (cross-hatched); (b) at the ψ' formation energy (white, all events; horizontal lines, J/ψ-inclusive subsample) and at $\sqrt{s}$ = 3.8 GeV (cross-hatched).

Sample	J/ψ Energy		ψ' Energy	
	Bkg @ 3.0 GeV	Bkg @ 3.3 GeV	Bkg @ 3.6 GeV	Bkg @ 3.8 GeV
1	0.780±0.004	0.789±0.004	0.72±0.01	0.72±0.01
2	0.789±0.005	0.806±0.005	0.75±0.02	0.75±0.02
3	0.728±0.006	0.737±0.005	0.77±0.01	0.77±0.01
4	0.786±0.009	0.801±0.009	0.77±0.02	0.77±0.02

Tab. 3.2: Efficiency of the off-line analysis calculated on different samples. The errors are statistical.

Figure 3.12 shows the invariant mass distribution for candidate electrons after preliminary cuts only: (a) at the J/ψ and (b) at the ψ' formation energies. The cross-hatched areas in both histograms show the background contamination in these samples, calculated by applying the same preliminary cuts to data taken off-resonance and rescaled by luminosity. In Figure 3.12b, inclusive $J/\psi + X$ events coming from the decay $\psi' \to J/\psi + X$ are also shown (horizontal lines). They are selected by means of a 1C kinematic fit on events with an identified e^+e^- pair in the final state ($\log_{10}(EW1 \cdot EW2) > 0$), requiring that the fit probability be higher than 1%, with the additional requirement that the fit probability for the hypothesis $\psi' \to e^+e^-$ be less than 10%.

Figure 3.13 shows the corresponding distributions after the complete event selection. It can be seen that the background contamination in these data samples is very low.

The efficiency of the off-line analysis is defined as the fraction of events in the preliminary samples (Figure 3.12) that survive all cuts (Figure 3.13), once background (including $J/\psi + X$ events at the ψ') is subtracted. At the ψ', only events with invariant mass above 3.4 GeV are considered.

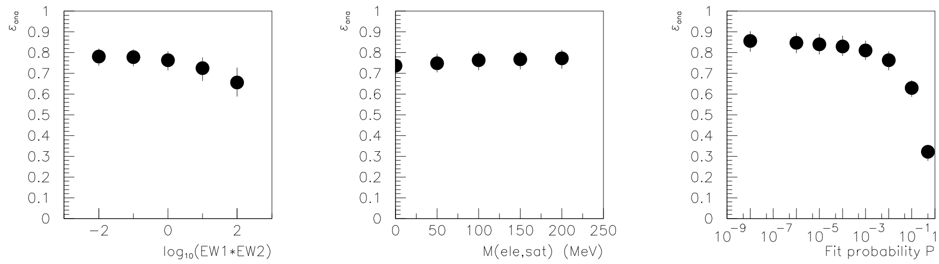

Fig. 3.14: Efficiency of the off-line selection as a function of each cut.

To estimate the systematic uncertainty introduced by the subtraction procedure, I employ background data taken both below and above resonance ($\sqrt{s} = 3.0$ GeV and $\sqrt{s} = 3.3$ GeV for the J/ψ, and $\sqrt{s} = 3.6$ GeV and $\sqrt{s} = 3.8$ GeV for the ψ').

The efficiency is found to be $\varepsilon_{\text{ana}} = 0.764 \pm 0.003(\text{stat})\ ^{+0.042}_{-0.048}(\text{syst})$. Its value is the average of the sixteen efficiencies calculated with the same procedure on the various samples (Table 3.2): J/ψ or ψ' signal from one of the four sets of runs, subtracted background taken below or above resonance. The asymmetric systematic errors are the difference between the average and the largest and smallest values. The individual contributions are approximately 3% from CM energy and 1% from the choice of background; the rest comes from the choice of run numbers.

The overall efficiency, which I use to correct the number of events at all energies, is thus $\varepsilon = 0.676 \pm 0.005(\text{stat})\ ^{+0.042}_{-0.055}(\text{syst})$.

3.3 Stability of the Selection Criteria

The purpose of this study is to verify that the cuts chosen for the event selection, which are described in Section 3.1.(c), are optimized in terms of efficiency and background rejection.

Using the procedure described above in Section 3.2, I calculate the efficiency ε_{ana} of the off-line selection as a function of the three cuts employed: the product of the Electron-Weight indices, the maximum invariant mass allowed when combining a possible on-time extra clusters with the candidate electron or positron and the probability of the two-body kinematic fit (the presence of the fiducial volume cut is understood). While two of them are set to their chosen values, the third is allowed to vary between a 'loose' and a 'tight' value (arbitrarily defined). For instance, for the extra cluster invariant mass, the loose cut is 200 MeV/c^2, above the π^0 mass; whereas the tight cut is 0 MeV/c^2, which is equivalent to requiring no on-time extra clusters. The results are shown in Figure 3.14.

Also the number N of selected events is measured as a function of the three cuts. Figures 3.15, 3.16 and 3.17 show the results for the three samples where they are statistically more significant (samples 1, 3 and 4 in Table 3.1).

The ratio N/ε_{ana} as a function of the cuts indicates whether the sample is being contaminated by background and whether the efficiency of the

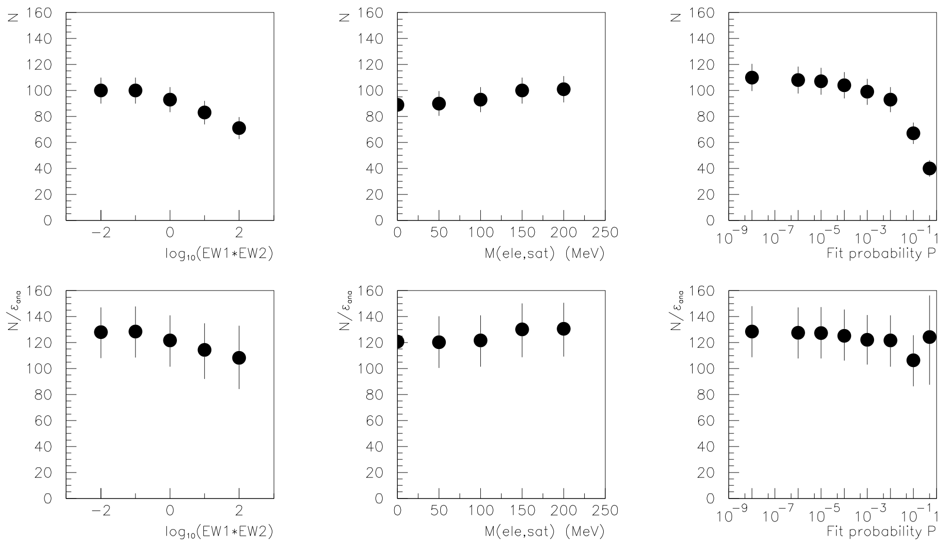

Fig. 3.15: The number of events N selected from sample 1 ($\sqrt{s}$ = 3.0 GeV) and the ratio N/ε_{ana} as a function of the off-line cuts.

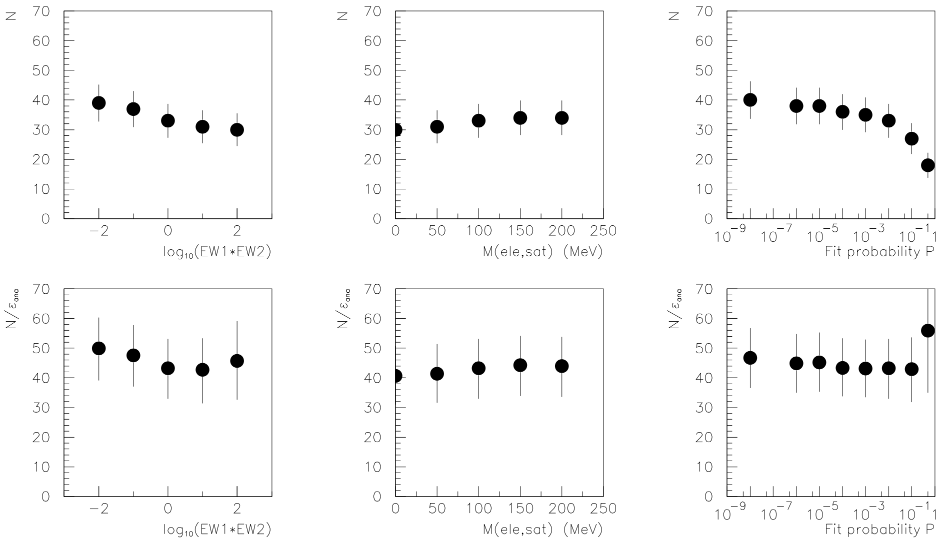

Fig. 3.16: The number of events N selected from sample 3 ($\sqrt{s}$ = 3.53 GeV) and the ratio N/ε_{ana} as a function of the off-line cuts.

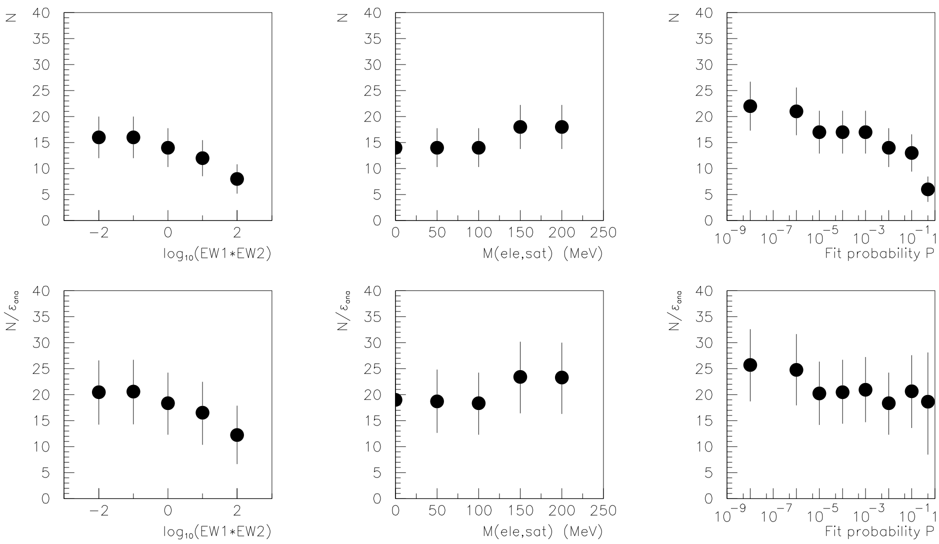

Fig. 3.17: The number of events N selected from sample 4 ($\sqrt{s}$ = 3.6 GeV) and the ratio N/ε_{ana} as a function of the off-line cuts.

selection is optimized. In the absence of background, N/ε_{ana} is expected to be flat.

I consider the plots in Figures 3.15–3.17 satisfactory. The ratio N/ε_{ana} is stable in proximity of the chosen cuts, and the selection criteria have both high efficiency and good background-rejection power.

3.4 Study of Background Processes

Since the e^+e^- signal is immersed in the comparatively huge $\bar{p}p$ total cross section, a thorough evaluation of the magnitude of background contamination is necessary. The reactions that can simulate a good signal in the E-835 detector are photon conversions, π^0 Dalitz decays, two-body hadronic final states (mainly $\pi^+\pi^-$) and inclusive production of J/ψ.

(a) Photon Conversions and Dalitz Decays

I consider the reactions:

$$\bar{p}p \rightarrow \pi^0\pi^0 \quad (3.5)$$

$$\bar{p}p \rightarrow \pi^0\gamma \quad (3.6)$$

$$\bar{p}p \rightarrow \gamma\gamma. \quad (3.7)$$

Two coalescing electron-positron pairs are generated if the two photons in reaction 3.7 convert in matter. A back-to-back electron-positron pair can be produced from reaction 3.6 as well and in two ways: (a) the pion decays into two photons, one of which converts in matter; (b) the pion undergoes Dalitz decay ($\pi^0 \rightarrow e^+e^-\gamma$). In both cases, the original photon has to convert and one photon from the pion decay has to be undetected. A similar reasoning applies to reaction 3.5.

The probability of $\pi^0\pi^0$ and $\pi^0\gamma$ to simulate $\gamma\gamma$ has been measured in E-760 with Monte Carlo techniques (Armstrong et al. 1997); the corresponding cross sections ($\sigma'_{\pi^0\pi^0}$ and $\sigma'_{\pi^0\gamma}$, respectively) dominate over the $\bar{p}p \rightarrow \gamma\gamma$ continuum cross section. The low probability of not detecting two photons from $\pi^0\pi^0$ is compensated by the high $\bar{p}p \rightarrow \pi^0\pi^0$ cross section, making these two background sources approximately equal; their sum is reported in Table 3.3 for some energy points.

The probability of a photon to convert before hodoscope H1, and thus to be able to fire the first-level trigger, has been measured in a sample of $\pi^0\pi^0$ events collected with a special total-energy neutral trigger with no hodoscope veto (Appendix A); it is $\eta < 1.7\times10^{-2}$, and it is consistent with estimates that employ the thickness of the material between the interaction region and H1. The probability of a pion to decay through the Dalitz process is $\delta=1.2\times10^{-2}$.

Due to their small opening angle, electron-positron pairs might be misidentified as single electron tracks. I estimate the rejection power of

$\sqrt{s}$ (GeV)	$\sigma'_{\pi^0\pi^0} + \sigma'_{\pi^0\gamma}$ (pb)
2.9	1×10^3
3.1	4×10^2
3.5	6×10^1
4.3	$<6\times10^1$

Tab. 3.3: Cross sections for $\pi^0\pi^0$ or $\pi^0\gamma$ final states simulating $\gamma\gamma$ (two or one photons not detected, respectively), based upon E-760 data and Monte Carlo calculation (Armstrong et al. 1997)

the Electron-Weight cut on a sample of "pairs", defined as charged tracks with a large energy deposit in the CCAL that, combined with another calorimeter cluster, give a π^0 invariant mass. The EW distribution for events in which both candidate electrons are actually pairs is shown in Figure 3.18a, for data taken at $\sqrt{s}$=3.0 GeV. From that distribution, I deduce that the probability ω of an event with two back-to-back pairs of passing the EW cut is $\omega < 4\times10^{-2}$ (Figure 3.18b).

Following the above discussion, the expected background cross section due to processes 3.5, 3.6 and 3.7 is:

$$\sigma_p < \omega \cdot \Big[\begin{array}{lll} (\delta+2\eta)^2 & \sigma'_{\pi^0\pi^0} & + \\ (\delta+2\eta)\eta & \sigma'_{\pi^0\gamma} & + \\ \eta^2 & \sigma_{\gamma\gamma} & \end{array} \Big]. \tag{3.8}$$

Numerically, σ_p is less than 6×10^{-2} pb at 2.9 GeV and less than 3×10^{-3} pb at 3.5 GeV.

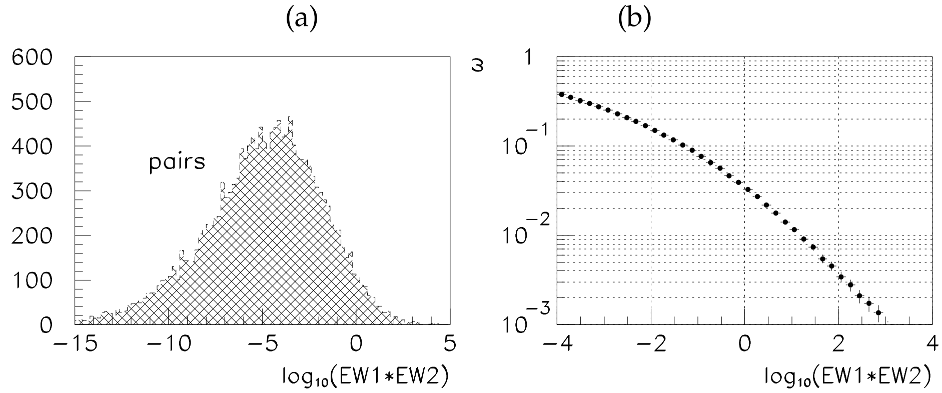

Fig. 3.18: (a) Distribution of the EW index for events with two back-to-back electron-positron pairs. (b) Rejection power ω as a function of the EW cut for the same sample of events.

(b) Two-body Hadronic Processes

A two-body hadronic final state can simulate an e^+e^- final state if the Čerenkov gives a signal, a hadronic shower is generated in the CCAL with the characteristics of an electromagnetic shower (energy and shape) and if the kinematics is similar. Because of its high cross section and due to the relatively small mass of the pions, the process:

$$\bar{p}p \rightarrow \pi^+\pi^- \tag{3.9}$$

is the most relevant. I estimate the probability ξ of a hadronic shower being generated in the CCAL with an energy compatible with the e^+e^- hypothesis with data from a dedicated trigger (Appendix B). This trigger requires two charged tracks as defined by the hodoscopes, without any requirements on the Čerenkov counter or the CCAL; the result is ξ=1×10^{-2}. From the same sample of data, the rejection inefficiency of the Čerenkov contribution to the Electron-Weight cut comes out to be κ <5×10^{-3} per track.

The differential cross section of process 3.9 is shown in Figure 3.19 for three different CM energies, as measured by Fields et al. (1972), Eide et al. (1973) and Buran et al. (1976), respectively. Also shown is the cross section integrated over the acceptance α_{acc} of the E-835 detector, as a function of energy; it varies between 2 μb at 2.9 GeV and 0.5 μb at 3.6 GeV. The expected background is

$$\begin{aligned} \sigma_h &= (\alpha_{acc}\sigma_{\pi^+\pi^-}) \cdot \kappa^2 \cdot \xi^2 \\ &< 0.5 \times 10^{-2} \text{ pb (at 2.9 GeV)} \\ &< 1.3 \times 10^{-3} \text{ pb (at 3.6 GeV).} \end{aligned} \tag{3.10}$$

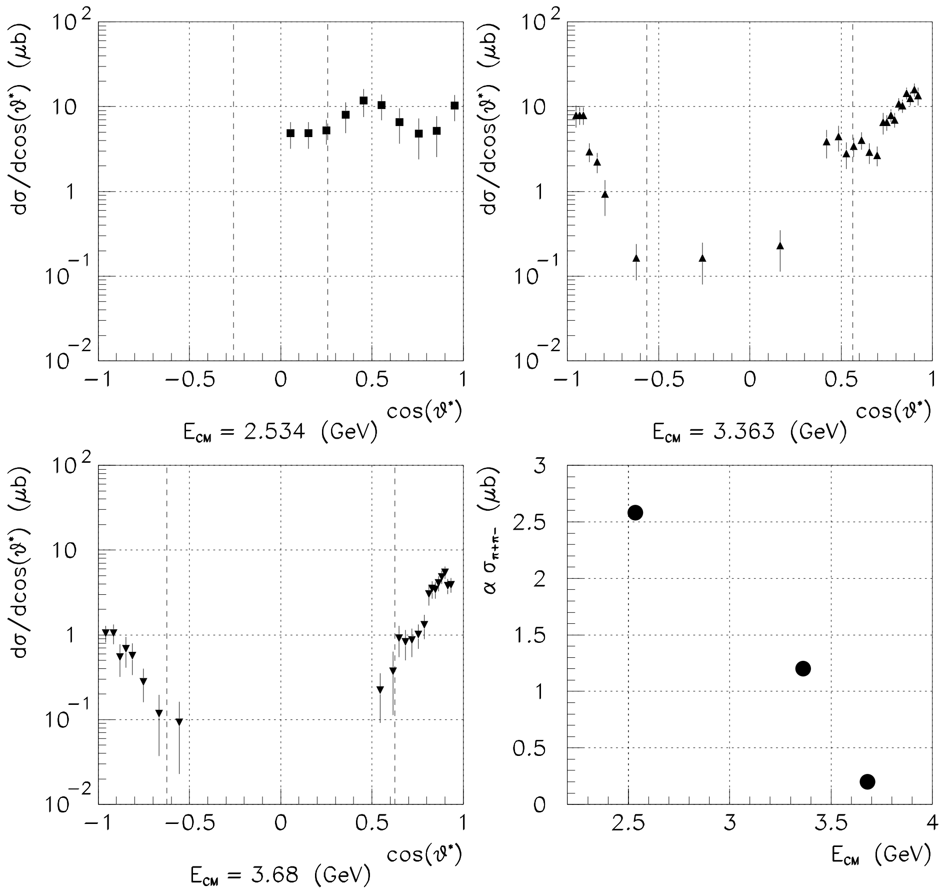

Fig. 3.19: Differential $\bar{p}p \rightarrow \pi^+\pi^-$ cross section taken from the literature (Fields et al. 1972; Eide et al. 1973; Buran et al. 1976). The bottom right plot shows the cross section integrated over the E-835 fiducial volume (vertical dashed lines in the other three plots), as a function of CM energy.

(c) Inclusive Production of J/ψ

Above a certain threshold, the process $\bar{p}p \to J/\psi + X$, followed by $J/\psi \to e^+e^-$, can fit the e^+e^- two-body kinematics, when X is not detected. For this reason, data taken in proximity of some charmonium resonances have been excluded, for this analysis, from the data sample (Section 3.1). The remaining J/ψ-inclusive continuum within the acceptance of this experiment is less than 5 pb and is mainly due to $\bar{p}\,p \to J/\psi\pi^0 \to (e^+e^-) + (\gamma\gamma)$ (Armstrong et al. 1992a). The probability, for an inclusive event, of satisfying two-body kinematics has been evaluated at the χ_{c1} and χ_{c2} resonances, in $J/\psi + \gamma$ decays in which the photon is not detected. It is defined as the fraction of events which satisfy the two-body kinematic fit probability cut. The result is 5×10^{-3} and is taken as an upper limit for all inclusive processes in the whole energy range. This yields a background contribution σ_i smaller than 2.5×10^{-2} pb.

Summing all the contributions $\sigma_B = \sigma_p + \sigma_h + \sigma_i$, one obtains σ_B=9×10^{-2} pb at 2.9 GeV and σ_B=4×10^{-2} pb at 3.5 GeV, corresponding to approximately one event at both energies. Since these background estimates are conservative, no subtraction from the number of candidate events is performed.

3.5 Measurement of the Form Factor

(a) Method

The number N of events collected with an integrated luminosity L and an overall efficiency ε is

$$N = \varepsilon\, L\, \sigma_{acc}, \qquad (3.11)$$

where the term σ_{acc} is the differential cross section integrated over the CM acceptance region (derived from Equation 1.25):

$$\begin{aligned}\sigma_{\text{acc}} &\equiv \int_{-|\cos\theta^*|_{\max}}^{+|\cos\theta^*|_{\max}} \left[\frac{d\sigma}{d(\cos\theta^*)}\right] d(\cos\theta^*) \qquad (3.12)\\ &= \frac{\pi\alpha^2}{8EP}\cdot\left[A\cdot|G_M|^2 + \frac{4m_p^2}{s}\cdot B\cdot|G_E|^2\right]. \qquad (3.13)\end{aligned}$$

At different values of s, the fiducial range $15° < \theta < 60°$ used in the event selection corresponds to different acceptances for θ^*, the scattering angle in the CM frame. At $\sqrt{s} < 3.661$ GeV, it is the upstream edge of the fiducial range ($\theta = 60°$) that determines $|\cos\theta^*|_{\max}$; whereas, for $\sqrt{s} > 3.661$ GeV, it is the downstream edge ($\theta = 15°$) that constrains the acceptance. The fact that the E-835 apparatus cannot distinguish between electrons and positrons is taken into account by integrating from $-|\cos\theta^*|_{\max}$ to $+|\cos\theta^*|_{\max}$; the (energy-dependent) acceptance coefficients A and B are:

$$A \equiv 2\cdot\int_0^{|\cos\theta^*|_{\max}} \left(1+\cos^2\theta^*\right) d(\cos\theta^*) \qquad (3.14)$$

$$B \equiv 2\cdot\int_0^{|\cos\theta^*|_{\max}} \left(1-\cos^2\theta^*\right) d(\cos\theta^*). \qquad (3.15)$$

For small $|\cos\theta^*|_{\max}$, A is approximately equal to B and the relative importance of the 'electric' and 'magnetic' contributions is weighed by $4m_p^2/s$ only. As $|\cos\theta^*|_{\max}$ approaches one, the ratio A/B tends to 2, and the 'electric' contribution is further suppressed.

The measurement of the angular distribution of the form factor events would decouple the 'electric' and 'magnetic' contributions to the differential cross section. Unfortunately, high statistics and wide angular coverage are necessary. Figure 3.20 gives an idea of how close three of the possible angular distributions are. A flat distribution (solid line), a $1+\cos^2\theta^*$ distribution (dashed line, implying negligible 'electric' contribution) and a

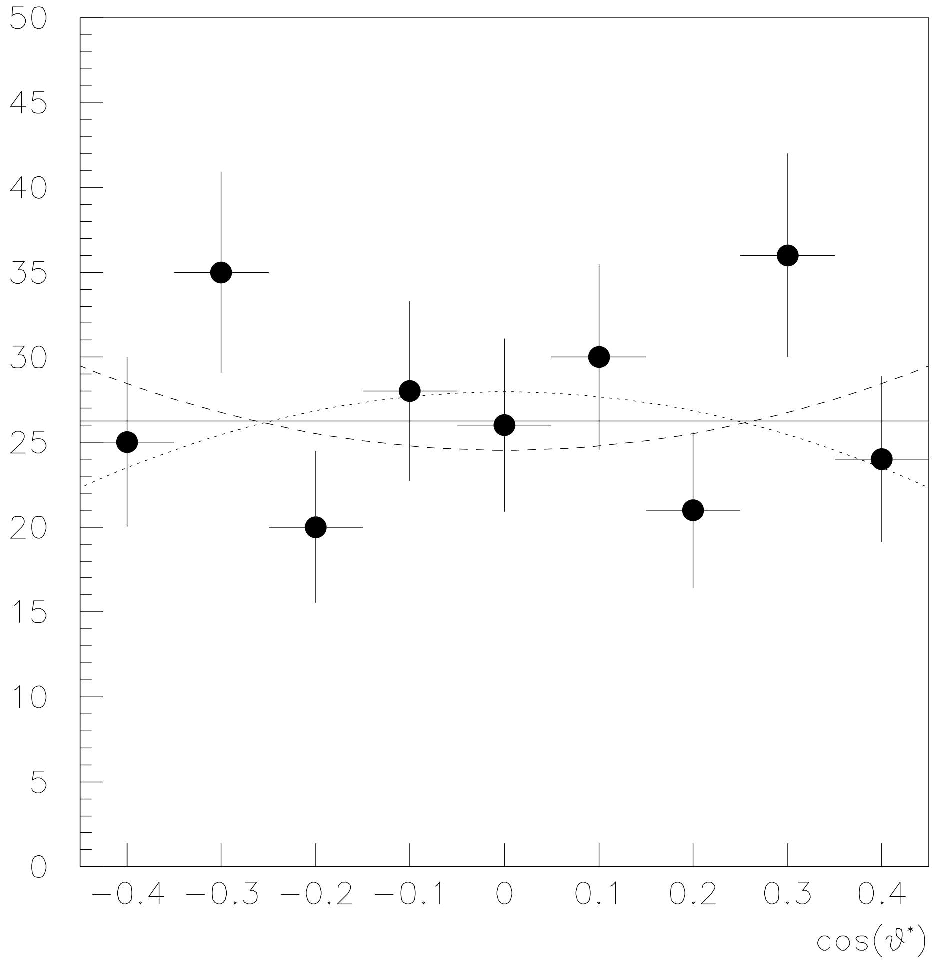

Fig. 3.20: Angular distribution of all form factor events in the CM acceptance region common to all energy points (two entries per event). Different functional forms are equally compatible.

$1-\cos^2\theta^*$ distribution (dotted line, negligible 'magnetic' contribution) are fitted to the data in the CM acceptance region common to all data points ($|\cos\theta^*| < 0.45$, from Table 3.4). The small number of events makes it impossible to discriminate between the various functional forms, which are equally compatible with the data; $\chi^2 \simeq 0.8$ for all three fits.

Since the low statistics and the limited $\cos\theta^*$ range do not allow to make a separate measurement of $|G_E|$ and $|G_M|$, I make two alternative hypotheses: (a) $|G_E| = |G_M|$, as is the case at the threshold of the timelike region ($s = 4m_p^2$), by definition of form factors (Equation 1.11); (b) the 'electric' contribution is assumed to be negligible. Under hypothesis (b), the measurement of the magnetic form factor of the proton is achieved through the relation:

$$|G_M| = \frac{1}{\alpha} \cdot \sqrt{\frac{8}{\pi}} \cdot \left[\frac{E\,P\,N}{\varepsilon\,A\,L}\right]^{\frac{1}{2}} . \tag{3.16}$$

Under hypothesis (a), A is replaced by $A + (4m_p^2/s) \cdot B$.

(b) Results

The results obtained are shown in Table 3.4. For each energy region, the integrated luminosity L, the number of selected events N, the cross section $\sigma_{acc} \equiv N/(L \cdot \varepsilon)$ and the geometrical acceptance in the CM frame are shown. Both statistical and systematic errors on σ_{acc} and $|G_M|$ are reported. The magnitude of the observed cross sections σ_{acc} relative to the total $\bar{p}p$ cross section (≈ 70 mb) should be emphasized.

Some data have been taken at $s = 18.4$ GeV^2, but no e^+e^- events have been observed. In Table 3.4, an upper limit of 2.44 events is given, corresponding to a 90% confidence level (Feldman and Cousins 1998; Caso et al. 1998).

The values of $|G_M|$ determined in the two hypotheses differ by 16% at

s	L	N	σ_{acc}	$\lvert\cos\theta^*\rvert_{max}$	$10^2 \times \lvert G_M\rvert$	
(GeV^2)	(pb^{-1})		(pb)		(a)	(b)
8.84 ± 0.16	17.69	93	$7.78^{+0.81+0.96}_{-0.81+0.67}$	0.451	$3.55^{+0.18+0.22}_{-0.19-0.17}$	$4.13^{+0.21+0.25}_{-0.22-0.18}$
10.78 ± 0.28	1.78	3	$2.49^{+1.9+0.3}_{-1.7-0.2}$	0.544	$2.11^{+0.70+0.14}_{-0.83-0.11}$	$2.38^{+0.78+0.15}_{-0.94-0.11}$
12.43 ± 0.02	47.84	33	$1.02^{+0.18+0.13}_{-0.18-0.08}$	0.601	$1.42^{+0.12+0.08}_{-0.13-0.06}$	$1.57^{+0.13+0.09}_{-0.14-0.07}$
13.11 ± 0.18	33.99	14	$0.61^{+0.19+0.07}_{-0.17-0.05}$	0.621	$1.11^{+0.16+0.07}_{-0.16-0.05}$	$1.22^{+0.18+0.08}_{-0.17-0.06}$
14.36 ± 0.50	1.86	1	$0.80^{+1.4+0.10}_{-0.8-0.07}$	0.604	$1.37^{+0.90+0.13}_{-0.54-0.11}$	$1.50^{+0.99+0.14}_{-0.59-0.12}$
18.40 ± 0.01	0.76	0	< 4.78	0.508	< 4.36	< 4.69

Tab. 3.4: Summary of the results of the form factor analysis.

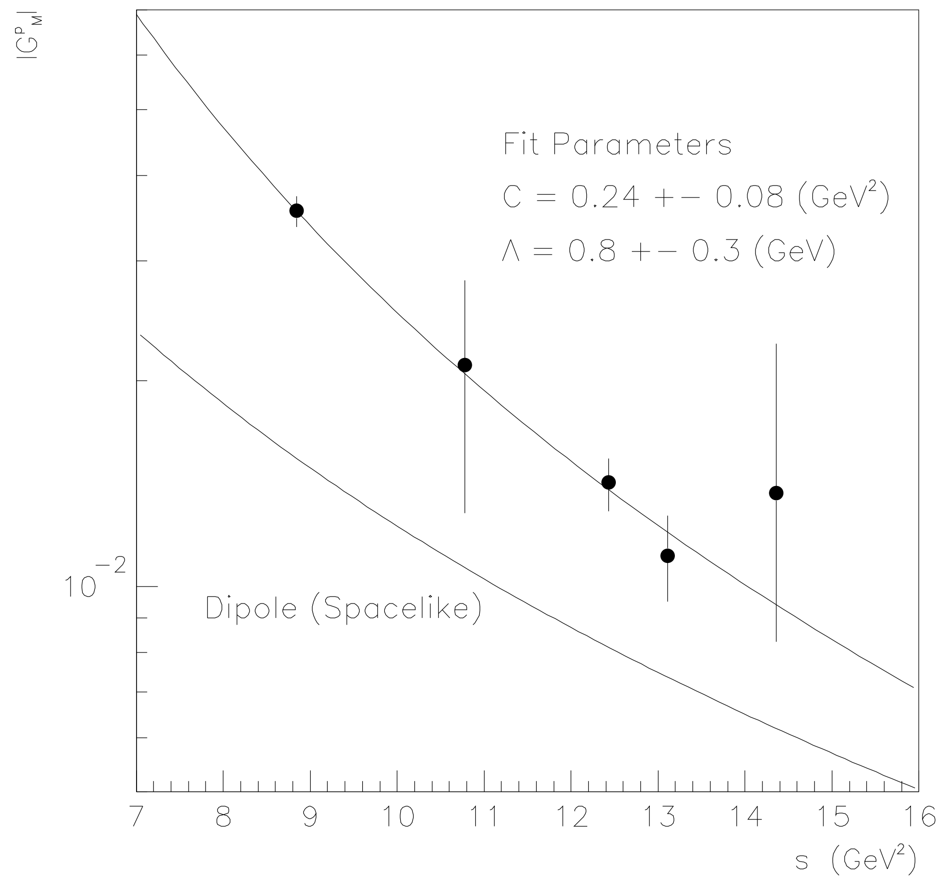

Fig. 3.21: A fit to the data in the asymptotic form of Equation 1.30. Also shown is the dipole behavior of the form factor in the spacelike region.

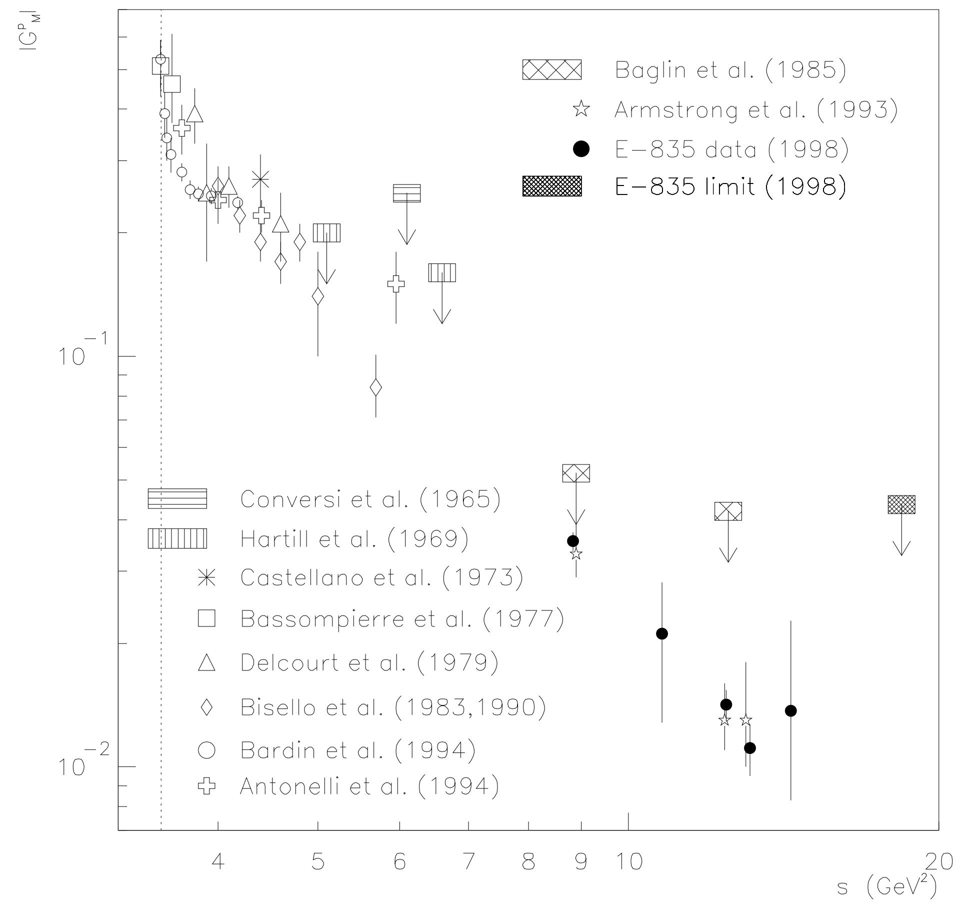

Fig. 3.22: The measurements presented in this dissertation (E-835 data and limit) are compared with all previous measurements. The values correspond to the $|G_E| = |G_M|$ hypothesis. The cross-hatched rectangles represent upper limits at the 90% confidence level.

$s = 8.8\ \text{GeV}^2$ and by 9% at $s = 14.4\ \text{GeV}^2$. The values of $|G_M|$ obtained under assumption (a) are plotted in Figure 3.21 and in Figure 3.22, where they are compared with the E-760 results and with earlier measurements.

Figure 3.21 shows a fit to the data in the asymptotic form described by Equation 1.30, where C and Λ are treated as free parameters. The fit can reproduce the data very well ($\chi^2 = 0.3$), even though the asymptotic regime has not been reached. In fact, there is still an appreciable difference between the timelike and the spacelike form factors. In Figure 3.21, the spacelike form factor at $s = Q^2$ is represented by the dipole functional form (Equation 1.16); the timelike form factor is 1.5 to 3 times larger, depending upon the energy.

(c) Remarks on the Uncertainties

Both statistical and systematic uncertainties on $|G_M|$ are reported in Table 3.4. They come from the errors on the directly-measured quantities, namely the number of events N, the luminosity L, the selection efficiency ε and the CM energy $\sqrt{s}$ (Equation 3.16).

In some cases, the relative errors on the directly-measured quantities are not small compared to 1, especially when coming from the number of events. For this reason, when propagating the error on x (one of the directly-measured quantities) to the derived variable $|G_M| = f(x) \propto \sqrt{x}$, I used the exact formula $\delta\,|G_M| = f(x + \delta x) - f(x)$ instead of the approximation $\delta\,|G_M| = (d\,|G_M|\,/dx) \cdot \delta x$.

Statistical Error. The statistical uncertainties dominate over the systematic ones, except for the data point where there are 93 events. Obviously, they are mainly due to the error on N. There is also a small contribution from the measurement of the efficiency (0.3%) and of the luminosity (0.1%). For the purpose of calculating the statistical error on the form factor, the contributions from the various sources are added in quadrature.

Systematic Error. The main systematic uncertainty comes from the efficiency (3–4%). The error on the value of ε used for all six data points takes into account variations due to CM energy, run to run inhomogeneities and background subtraction procedure, described in Section 3.2. The systematic uncertainty on the luminosity L (3%) yields a relative error of 1.5% on the form factor. The error on E, P, A and B, due to the grouping of several runs at different energies, is generally negligible, except for the point at s = 14.4 GeV^2, where the form factor is small and the energy interval is relatively wide; there, the corresponding relative error on $|G_M|$ is 4%. Systematic uncertainties are added linearly when calculating the total systematic error on the form factor.

4. CONCLUSIONS

In this dissertation, I presented new high-precision measurements of the magnetic form factor of the proton for large timelike momentum transfers at $q^2 = s$ between 8.8 GeV^2 and 14.4 GeV^2. An upper limit has also been extracted at $s = 18.4$ GeV^2, even though, due to the small amount of luminosity accumulated in this energy region, the limit is rather lax.

The results are in excellent agreement with those of E-760, which is the only other experiment which has obtained non-zero results in this energy interval. The values of $|G_M|$ I found also confirm the semi-quantitative predictions of QCD.

The experimental technique has proven very successful. It employs a non-magnetic spectrometer to identify e^+e^- final states generated by an antiproton beam intersecting an internal hydrogen gas jet target. Still, in order to investigate timelike form factors at higher energies and reach the asymptotic regime (where the theory is most easily calculable), it will be necessary to develop new techniques or better performing detectors. In fact, the rapidly decreasing cross section and the huge hadronic background demand higher and higher luminosities and more powerful electron/positron tagging.

This is a field of active research also from the theoretical point of view. One of the goals is being able to calculate the form factors of baryons where experimental information exists. In particular, the full understanding of the proton structure (one of the building blocks of matter as we know it) is among the extremely interesting challenges facing Quantum Chromodynamics.

APPENDIX

A. PHOTON CONVERSIONS

The probability η that a photon generated in the interaction region converts in matter before reaching hodoscope H1 affects the background level for the form factor events (Section 3.4).

I measure this probability using data from a special total-energy trigger without hodoscope vetoes. This trigger simply requires that the energy deposited in the CCAL be at least 80% of the total energy in the lab frame; it is referred to as ETOT 80% no-veto.

From this sample, a clean $\pi^0\pi^0 \to 4\gamma$ subset is selected, by requiring exactly four clusters in the CCAL with their centers between ring 2 and ring 18 included. For the 5439 events that survive, the four clusters are paired according to which combination gives the best $\pi^0\pi^0$ kinematics, quantified by the minimum value of the variable:

$$(w_\theta \cdot \Delta\theta)^2 + (w_\phi \cdot \Delta\phi)^2 \, . \tag{A.1}$$

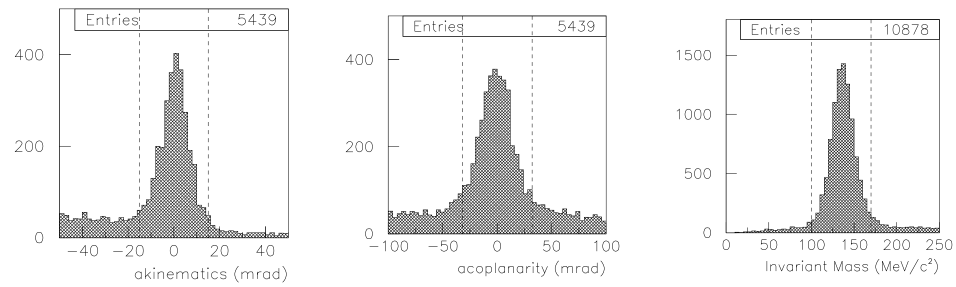

Fig. A.1: Distribution of akinematics, acoplanarity and candidate pion mass for four-cluster events from the total-energy study trigger.

The akinematics $\Delta\theta$ is defined as the difference between two quantities: (a) the value of the forward pion's polar angle predicted from the backward pion according to two-body kinematics and (b) the measured value of the forward pion's polar angle. $\Delta\phi$ is the acoplanarity, ie $|\phi_1 - \phi_2| - \pi$, which measures the azimuthal deviation from two-body kinematics. The weight w_θ is twice as large as the weight w_ϕ; it is determined a posteriori from the widths of the akinematics and acoplanarity distributions (Figure A.1). After the four clusters have been paired, three cuts are applied:

- invariant mass of the both candidate photon pairs within a ± 35 MeV window centered around the π^0 rest energy (=135 MeV);
- absolute value of the akinematics smaller than 15 mrad;
- absolute value of the acoplanarity smaller than 32 mrad.

The corresponding distributions before these three cuts are shown in Figure A.1. The final clean sample contains 2585 events, or 10340 tracks.

If one of the four calorimeter clusters is associated with a coincidence between hodoscopes H1 and H2$'$ (or H2), then it is identified as a photon conversion or as a Dalitz decay of the pion.

The opening angle of the photons coming from the same pion is small compared to the hodoscope granularity. Often ($\simeq 75\%$ of the times), if one of the two photons is associable with a hodoscope line, the other one is too. Neglecting this fact would make most of the conversions count as two, and this would end up in an overestimation of the conversion probability η. To avoid this, I make the assumptions that the conversion probabilities of the two photons are independent and that η^2 or $\eta \cdot \delta$ ($\delta = 0.6\%$ is the Dalitz probability per cluster) are small compared to η. Each time both clusters are associated with a hodoscope coincidence, the event is registered as a single occurence of a conversion or a Dalitz decay.

The results are shown in Figure A.2 as a function of the polar and azimuthal angles. Since Dalitz decays cannot be distinguished from conversions, the fraction of CCAL clusters with an associated charged track is the sum of two independent contributions. The Dalitz contribution per cluster is 0.6%. What is left (less than 1.7%), is attributed to photon conversions[a]; it is consistent with estimates that employ the thickness of the material between the interaction region and hodoscope H1. This value η = 1.7% is used in Section 3.4 to evaluate the form factor background due to neutral pions and photons.

[a] I am neglecting the detection inefficiency of the hodoscopes, H1 in particular.

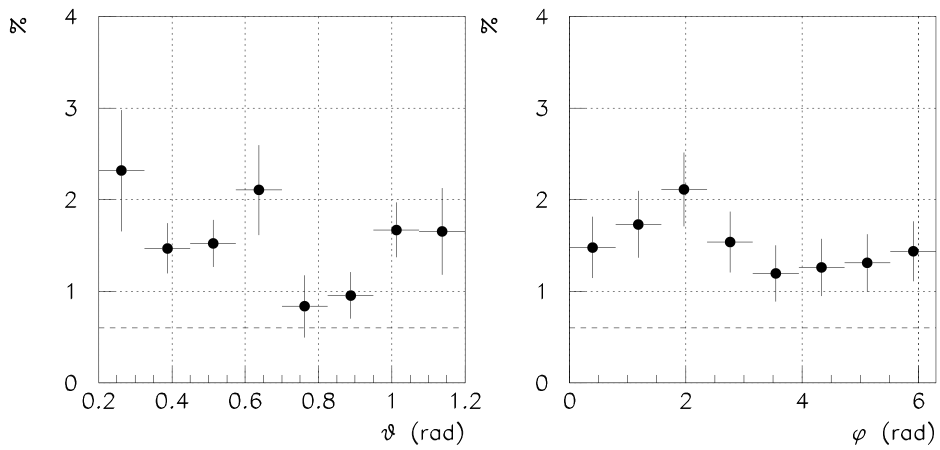

Fig. A.2: Probability of photon conversions or Dalitz decays before H1, as a function of the polar and azimuthal angles. The horizontal dashed line represents the contribution attributed to Dalitz decay.

B. PION REJECTION

The reaction $\bar{p}p \to \pi^+\pi^-$ contributes to the background for the form-factor selection (Section 3.4). I selected a sample of $\pi^+\pi^-$ events to measure the pion rejection inefficiency of the Čerenkov counter and of the CCAL. Both detectors contribute to the rejection of the first-level trigger and of the Electron-Weight algorithm. The main cause of inefficiency in the Čerenkov counter is the emission of δ-rays by a charged track. In the CCAL, the discrimination between hadrons and electrons or positrons is based on the magnitude and on the shape of the energy deposition.

Since the E-835 detector has not been designed to select hadrons (and much less to identify them), the $\pi^+\pi^-$ sample cannot be as clean as the e^+e^- samples are. Still, there are two trigger types which can be suitable for selecting the charged pion sample:

- minimum-bias trigger, requiring just two hits in the calorimeter above 100 MeV; these events have been collected at low rate throughout the data-taking run, with a prescaling factor of 10^5;
- two-body hadronic trigger, taken only once ($\sqrt{s} = 2.951$ GeV, runs 2225–2230, L = 605 nb^{-1}, prescaling factor of 1.2×10^2), and used to measure the efficiency of the proton-antiproton trigger. This logic is defined as $(2h) \cdot (H2 = 2) \cdot (COPL) \cdot (\overline{FCH})$; the symbols are explained in Section 3.1.(b).

There is also a limited set of minimum-bias events taken with a lower

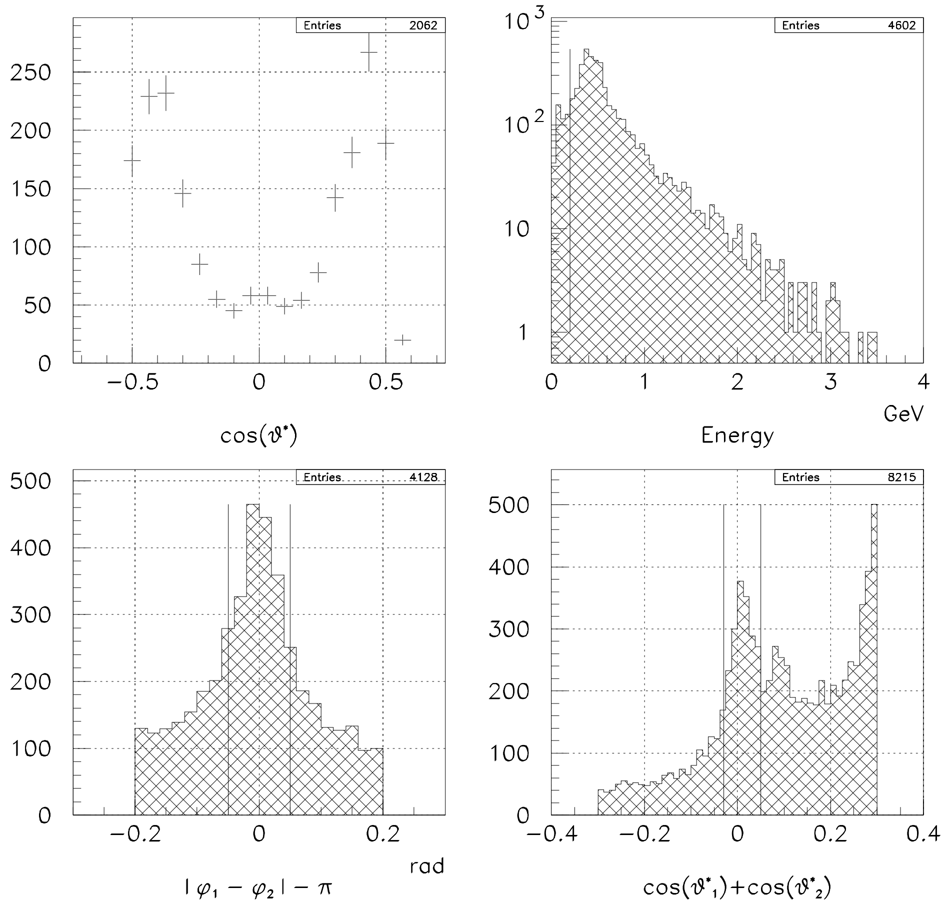

Fig. B.1: The $\pi^+\pi^-$ sample. The angular distribution of the tracks in the CM frame is shown on the top left (two entries per event). On the top right is the energy distribution before the energy cut (represented by the vertical line) and after all other cuts. The analogous plots for the acoplanarity and the $[\cos(\theta_1^*) + \cos(\theta_2^*)]$ distributions are shown at the bottom.

prescaling factor. For this study, I choose the $\bar{p}p$ study trigger, which is the most statistically significant.

Besides a strict two-cluster cut on the CCAL multiplicity, the off-line selection of $\bar{p}p \to \pi^+\pi^-$ is essentially based upon azimuthal and polar kinematics. The cuts are applied on cluster energy, acoplanarity $\equiv |\phi_1 - \phi_2| - \pi$ and on the sum $\cos(\theta_1^*) + \cos(\theta_2^*)$ of the cosines in the CM frame; the corresponding distributions are shown in Figure B.1, together with the cuts.

For each of the 2062 selected tracks, the probability of having a signal in the Čerenkov counter above 0.5 phe, which is the threshold used in the first-level trigger, is measured as a function of the polar and azimuthal angles (Figure B.2). The high rejection inefficiency in the upstream region is likely due to the phototube recesses; however, in the form factor analysis, that region is excluded from the fiducial volume. In the region between 15° and 60°, the average rejection inefficiency is 82/1646 = (5.0±0.5)%.

The fraction of tracks releasing in the CCAL an energy deposit com-

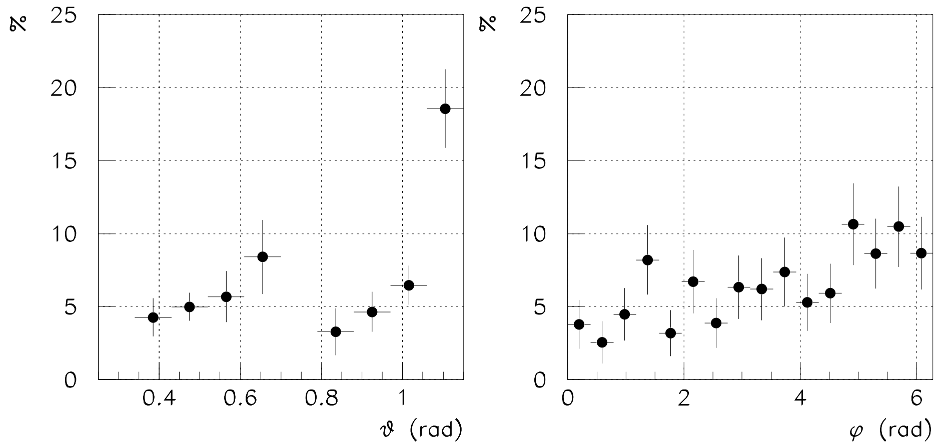

Fig. B.2: Pion rejection inefficiency of the Čerenkov counter as a function of the polar and azimuthal angles.

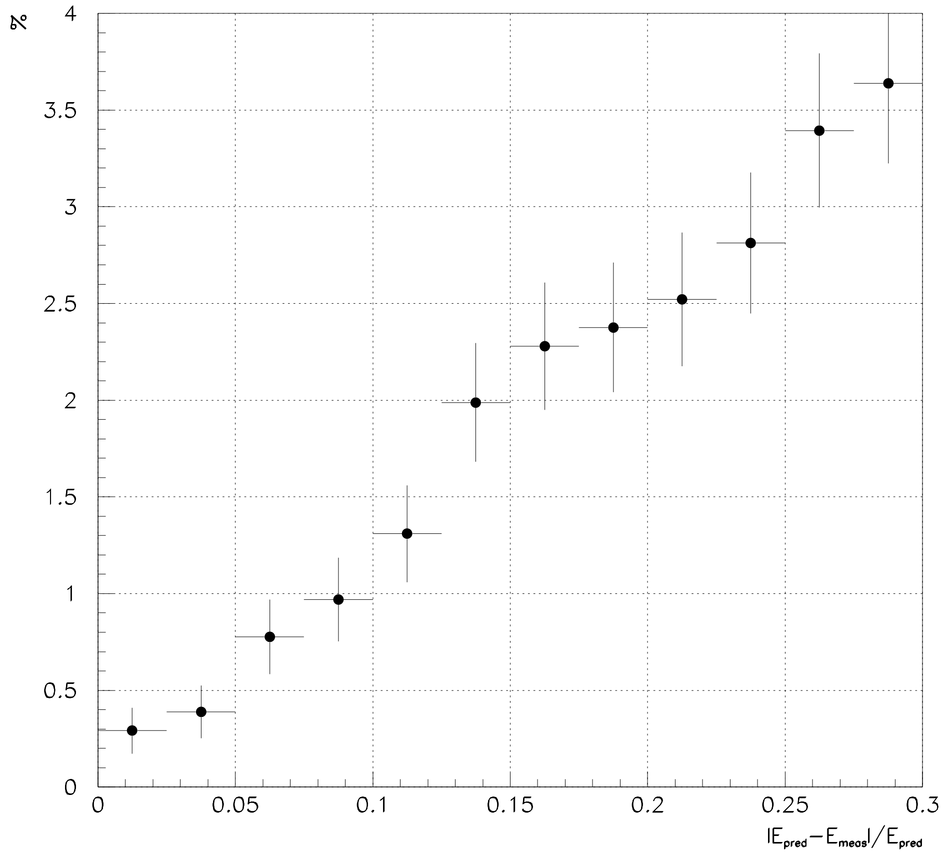

Fig. B.3: Fraction of pion showers having a measured energy compatible with an electron shower in the same polar region, as a function of the relative deviation from the predicted energy.

patible with the e^+e^- kinematics is also recorded. From Figure B.3, the probability of a pion shower of having an energy within 10% of the energy of an electron impinging in the same polar region is (1.0±0.2) %. This can be taken as the pion rejection inefficiency of the CCAL when the shape of the cluster is not used (for example, in the first-level trigger).

The sample is too small to evaluate the Čerenkov rejection at trigger level and at the EW level separately. For this reason, I also calculate an overall Čerenkov inefficiency, which includes the EW cut. An upper limit can be extracted by determining how often a pion track has $\mathrm{EW} > 0$. In fact, the fraction of $\pi^+\pi^-$ events passing the EW cut used in the analysis ($\log_{10}(\mathrm{EW1} \cdot \mathrm{EW2}) > 0$) will be a subset of those having both tracks with $\mathrm{EW} > 0$. A clean sample of electron/positron tracks from the J/ψ is selected with kinematic cuts. The distribution of Čerenkov signal for the

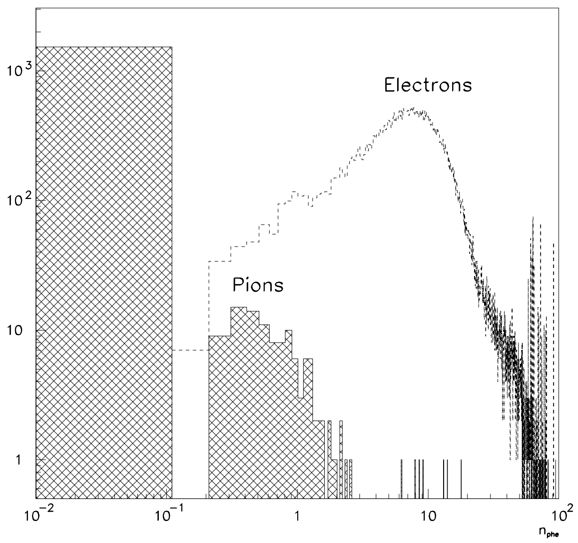

Fig. B.4: Distribution of Čerenkov signals for clean electron tracks and for events in the $\pi^+\pi^-$ sample.

electron tracks with EW > 0 is plotted in Figure B.4. After normalization, this distribution is interpreted as the derivative of the probability Π of passing the EW > 0 cut as a function of the number of photoelectrons n_{phe}. This is a conservative assumption, because it neglects the CCAL contribution to the EW. The probability Π is constrained to be zero at $n_{\mathrm{phe}} = 0$ and approaches one as n_{phe} increases. The n_{phe} distribution for all pion tracks is also shown in Figure B.4. The probability κ of a pion track of passing the EW cut due to the Čerenkov signal is taken to be this distribution multiplied by Π and summed over n_{phe}. The result is $\kappa = (5\pm1)\times10^{-3}$; I use this number in the background estimates of Section 3.4.

REFERENCES

Allspach, D. et al. (1998). The variable density gas jet internal target for Experiment 835 at Fermilab. *Nucl. Instrum. Meth. Phys. Res. A 410*, 195–205.

Ambrogiani, M. et al. (1997). Construction and Performance of a Cylindrical Scintillating Fiber Detector for Experiment 835 at FNAL. *IEEE Trans. Nucl. Sci. 44*, 460–463.

Ambrogiani, M. et al. (1998). The E835 scintillating fiber tracking detector. *Nucl. Phys. B (Proc. Suppl.) 61B*, 384–389.

Andivahis, L. et al. (1994). Measurements of the electric and magnetic form factors of the proton from $Q^2 = 1.75$ to 8.83 $(\mathrm{GeV}/c)^2$. *Phys. Rev. D 50*(9), 5491–5517.

Antonelli, A. et al. (1994). Measurement of the electromagnetic form factor of the proton in the time-like region. *Phys. Lett. B 334*, 431–434.

Armstrong, T. A. et al. (1992a). Observation of the $^1P_1$ State of Charmonium. *Phys. Rev. Lett. 69*(16), 2337–2340.

Armstrong, T. A. et al. (1992b, September). Proposal to Continue the Study of Charmonium Spectroscopy in Proton-Antiproton Annihilations. Proposal P-835, Fermilab. Presented by the E760 Collaboration.

Armstrong, T. A. et al. (1993). Proton Electromagnetic Form Factors in the Timelike Region from 8.9 to 13.0 GeV^2. *Phys. Rev. Lett. 70*(9), 1212–

1215.

Armstrong, T. A. et al. (1996). Precision measurements of antiproton-proton forward elastic scattering parameters in the 3.7 to 6.2 GeV/c region. *Phys. Lett. B 385*, 479–486.

Armstrong, T. A. et al. (1997). Two-body neutral final states produced in antiproton-proton annihilations at $2.911 \leq \sqrt{s} \leq 3.686$ GeV. *Phys. Rev. D 56*(5), 2509–2531.

Atac, M. (1998). Visible Light Photon Counters (VLPCs) for High Rate Tracking Medical Imaging and Particle Astrophysics. See Bross, Ruchti, and Wayne (1998), pp. 315–331.

Baglin, C. et al. (1985). Upper Limits of the Proton Magnetic Form Factor in the Time-like Region from $\bar{p}p \to e^+e^-$ at the CERN-ISR. *Phys. Lett. 163B*(5,6), 400–403.

Bagnasco, S. et al. (1997, June). FCAL II: Design and Construction. Fermilab E-835 Internal Note, unpublished.

Bagnasco, S. et al. (1998a). A straw chambers' tracker for the high rate experiment 835 at the Fermilab accumulator. *Nucl. Instrum. Meth. Phys. Res. A 409*, 75–78.

Bagnasco, S. et al. (1998b). The Threshold Gas Cherenkov Counter of Charmonium Experiment 835 at Fermilab. *Nucl. Instrum. Meth. Phys. Res.*. Submitted.

Baldini, W. and F. Marchetto (1997, April). Charged trigger efficiency for inclusive J/ψ. Fermilab E-835 Internal Note, unpublished.

Bardin, G. et al. (1991a). Measurement of the proton electromagnetic form factor near threshold in the time-like region. *Phys. Lett. B 255*(1), 149–154.

Bardin, G. et al. (1991b). Precise determination of the electromagnetic form factor of the proton in the time-like region up to $s = 4.2\ \text{GeV}^2$. *Phys. Lett. B 257*(3,4), 514–518.

Bardin, G. et al. (1994). Determination of the electric and magnetic form factors of the proton in the time-like region. *Nucl. Phys. B411*, 3–32.

Bartoszek, L. et al. (1991). The E760 lead-glass central calorimeter: design and initial test results. *Nucl. Instrum. Meth. Phys. Res. A 301*, 47–60.

Bassompierre, G. et al. (1976). Measurement of the Branching Ratio $\Gamma(\bar{p}p \to e^+e^-)/\Gamma(\bar{p}p \to \text{total})$ in Antiproton-Proton annihilation at Rest. *Phys. Lett. 64B*(4), 475–478.

Bassompierre, G. et al. (1977). First Determination of the Proton Electromagnetic Form Factors at the Threshold of the Time-like Region. *Phys. Lett. 68B*(5), 477–479.

Biino, C. et al. (1992). A large acceptance threshold cherenkov counter for Experiment 760 at Fermilab. *Nucl. Instrum. Meth. Phys. Res. A 317*, 135–142.

Bisello, D. et al. (1983). A Measurement of $e^+e^- \to \bar{p}p$ for $(1975 \leq \sqrt{s} \leq 2250)$ MeV. *Nucl. Phys. B224*, 379–395.

Bisello, D. et al. (1990). Barion pairs production in e^+e^- annihilation at $\sqrt{s} = 2.4$ GeV. *Z. Phys. C 48*, 23–28.

Braunschweig, W. et al. (1975). Two-body Hadronic Decays of the 3.1 GeV Resonance. *Phys. Lett. 57B*(3), 297–300.

Bross, A. D., R. C. Ruchti, and M. R. Wayne (Eds.) (1998). *SciFi97: Workshop on Scintillating Fiber Detectors*, AIP Conference Proceedings 450, Woodbury, New York. American Institute of Physics.

Buran, T. et al. (1976). Antiproton-proton annihilation into $\pi^+\pi^-$ and K^+K^- at 6.2 GeV/c. *Nucl. Phys. B116*, 51–64.

Buzzo, A. et al. (1997). A Silicon Pad Detector for E-835 experiment at Fermilab. *Nucl. Instrum. Meth. Phys. Res. A 391*, 443–451.

Cabibbo, N. and R. Gatto (1961). Electron-Positron Colliding Beam Experiments. *Phys. Rev. 124*(5), 1577.

Caso, C. et al. (1998). Review of Particle Physics. *Euro. Phys. J. C 3*(1–4), 1–794.

Castellano, M. et al. (1973). The Reaction $e^+e^- \to p\bar{p}$ at a Total Energy of 2.1 GeV. *Nuovo Cimento 14 A*(1), 1–20.

Cester, R. and P. Rapidis (1994). Charmonium Formation in $\bar{p}p$ Annihilations. *Annu. Rev. Nucl. Part. Sci. 44*, 329–371.

Church, M. D. and J. P. Marriner (1993). The Antiproton Sources: Design and Operation. *Annu. Rev. Nucl. Part. Sci. 43*, 253–295.

Conversi, M. et al. (1965). The Leptonic Annihilation Modes of the Proton-Antiproton System at 6.8 $(\mathrm{GeV}/c)^2$ Timelike Four-Momentum Transfer. *Nuovo Cimento XL A*(2), 690–701.

Dalpiaz, P. (1979). Charmonium and Other Onia at Minimum Energy. In H. Poth (Ed.), *Karlsruhe 1979: Physics with Cooled Low Energetic Antiprotons (First LEAR Workshop)*, pp. 111–124.

Delcourt, B. et al. (1979). Study of the Reaction $e^+e^- \to p\bar{p}$ in the Total Energy Range 1925–2180 MeV. *Phys. Lett. 86B*(3,4), 395–398.

Eide, A. et al. (1973). Elastic scattering and two-body annihilations at 5 GeV/c. *Nucl. Phys. B60*, 173–220.

Ernst, F. J., R. G. Sachs, and K. C. Wali (1960). Electromagnetic Form

Factors of the Nucleon. *Phys. Rev. 119*(3), 1105–1114.

Feldman, G. J. and R. D. Cousins (1998). Unified approach to the classical statistical analysis of small signals. *Phys. Rev. D 57*(7), 3873–3889.

Fields, T. et al. (1972). Comparison of new data on $\bar{p}p \rightarrow \pi^-\pi^+$ and other two meson states at 2.3 GeV/c. *Phys. Lett. 40B*(4), 503–506.

Foldy, L. L. (1952). The Electromagnetic properties of Dirac Particles. *Phys. Rev. 87*(5), 688–693.

Garzoglio, G. (1998). Private communication.

Gousset, T. and B. Pire (1995). Timelike form factors at high energy. *Phys. Rev. D 51*(1), 15–24.

Hand, L. N., D. G. Miller, and R. Wilson (1963). Electric and Magnetic Form Factors of the Nucleon. *Rev. Mod. Phys. 35*(2), 335–349.

Hartill, D. L. et al. (1969). Antiproton-Proton Annihilation into Electron-Positron Pairs and Gamma-Ray Pairs. *Phys. Rev. 184*(5), 1415–1423.

Hasan, M. A. et al. (1990). The Fermilab E760 forward electromagnetic calorimeter. *Nucl. Instrum. Meth. Phys. Res. A 295*, 73–80.

Hofstadter, R. (1963). *Electron Scattering and Nuclear and Nucleon Structure*. New York: W. A. Benjamin, Inc.

Jacob, M. and G. C. Wick (1959). On the General Theory of Collisions for Particles with Spin. *Ann. Phys. 7*, 404–428.

Kroll, P., T. Pilsner, M. Schürmann, and W. Schweiger (1993). On exclusive reactions in the time-like region. *Phys. Lett. B 316*, 546–554.

Lepage, G. P. and S. J. Brodsky (1980). Exclusive processes in perturbative quantum chromodynamics. *Phys. Rev. D 22*(9), 2157–2198.

McAllister, R. W. and R. Hofstadter (1956). Elastic Scattering of 188-Mev Electrons from the Proton and the Alpha Particle. *Phys. Rev. 102*(3), 851–856.

Patrignani, C. (1997?). J/ψ inclusive selection using the Electron Weight. Fermilab E-835 Internal Note, unpublished.

Patrignani, C. (1998). Private communication.

Pedlar, T. K. (1998, September). Elements of Precision: Luminosity Measurement in E835. Fermilab E-835 Internal Note, unpublished.

Petroff, M. D. and M. Atac (1989). High energy particle tracking using scintillating fibers and solid state photomultipliers. *IEEE Trans. Nucl. Sci. 36*(1), 163–164.

Rosenbluth, M. N. (1950). High Energy Elastic Scattering of Electrons on Protons. *Phys. Rev. 79*(4), 615–619.

Ruchti, R. C. (1996). The Use of Scintillating Fibers for Charged-Particle Tracking. *Annu. Rev. Nucl. Part. Sci. 46*, 281–319.

Salzman, G. (1955). Neutron-Electron Interaction. *Phys. Rev. 99*(3), 973–979.

Sill, A. F. et al. (1993). Measurements of elastic electron-proton scattering at large momentum transfer. *Phys. Rev. D 48*(1), 29–55.

Sterman, G. and P. Stoler (1997). Hadronic Form Factors and Perturbative QCD. *Annu. Rev. Nucl. Part. Sci. 47*, 193–233.

Trokenheim, S., M. Sarmiento, K. K. Seth, and L. Bartoszek (1994). A $p\bar{p}$ luminosity monitor for Fermilab experiment E760. *Nucl. Instrum. Meth. Phys. Res. A 355*, 308–319.

Walker, R. C. et al. (1994). Measurements of the proton elastic form factors for $1 \leq Q^2 \leq 3$ $(GeV/c)^2$ at SLAC. *Phys. Rev. D 49*(11), 5671–5689.

Yennie, D. R., M. M. Lévi, and D. G. Ravenhall (1957). Electromagnetic Structure of Nucleons. *Rev. Mod. Phys. 29*(1), 144–157.

Zichichi, A. et al. (1962). Proton-Antiproton Annihilation into Electrons, Muons and Vector Bosons. *Nuovo Cimento XXIV*(1), 170–180.